# Towards Directed Self-Assembly of Quantum Dot Mesocrystals of Ge/Si Using Focused Ion Beam Patterning

---

A Dissertation

Presented to

the faculty of the School of Engineering and Applied Science

University of Virginia

---

in partial fulfillment

of the requirements for the degree

Doctor of Philosophy

by

Christopher J Duska

August

2016

APPROVAL SHEET

The dissertation
is submitted in partial fulfillment of the requirements
for the degree of
Doctor of Philosophy

AUTHOR

The dissertation has been read and approved by the examining committee:

Jerrold Floro
Advisor

Petra Reinke, Chair

Stu Wolf

Patrick Hopkins

Stephen McDonnell

Accepted for the School of Engineering and Applied Science:

Craig H. Benson, Dean, School of Engineering and Applied Science

August
2016

# Table of Contents

1

## List of Figures

## List of Abbreviations and Acronyms

| | |
|---|---|
| 2D-FFT | Two-dimensional fast Fourier transform |
| 3D | Three dimensional |
| AFM | Atomic force microscopy |
| a.m.u. | Atomic mass unit |
| ATG | Asaro-Tiller-Grinfeld |
| BF | Bright field |
| BOE | Buffered oxide etch |
| CBED | Convergent beam electron diffraction |
| CNST | Center for Nanoscale Technology |
| DI | Deionized |
| DC | Direct current |
| EBID | Electron beam induced deposition |
| EFTEM | Energy filtered transmission electron microscopy |
| eV | Electron Volt |
| FIB | Focused ion beam |
| Ga | Gallium |
| $Ga^+$ | Gallium ion |
| Ge | Germanium |
| HAADF | High angle annular dark field |
| HAADF-STEM | High angle annular dark field-scanning transmission electron microscopy |
| HF | Hydrofluoric acid |
| $H_2O$ | Water |
| $h_c$ | Critical thickness |
| HCl | hydrochloric acid |
| IMEC | Interuniveristy microelectronics center |
| IR | Infrared |
| MBE | Molecular beam epitaxy |
| MFP | Mean free path |
| Nav-Cam | FIB navigation camera |
| NIG | Nude ion gage |
| NIST | National Institute of Science and Technology |
| PbSe | Lead selenide |
| PbTe | Lead telluride |
| PSDF | Power spectrum density function |
| PTEM | Plan view transmission electron microscopy |
| QD | Quantum dot |
| QDGFET | Quantum dot gate field effect transistor |
| RCA-2 | Oxidzing cleaning solution created at RCA laboratories by Werner Kern |
| RGA | Residual gas analyzer |
| RHEED | Reflected high energy electron diffraction |

| | |
|---|---|
| SEM | Scanning electron microscope |
| Si | Silicon |
| SIMS | Secondary ion mass spectrometry |
| SiN | Silicon nitride |
| SK | Stranski-Krastanow |
| STEM | Scanning transmission electron microscopy |
| STM | Scanning tunneling microscopy |
| TEM | Transmission electron microscopy |
| TIF | Tagged image file format |
| ToF-SIMS | Time of flight secondary ion mass spectroscopy |
| UHV | Ultra high vacuum |
| XTEM | Cross sectional transmission electron microscopy |

## List of Symbols

| | |
|---|---|
| Å | Angstrom |
| $a_{Ge}$ | Lattice parameter for Germanium |
| $a_{Si}$ | Lattice parameter for Silicon |
| $a_{Si(1-x)Gex}$ | Lattice parameter for Silicon and Germanium mixture |
| $c$ | constant |
| $C$ | Coulomb |
| $D$ | Diffusivity |
| $D_0$ | Exponential prefactor |
| $\Delta E$ | change in energy |
| E | Energy |
| $E_b$ | Surface binding energy |
| $E_c$ | Critical energy |
| $E_m$ | Energy of migration |
| $\varepsilon_{coh}$ | Coherent strain |
| $F$ | Force |
| $\gamma$ | Surface free energy/figure of merit |
| $\gamma_e$ | Free energy of the faceted edge |
| $\gamma_s$ | Free energy of the normal surface |
| $\gamma_w$ | Free energy of the wetted surface |
| $I$ | Ion current |
| $\varkappa$ | Surface curvature |
| $k$ | Spring constant |
| $\Gamma$ | Change in surface energy |
| $\lambda$ | Light source wavelength |
| $\lambda_{ATG}$ | Asaro-Tiller-Grinfeld instability wavelength |
| $\lambda_{MFP}$ | Gas mean free path |
| $\lambda_n$ | Surface pattern wavelength |
| $M$ | Biaxial modulus |
| $\mu$ | Shear modulus of the substrate |
| $\mu_0$ | Chemical potential of a planar surface |
| $N_A$ | Avogadros's number, 6.023 x $10^{23}$ |
| $\nu$ | Poisson's ratio |
| $\Omega$ | Atomic volume |
| $R$ | Resistance; Gas constant |
| $\rho$ | Density |
| s | Standard deviation |
| $\sigma$ | In-plane stress |
| Si | Silicon |
| $T$ | Temperature |
| $t$ | Dwell time |

| | |
|---|---|
| $\vartheta$ | Contact angle, emission angle |
| $V$ | Volume |
| $V_c$ | Critical volume |
| $\langle V \rangle$ | Mean volume |
| $x$ | Deflection |

# Acknowledgements

Few people get an opportunity in life that I have been afforded through the generous support of the Materials Science and Engineering Department, at the University of Virginia. Through my past teaching experience I have really been able to truly appreciate the opportunity to learn all that I have over the past few years. I would like to thank Prof. Jerry Floro for guiding me on this journey. His support and enthusiasm, through missteps and voids has made reaching this point possible. He has been remarkable in his support and guidance, and most especially his patience. There are few people I have ever met with so dedicated and unselfish purpose as he is to sharing his love of science and education.

I would also like to thank my committee: Prof. Reinke, Prof. Wolf, Prof. Hopkins, and Prof. McDonnell who have graciously agreed to serve in this purpose and at times allow me access to their labs and students to make this research possible.

I would like to acknowledge the assistance of Joshua Schumacher at Center for Nanoscale Science and Technology, NIST in Gaithersburg, for his assistance with the FIB and patterning, James Tuggle at Virginia Polytechnic Institute, and especially James Maier at Pennsylvania State University for his exceptional liftout skills.

I would like to thank the Department of Materials Science and Engineering, the faculty, staff, and students who make the department the world class facility that it is. I would also like to thank my lab mates and fellow students both past and present: Dr. Chris Petz, Dr. Joseph Kassim, Dr. Priyah Ghatwai, Naiming Liu, Eric Vetter, Copeland Kell, Wade Jensen, Rob Golden, Matt Schneider, Gopal Ramalingam, Ehsan Monazami, and especially Jatin Amatya.

I would like to extend a special thank you and acknowledgement to Carl and Margot Johnson, whose personal generosity and commitment to science education through the II-VI foundation has made this project and research possible.

I dedicate this to Felix and Edward who had a passion to make things work, but never had the opportunity of higher education, and to my father, Ronald, whose example made a doctorate a lifelong ambition. Finally, without whom, what's the point? To my children: Sarah, Jessica, Jacob, and Samuel, thank you for all your encouragement. I hope this serves as an inspiration to you, and Linda, the yin to my yang, the butter to my toast, and love of my life, without whom this is an unrealized dream, here it is.

# Abstract

A quantum dot mesocrystal (QDMC) is a three-dimensional, spatially ordered array of quantum dots (QDs) epitaxially embedded in a matrix material. By manipulating the QD array, e.g. size, periodicity, symmetry and chemical composition, we can potentially tailor the electrical, thermal, optical and magnetic properties of the crystal. While the dots themselves possess size-dependent properties due to electronic confinement and discrete energy states, bringing the quantum dots close enough together on the nanometer scale can result in electron wavefunction overlap and extended state or even miniband formation. Control of these properties can lead to potential applications in optoelectronics, nanoelectronics and thermoelectrics.

The strategy for forming ordered three-dimensional QDMCs of Ge on and in Si (001) is to encapsulate a well-ordered two-dimensional array of Ge QDs. Self-assembly of the ordered 2D array is directed by a surface topographical pattern pre-imposed on the substrate. Embedded Ge QDs create an inhomogeneous strain field in the Si encapsulation layer, onto which additional Ge is deposited. The strain field drives the nucleation to sites directly over the embedded QDs, thereby replicating the layer underneath. Repeating this process can result in a highly ordered QDMC. The challenge is to achieve this at lengthscales near or below the intrinsic lengthscale of the QDs themselves. The latter is dictated by the competition between elastic and surface energy.

The first part of the thesis discusses the directed formation of Stranski-Krastanow Ge QDs by molecular beam epitaxy (MBE). Highly uniform arrays are produced using a Ga+

focused ion beam (FIB), in conjunction with wet chemistry, to create surface morphology conducive to QD growth at ion doses considerably less than previously reported. This enabled successful self-assembly down to at least 50 nm interdot spacing, which is much less than previously achieved using FIB. Localization of the QDs can be achieved by creating topographical features, e.g. pits, that lower the barriers to formation through geometry, strain, or surface energy anisotropy. At the optimal dose, FIB patterned substrates at 50 nm create a template that nucleates QDs with a narrow normalized volume distribution width, with very high occupancy. The formation of the QDs is not in the pits, which is typical, but in the four-fold "crown" region in between the pits. We discuss the competing mechanisms that drive the nucleation of the QDs. The effect of buffers, deposition thickness, and temperature are explored.

The second part of the thesis discusses the formation of three-dimensional QDMCs on the 2D seed layers of Ge QDs. While atomic force microscopy suggests that high-fidelity multilayer replication of the initial, patterned layer can occur, cross-section transmission electron microscopy reveals complex behavior. For example, in several instances, extreme pattern morphology was completely undetected by the AFM. Although these morphologies are not optimal for QDMC formation, they also provide interesting insights into the propensity for self-assembly in this system. The limitations of the FIB for patterning at 50 nm and below will be discussed.

# 1 Introduction

Quantum dots (QDs) possess significantly altered density of states relative to bulk material counterparts, because of electronic confinement in all three dimensions. They have been described as artificial atoms, which, when incorporated into a confining matrix, can lead to materials with entirely new electronic and optical properties. However, there exist significant challenges fabricating such material systems, due in part to the idiosyncrasies of the constituent materials, and to the requisite length-scales. Material fabrication on the nanometer scale is technologically challenging and can be greatly simplified in principle by self-assembly processes. Fabrication of discrete structures for nanoelectronic applications at the size required for quantum confinement is further complicated by requirements for size uniformity, composition, positional accuracy and interdot distance.

Crystal growth of Germanium (Ge) on Silicon (001) by vapor-phase heteroepitaxy follows a Stranski-Krastanow (SK) growth mode where 3D islands form after an initial planar wetting layer reaches a critical thickness. This transformation is driven by a reduction in elastic energy due to the 4% lattice mismatch between Si and Ge. These 3D islands are coherently strained, [1,2] and as such, given their small dimensional size, can effectively confine charge. [3] Subsequent research on SK-based self-assembly focused on a variety of topics including fundamental growth mechanisms, growth uniformity, multilayer structures and superlattices, and directed growth. Novel electronics have been proposed that require coupling between adjacent QDs, requiring interdot distances of less than 10 nm. [4–7] One recent conception incorporates quantum dot structures in multi-valued logic devices. In a quantum dot gate field effect transistors (QDGFET) layers of quantum dots are located between the gate contact and the gate insulator. The QDGFET exhibits an intermediate state in between on “on” and “off” because of stored charge in the quantum dots. [8]

Another application where the inclusion of quantum dots has potential benefits is in Si-Ge thermoelectrics. The thermoelectric figure of merit is enhanced first by reducing the thermal conductivity by the inclusion of nanostructures, and increased phonon scattering. Secondly, the electrical conductivity is enhanced through enhanced electronic flow through high-mobility conduction channels that arise due to electronic confinement in the Si matrix in between the dots. The improvement is predicted to be particularly acute at lower temperatures, i.e. 200 °K, but persists to higher temperatures as well. [9,10]

Finally, Ge QDs have shown photoluminescent properties in the mid IR range making them attractive candidates for detector applications at this wavelength. [11–13] Electroluminescence has also been demonstrated indicating the potential for on chip LEDs. [14–16] Additional research is driven by a search for pathways to ever smaller and faster electronic devices, as well as silicon integration technology.

For many applications, the requirements of size uniformity, positional accuracy and interdot distance pose a challenge as they represent non-equilibrium conditions for unconstrained quantum dot growth. Directing self-assembly by means of changing the substrate surface morphology has been an effective means for producing highly uniform arrays of QDs using the SK transition, and not only allows for positional control, but reduces the critical volume size for QD nucleation relative to QD formation on a planar surface. [17] The reduction in critical volume permits reduced interdot distance, overlapping strain fields between dots, and the potential for exchange interactions in the lateral plane. Modification of the surface has been achieved by means of lithography, [18–20] nano-indentation [21] and ion-beam processing. [22–25] The various techniques and experiments cover a large range of surface features to direct the growth including pits, [18,19,22] stripes, [26–28] mesas, [29,30] and oxide windows, [31] as well as a wide range of QD areal density, growth temperatures, composition and deposition thickness. We have investigated the use of a Ga+ focused ion beam (FIB) to direct write patterns on Si (001) surfaces to direct precise positioning of Ge QDs at sub-100 nm lengthscales.

## 1.1 Si/Ge heteroepitaxy

The first transistor was made using a bulk Ge crystal, but because of an insufficiently stable oxide, Ge was replaced when Si processing became capable of providing sufficiently pure material despite Ge's superior electronic properties. There has been an exponential growth in transistor density since. Moore's law is often invoked as motivation for research, and as downscaling of silicon based integrated circuitry continues, Ge has emerged as an important material in fabrication. In particular, Ge is alloyed with Si in order to strain the materials and enhance the mobility of the carriers within the Si channel. This trend is expected to continue until at least the 7 nm node and possibly longer. [32]

The combination of similarities and slight differences of Ge and Si make it such a unique and intriguing material system. Ge and Si are group IV semiconductors, and share the diamond cubic crystal structure. They are completely miscible and readily alloy (Figure 1-1: binary phase diagram). The lattice constants are $a_{Si}$ = 5.431 Å and $a_{Ge}$= 5.658 Å @ 300 °K.

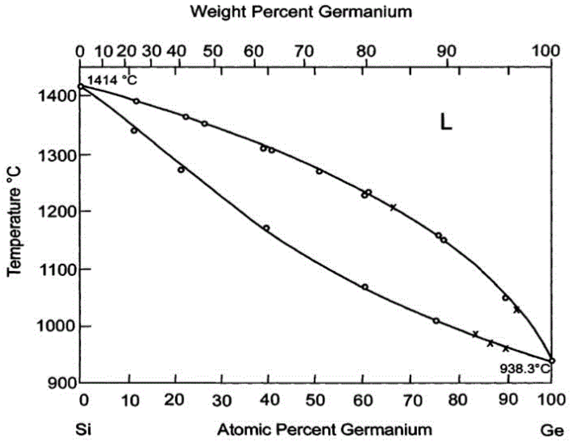

**Figure 1-1: Binary phase diagram for Si-Ge**

For Ge and $Si_{1-x}Ge_x$ films deposited directly onto a Si substrate, a biaxial stress and tetragonal strain results for a fully coherent film given by: [33]

$$\varepsilon_{coh} = (a_{Si}-a_{Ge})/a_{Ge} \qquad \text{Equation 1-1}$$

The lattice parameter for an unstrained $Si_{1-x}Ge_x$ alloy film can be approximated by Vegard's law:

$$a_{Si(1-x)Gex} = (1-x)a_{Si} + x\, a_{Ge} \qquad \text{Equation 1-2}$$

It has also been experimentally fitted for Si and Ge [34] to capture the small degree of bowing in the lattice parameter:

$$a_{Si(1-x)Gex} = (5.431 - 0.20x + 0.027x^2)\,\text{Å} \qquad \text{Equation 1-3}$$

The work of Dismukes was verified by Kasper et al. in thin epitaxial films. [35] The lattice mismatch and the elastic strain energy that develops within a film due to the lattice mismatch, (Fig. 1-2) is a primary driver for many of the features of Ge film including the 3D islanding by SK growth, and modified band structures. Because Si and

Ge are completely miscible, a continuous range of film alloys is possible, and as a consequence, the lattice parameter and resulting strain can be controlled precisely, leading to a host of engineering possibilities.

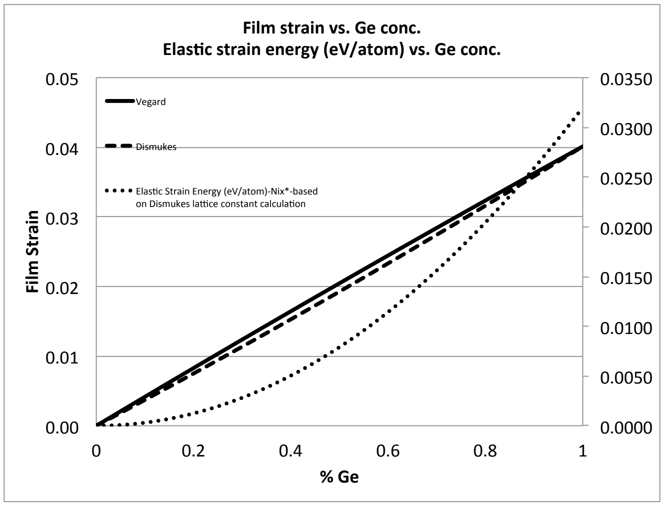

**Figure 1-2: Quantum dot formation on planar surfaces**

On planar Si (001) surfaces, deposited Ge forms a strained wetting layer. The elastic strain energy increases linearly with increasing thickness until nucleation of faceted 3D islands, [1,2] (a.k.a. “huts” or “pyramids”, defined by special {105} facets) occurs. With pure Ge, the critical thickness $h_c$ of the wetting layer is between 3-4 ML. [1,36]. The formation of 3D islands reduces the elastic strain energy at the expense of increased surface energy. Once formed, the 3D islands typically coarsen and undergo a progression of shape transformations in order to reduce free energy as they grow in volume. [37–40]

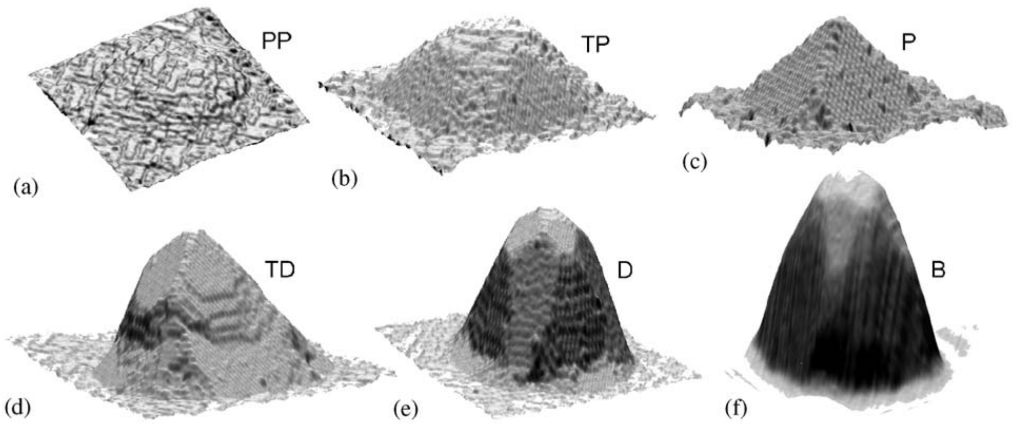

**Figure 1-3: STM and AFM images of representative islands during evolution of SiGe islands on Si (001): (a) pre-pyramids (PP), (b) truncated pyramids (TP), (c) pyramids (P), (d) transition domes (TD), (e) domes (D), (f) barns (B)** [41]

QDs grown in this manner are limited with regard to technical applications, as the dots are randomly positioned, with a broad size distribution and often a low areal density (number of QDs per area). Applications that require exchange interactions between the quantum dots, especially in the lateral space, typically require precise positioning, small inter-dot distances, i.e. < 10 nm, and a uniform size distribution. Uniform size distributions are particularly important for optoelectronic applications, as size relates directly to wavelength through confinement, and wide distributions lead to signal broadening.

A simple model to calculate energetics involved in the nucleation of islands was presented by Tersoff and Tromp (1993) where the increase in surface area energy due to the formation of the islands is offset by a decrease in elastic strain energy. [42] For an island shaped as a trapezoidal prism there exists an energy per unit volume (E/V) minimum for a fixed aspect ratio faceted QD (e.g. {105} faceted hut.) The existence of this minimum indicates that there is an energetic barrier (i.e. nucleation energy) to the formation of islands. Tersoff reformulated the calculation for the change in free energy upon island formation: [43]

$$\Delta E = 4\Gamma V^{2/3} \tan^{1/3} \theta - 6cV \tan\theta \qquad \textit{Equation 1-4}$$

where Γ represents the change in surface energy given by the expression:

$$\Gamma = \gamma_e \csc\theta - \gamma_s \cot\theta. \qquad \textit{Equation 1-5}$$

where $\gamma_e$ and $\gamma_s$ are the surface free energies of the facets and the normal surface, $\theta$ is the contact angle of a faceted edge, $V$ is volume, and $c$ is given by $\sigma^2 (1-\nu)/2\pi\mu$, where $\sigma$ is the in plane stress, $\nu$ is Poisson's ratio and $\mu$ is the shear modulus of the substrate.
There exists a maximum energy, which is plotted in Fig. 1-4:

$$E_c = 64\Gamma^3 \cot\theta \,/\, 243c^2, \text{ when } V_c = (4\Gamma/9c)^3 \cot^2 \theta. \qquad \textit{Equation 1-6}$$

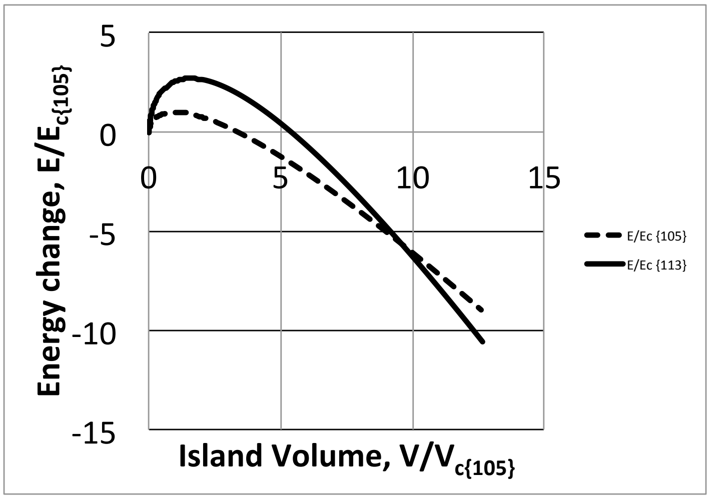

**Figure 1-4: Change in free energy of a strained layer forming {105} and {113} faceted islands of volume V. The curves are normalized to the critical values $E_c$ and $V_c$ for the formation of the {105} faceted island.** [44]

From Fig. 1-4 it can be seen that there exists an energetic barrier for direct nucleation of {105}-faceted islands at a critical volume and subsequently as the volume of the island increases the free energy change is reduced and eventually becomes negative. A larger energy barrier exists for {113} faceted islands at a correspondingly larger critical volume, and that there exists a volume above which {113} faceted islands are energetically preferred. The empirical progression of Ge island shapes is well documented. [37,45,46] Following the transition from {105} faceted pyramids to {113} domes (these are actually multi-faceted, but {113} is a dominant facet), islands will progress to barns [39] and finally to superdomes [47] where misfit dislocations dramatically reduce the elastic strain energy. One paper provides a surprising result, not corroborated, that at high enough growth temperatures, i.e. > 675 °C, domes are the first stable islands to form, and interestingly do not preclude the formation of pyramids. [48,49] This seemingly thermodynamic violation occurs because there is a small window in the wetting layer thickness where domes are stable, but pyramids are not.

In Tersoff, et. al.'s nucleation-based theory, $E_c$ scales inversely with strain: $E_c \sim 1/e^{-4}$, while $V_c \sim 1/e^{-6}$. While nucleation of discrete islands has been observed in films with high misfit strain, such as Ge on Si (001) in real-time, [50,51] the increasing nucleation barrier in $Si_{1-x}Ge_x$ films with lower misfit strain precludes the nucleation of islands. Roughening of the film surface in the low misfit regime is often attributed to an *instability* driven by strain. Similar surface roughening mechanisms, referred to as the Asaro-Tiller-Grinfeld instability (ATG), [52,53] have been observed in metals and other semiconductor films. [54] Discontinuities in the film surface reduce the overall elastic strain energy provided that the "ripples" exceed a characteristic wavelength. Island formation in lower strain films is a nucleation-less process. The "ripples" grow in thickness and steepness until a low energy facet is formed. The faceted ripples may then coarsen. A theory for the instability in the presence of surface energy anisotropy provides a relevant connection between the pure instability and pure nucleation extremes. [55]

## 1.2 Directed quantum dot formation

Attempts to create spatial ordering purely by self-assembly have been successful only in the II-VI material system, [56] where large elastic anisotropy in PbSe/PbTe superlattices leads to lateral ordering of the PbSe quantum dots within a few repeat layers, thereby creating a quantum dot mesocrystal with no imposed patterning of the substrate. Ge QDs on Si (001) in QD superlattices will replicate their positions vertically, [3,57] but there is no long-range lateral order. Other strategies to self assemble ordered QDs include growth on vicinal surfaces. [58–62] Quasi-periodic one-dimensional patterns are created by step bunching during Si buffer growth on miscut surfaces along the <110> direction. Zhong et al deposited a 100.0 nm Si buffer, on a 4° miscut wafer which formed a rippled surface with a 100 nm pitch. Deposition of 5.0 nm of $Si_{0.55}Ge_{0.45}$ at 625 °C resulted in a rows of dome shaped QDs spaced at 70 nm along the ripple flanks. Embedded dislocation networks are also effective at directing the nucleation of QDs. [63–65] Ge QDs grown on relaxed buffers first nucleate at the intersection of dislocations lines. QDs then form on dislocation lines with additional coverage, and finally within the areas between the lines. [65] However, the dislocation arrays themselves have random inter-dislocation spacing, and hence do not provide periodic or controllable spatial patterning. These results do further confirm, however, the surprisingly important role that rather small strain gradients on the free surface play in directing the nucleation of quantum dots.

A number of studies have directed the formation of the QDs by creating openings in a surface oxide that masks the Si substrate. This has been accomplished with an STM tip, [66] or wet chemical etching through a SiN shadow mask patterned with e-beam lithography. [31,67] The exposed underlying substrate will nucleate Ge QDs within the exposed regions.

Photolithography has been used to create many structures on which QDs have been formed including stripes, [68–70] mesas, [27,29,71] and pits. [18,20,72] While elastic strain energy still drives the formation of QDs, diffusion of Ge on non-planar surfaces is additionally influenced by surface free energy. The chemical potential of a curved surface can be described: [54,70]

$$\mu(x,y) = \mu_0 + \Omega\gamma\varkappa(x,y) + \Omega E_s(x,y) \qquad \textit{Equation 1-7}$$

The first term ($\mu_0$) is the chemical potential of the planar surface, the second term describes the effects of surface curvature ($\varkappa$) on the chemical potential through the surface energy anisotropy, where $\Omega$ is the atomic volume, and $\gamma$ is the orientation-dependent surface energy. The third term describes the effect of strain relaxation associated with surface curvatures. As the surface chemical potential is a minimum with negative curvature, it is expected that surface diffusion of surface adatoms or addimers will drive mass transfer into pits or other concave features. Fig. 1-5 shows four examples of directed nucleation using larger features, e.g. stripes and mesas. In two of the four instances (a) and (b), there is formation of quantum dots on regions of positive curvature. This suggests that strain relaxation plays an important role in the locating of QDs on non-planar surfaces, because without strain energy there is no barrier to Ge migration into the concave regions. Yang et al. [70] calculated the local chemical potential across a ridge, accounting for strain relaxation and determined that there exists a local minimum at the crown of the ridge. Single aligned rows of QDs form at the crests of the ridges (Fig. 1-5 (b)). Kitajima et al. [29] observed the formation of QDs on top of mesas. On large mesas, e.g. 600 nm wide, the QDs formed on the corners, presumably where the local strain energy is at a minimum. With decreasing mesa size the QDs form closer together, ultimately coalescing. They obtained a one-to-one correlation between dots and mesas when the mesas were 140 nm across (Fig. 1-5 (c)). Meanwhile, Zhong, et al. observed different behavior in the positioning of QDs on stripes, which he successfully manipulated with the inclusion of a strained buffer. [68,73] On an unstrained buffer, QDs formed within the ridges of the stripes with sufficiently high growth temperature, e.g. 650 °C. (Fig. 1-5 (d)) He attributes the lack of formation of QDs on the top of the terrace to the Ge wetting layer not reaching a critical thickness despite 7 ML (i.e. beyond critical) of Ge being deposited overall. This suggests there is a net flux of adatoms to the valleys. At a lower growth temperature (600 °C), QDs form both at the top and within the ridges.

For this experiment a four step buffer growth was used. The first and second steps were identical, but for step three, pure Si was deposited in one case, and a five period superlattice consisting of 20 Å$Si_{0.5}Ge_{0..5}$ / 30 Å Si in the other. In both cases, 80 Å of Si is deposited as the final buffer step. Despite the lowering of the strain at the top of the pattern, and in principle reducing the driving force for on top nucleation, the strained buffer layer creates an inhomogeneous strain layer at the edges of the top surface where the Ge layer is partially relaxed. This acts as a barrier for atoms to hop down the slope, and in fact the activation barrier is lower for atoms to hop up. There is sufficient material on the top surface to nucleate QDs. [73]

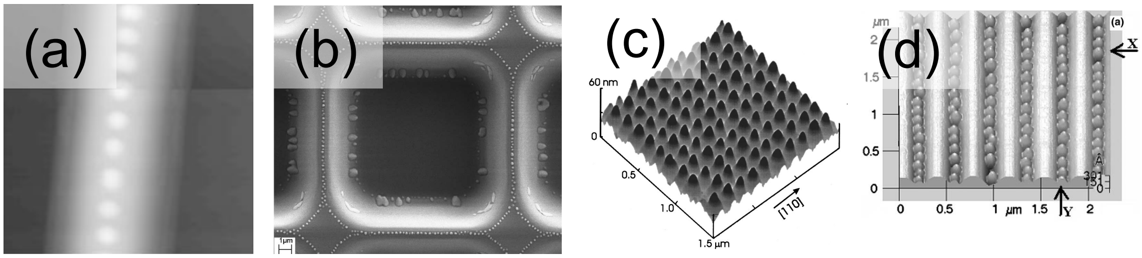

**Figure 1-5: (a) QDs formed on a 700 nm wide mesa.** [27] **(b) Ge QDs forming at the local minimum on top of the ridge and large Ge crystals at the feet of the sidewall.** [70] **(c) Ge QDs formed on top of 140 nm Si mesas.** [29] **(d) Ge QDs formed between Si stripes.** [68]

## 1.3 Pit induced quantum dot formation

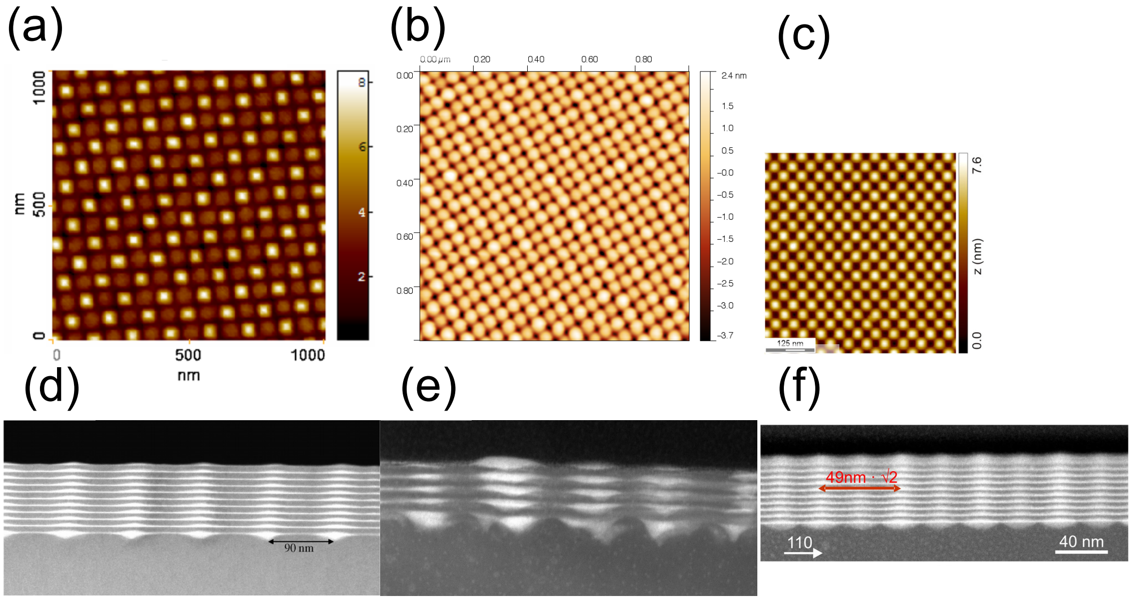

**Figure 1-6: Evolution of ordered high-density QDs patterns: (a) 90 nm pitch .** [19,74]**, (b) 50 nm pitch.** [75] **(c) 35 nm pitch, scaled to match lateral dimension of (a) and (b)** [7]**. (d) 10 layer QDMC at 90 nm.** [74]**. (e) 5 layer at QDMC 50 nm pitch (thesis). (f) 10 layer QDMC at 35 nm .** [7]

There has been tremendous success in growth of Ge QDs in lithographically produced pits for both patterns having high areal density (Fig. 1-6 (a) and (c)), [19,76] and for lower areal density patterns with inter-dot distances up to 3.4 µm (Fig. 1-7). [20,68] Advantages of lithographic methods include parallel processing, highly repeatable surface features, and an undamaged substrate. In interference lithography the pattern resolution (pitch) is limited by the light source wavelength.

$$\mathit{pitch} = \lambda/2 \qquad \textit{Equation 1-8}$$

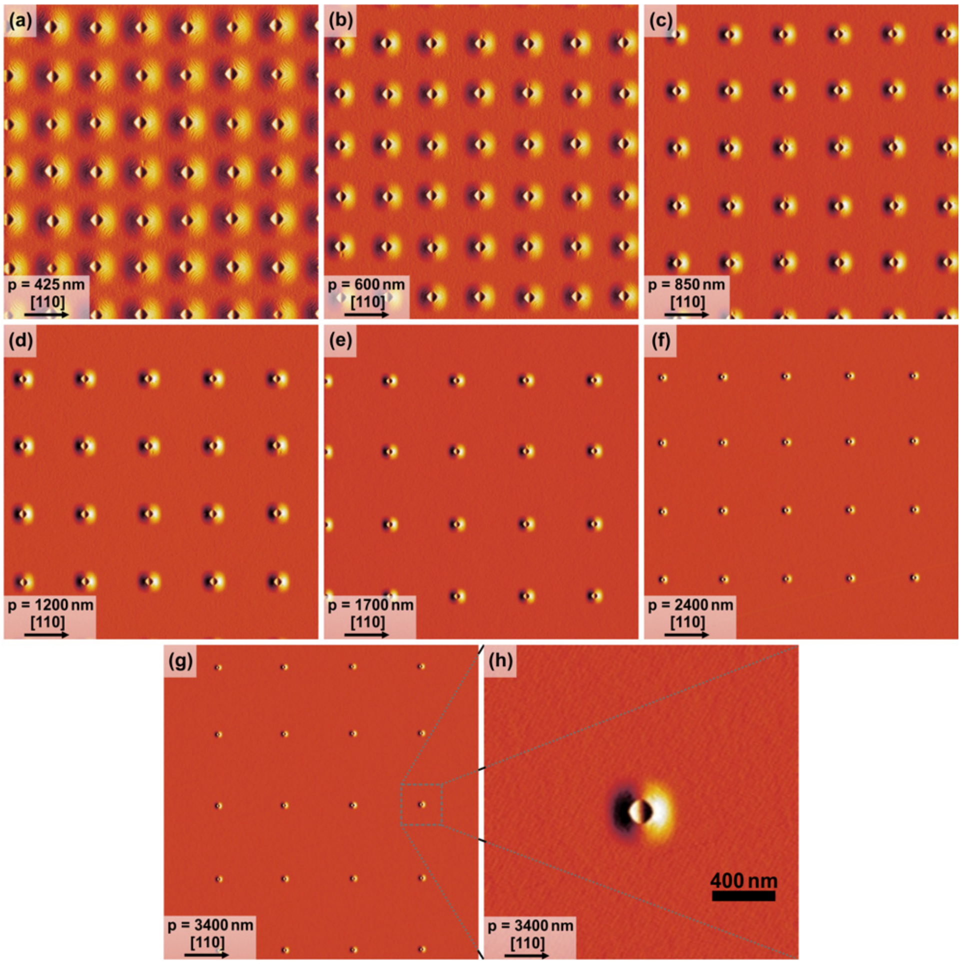

**Figure 1-7: AFM micrograph in derivative mode, 3ML of Ge deposited on a Si substrate at 700°C. Patterns of various inter-pit distance from (a) 425 nm to (g) 3,400 nm were grown simultaneously. The detail of a single pit is shown in (h).**

This has limited pattern density in the past, but use of EUV lithography, has brought interference lithography to pitches below 50 nm. [19] Regardless, high quality arrays have been created where QDs nucleate within pits formed in the substrate by carefully controlling the pit morphology, including pit sidewall angle, pit size uniformity, pit period, film thickness, growth temperature (Fig. 1-7). In optical lithography, photo-resist is exposed and patterns are etched into a surface via wet chemical etch or reactive ion etching (RIE). Pit *morphology* is controlled through the diameter of the etched pit growth of a buffer (Fig. 1-8). Vastola et al. demonstrated how the pit shape, in particular the sidewall angle, influences the nucleation location of the islands. [20,77] For sidewall angles less than 5°, smoothing and filling of the pit occurs without the formation of a QD initially. Pits with sidewall angles between 5° - 18° are shown to be optimal for forming QDs (Fig. 1-9).

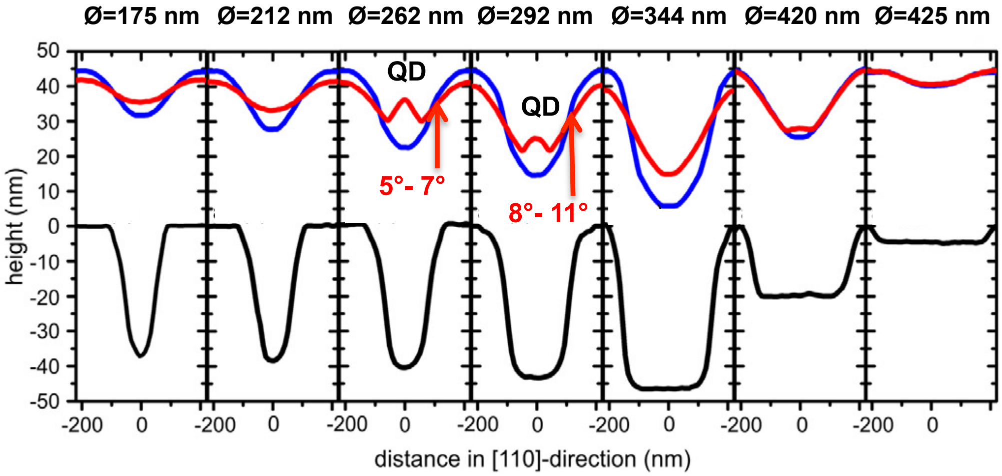

**Figure 1-8: Influence of the etched pit dimension and buffer growth on pit morphology and QD growth. Linescans through the middle of pits before growth (black), after a 45 nm Si buffer growth (blue) and 3 ML of Ge deposition (red). The profiles are offset using a conservation of volume. Si diffusion is enhanced by the presence of Ge, resulting in a smoothening of the underlying substrate profile.** [20]

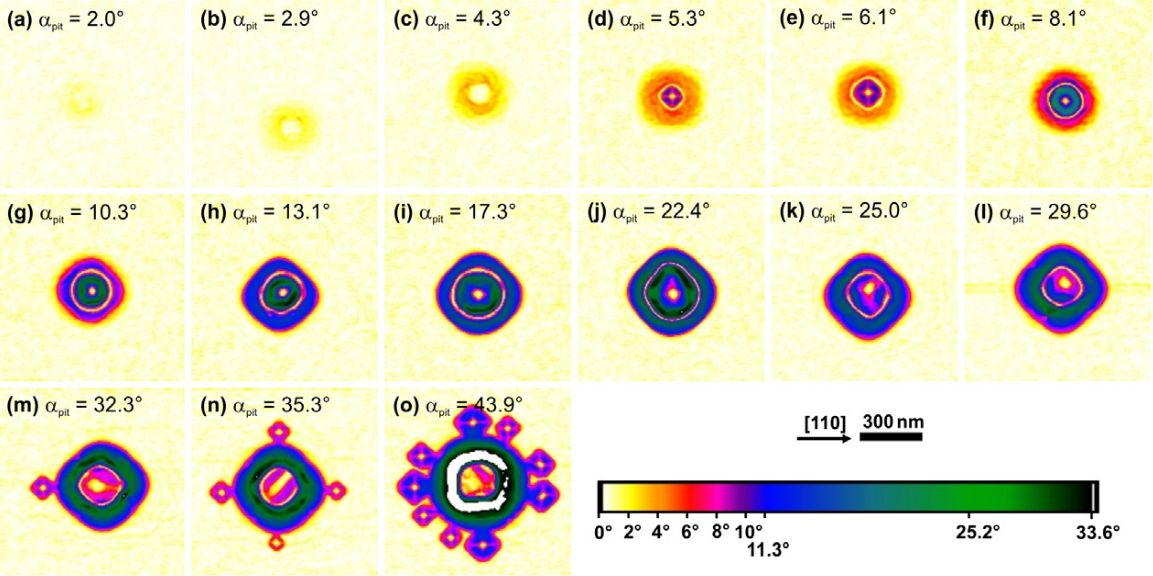

**Figure 1-9: Local slope plots of pits and QDs relative to the substrate surface, Si (001), indicating the positioning of QDs relative to the pits as a function of sidewall angle. The range of sidewall angles is created by varying the diameter of the etched pit from (a) 150 nm to (o) 295 nm.** [20]

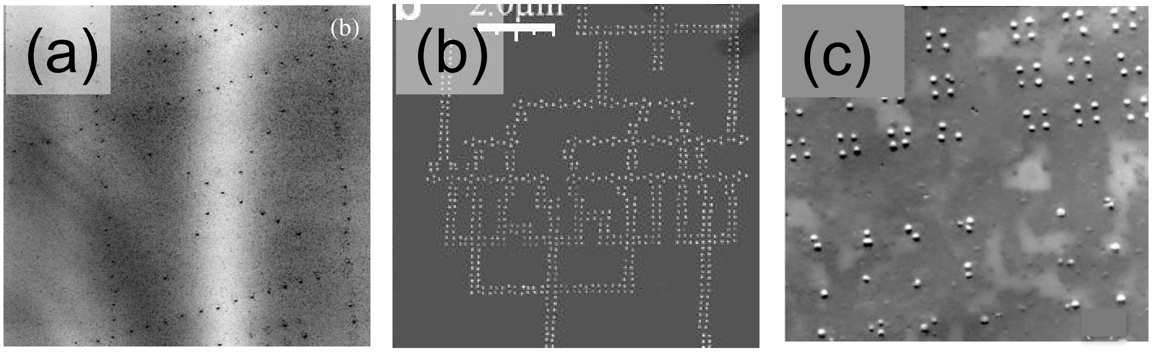

**Figure 1-10: Ge QD growth on FIB patterned surfaces. (a) 3.5 µm x 3.3 µm plan view transmission electron microscopy (PTEM) micrograph: 5 ML of Ge deposited on a 6K ion/dose pattern after annealing 15 min at 600°C.** [24] **(b) 10 µm x 10 µm AFM: Ge QD array in the form of a QCA adder circuit. Dose: 7K ions/site. Pattern was annealed for 1 min at 550°C.** [78] **(c) 2.5 µm x 2.1 µm PTEM: Ge QD clusters at different pitch, 45 nm lower right (LR), 60 nm (LL), 105 nm (UL), and 120 nm (UR). 18K ions/site.** [79]

In the experiments referenced in Fig. 1-10, the patterning and growth were conducted in a contiguous vacuum, i.e. the samples were never exposed to atmosphere and so there is no oxidation of the surface in between process steps. It is a three-stage process: patterning with FIB, annealing of the patterns, and finally growth. The critical step in this approach is the annealing of the patterns. Kammler et al. showed increased substrate damage with increased FIB exposure, with the affected areas increasing from 90 nm in diameter at 6000 ions/site to 320 nm in diameter at 600,000 ions/site. [22] While a pit still remained in the substrate surface at a dose of 600,000 ions/site following an anneal at 750 °C for 15 min, there were no surface features remaining for the sites exposed to only 6,000 ions/site. The pattern shown in Fig. 1-10 (a) was achieved on a 6,000 ion/site pattern followed by a 15 min annealing at 600 °C. Portavoce et al., Fig. 1-10 (b), demonstrated highly directed patterns with a 7,000 ion/site dose and an annealing at 550 °C of only one minute. [25] It was determined that the small morphological changes to the surface were responsible for nucleation of the QDs at sub-critical thickness. Annealing helps restore crystallinity to the FIB patterned sites but that a net sputtering of material results in small shallow pits. Experiments where annealing was performed at higher temperatures (e.g. 650 °C), for prolonged time (15 min) produced random nucleation similar to un-patterned substrates.

It is important to realize that in most of this work, the interdot spacing of these patterns is considerably larger than 100 nm. Gherasimova et al., [79] Fig. 1-10 (c), investigated cluster patterns where the interdot distances are less than 100 nm within each cluster. Nucleation does not occur simultaneously within a cluster, and the first dot(s) to nucleate take the available adatoms and inhibit the nucleation of QDs at other cluster sites, resulting in incomplete clusters.

Other research has been done in directed QD formation using a FIB based approach, with separate FIB and growth chambers, thus requiring cleaning and oxide desorption post patterning. [80–82] Arrays of 28 x 28 sites were patterned with a 30kV ion beam at a current of 1 pA, with a nominal beam size of 10 nm. The total pattern time is reported which correlate to a range of ions doses between 8000 ions/site to over 600,000 ions/site. They report a process where the samples are then cleaned in a HCl:$H_2O$ solution, annealed at 950 °C, and then re-cleaned in HCl. The removal of Ga was verified to be below the detection limit of SIMS, i.e. less than $10^{16}$ $cm^{-2}$. The samples are then loaded for growth, desorbed at 900 °C for 2 minutes to remove the native oxide and a 4 nm Si buffer is deposited at 750 °C. They report no change in the surface morphology between the second HCl cleaning and the deposition of the Si buffer.

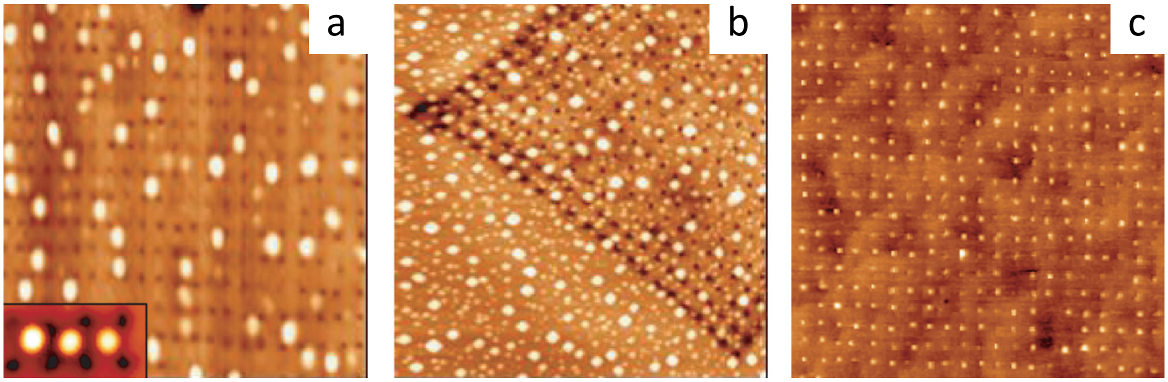

**Figure 1-11: 8 ML (1.4 nm) Ge deposited on FIB patterned Si (001) subtrates. (a) 180 nm pitch at 750 °C, (b) 350 nm pitch at 750 °C, and (c) 200 nm pitch at 550 °C. Deposition rate of 0.3 Å/s.** [83]

In Fig. 1-11, 8 ML Ge was deposited at two different temperatures: 750 °C, Fig. 1-11 (a) and (b), and at 550 °C, Fig. 1-11 (c). At high temperature, large Ge QDs nucleate on the planar regions between the pits, with good positional accuracy, but low site coverage. However, at low growth temperature, QD formation is highly correlated to the underlying pattern, forming only in the pits. They speculate that in the lower temperature regime, the QDs form in the pits because there is insufficient thermal energy for the Ge atoms to escape the stepped walls of the pits, whereas, at higher temperatures, the Ge atoms are sufficiently mobile to escape the pits and locate preferentially at a chemical potential minima on the terrace near the pits. [80]

In summary, there is strong experimental evidence that templated pits on a Si (001) surface result in the directed nucleation of QDs, and that this templating can be achieved with use of a FIB. Our research builds on this base, in which we created state of the art arrays of quantum dots on considerably shorter lengthscales, and characterized them with atomic force microscopy (AFM). We also generated multilayer structures which we were able to examine with transmission electron microscopy (TEM) to understand some of the complex underlying morphology. There were a number of unexpected results that will be discussed in the context of the existing literature summarized above.

## 1.4 Thesis Organization

The thesis is organized in the following manner: in chapter 2, the experimental methods are discussed, including extensive discussion of AFM as it is used extensively in this thesis work. In chapter three, some preliminary work is discussed, and the challenges that were faced in forming the initial patterned arrays of QDs are highlighted. Chapter 4 is more intensive, dedicated to the formation and characterization of two-dimensional arrays of QDs. The attributes of the arrays are described in detail, which is followed by extensive discussion related to the formation mechanisms involved, as some of the results are surprising. In chapter 5, the formation and morphology of our QDMC growths is discussed. A cross sectional TEM sample is thoroughly dissected, as it leads to many insights into the key elements leading to the particular morphologies that we see. The conclusions of our work are detailed in chapter 6.

# 2 Experimental methods

*A coupla months in the laboratory can save a coupla hours in the library.- Westheimer's Discovery*

High quality, low defectivity epitaxial growth on Si requires stringent sample cleaning and surface preparation. As our FIB (patterning) and MBE (growth) are isolated from each other, the patterned substrate requires cleaning prior to epitaxial growth. Depending on device requirements, various cleaning methods are available to prepare a sample prior to placing it within the ultra high vacuum (UHV) environment. As Si readily oxidizes, surface preparation requires the stripping of these oxides within the UHV chamber by flashing the sample at high temperatures, e.g. greater than 1200 °C [84], or alternatively passivating the sample surface with sub-stoichiometric oxides or hydrogen. Removal of the passivation layer can be achieved at significantly lower temperatures, e.g. greater than 800 °C for sub-stoichiometric oxides [85] or 550 °C for the hydrogen. [86] The growth and characterization of our arrays and crystals consists of the following sequence:

- Clean and passive oxidation of a blank wafer
- Focused ion beam (FIB) patterning
- Clean and HF strip of the wafer prior to MBE
- Hydrogen desorption and MBE growth
- Ex situ characterization

## 2.1 Sample preparation for FIB

Each Si substrate is cleaned prior to patterning to ensure that the condition of the substrate is as consistent as possible prior to patterning. Two inch diameter, undoped, single crystal Si (001) wafers with a miscut of <0.1 degrees are used except where noted. The miscut is specified to ensure as flat a wafer as possible, retain the effective four-fold symmetry of the surface, and to minimize the effect of step edges on adatom diffusion and subsequent quantum dot formation. Each wafer, in preparation for patterning, was scribed with an identifying mark (Roman numeral) and fiducial (sideways T) to keep track of the respective samples, and to aid in the location of patterns (see Figure 2-1). The wafers were then cleaned in an IMEC solution, rinsed in deionized water (DI) for 5 minutes, dipped in a 5% HF solution for 30 seconds to strip the native oxide, and then placed for five minutes in a home-built UV ozone chamber to create a passive oxide on the surface. Samples are stored in ambient conditions in polypropylene wafer boxes.

**Figure 2-1: Image of the wafer as loaded into the FIB**

## 2.2 Patterning with focused ion beams (FIB)

Patterning with a FIB involves surface bombardment with high energy ions in a highly focused spot. The individual ions interact with the substrate to displace the atoms by either ejecting them from the substrate (sputter), displace them within the substrate (recoil), or can transfer energy to electrons within the substrate (electronic scattering). Recoiled atoms can displace other atoms (recoil cascade) if they have sufficient energy. This cascade persists until enough energy has dissipated and the individual recoils can no longer displace additional atoms. In the case where large numbers of ions are used, net sputtering occurs and pits are milled into the substrate surface. When smaller numbers of ions are used the region becomes highly defective, but without measurable sputtering. We have determined that when the samples are cleaned in preparation for molecular beam epitaxy (MBE), the localized areas of high defectivity near the surface are etched away.

Patterning was performed on the FEI Helios Nano Lab Dual Beam at the Center for Nanoscience Technology (CNST) at the National Institute of Science and Technology (NIST) in Gaithersburg, MD. The Helios is a dual beam system incorporating both $Ga^+$ ion and electron beams to provide increased functionality, e.g. micromachining, material deposition, material analysis, and high-resolution imaging. An integrated pattern generator allows for complex processing and patterning of substrates.

The FIB generates high energy ion beams which are focused onto the Si substrate. The ion energy can be adjusted from 1 keV up to 30 keV: higher energy results in a net increase of recoils. Additionally, the implantation depth of the ions, i.e. where the ions ultimately lose their kinetic energy, increases with higher energy. The number of ions that impinge on the surface is the product of the current of the beam (I) and the dwell time (t), and the coulombic charge ($6.241 \times 10^{18}$ ions/A):

$$ItC = ions/site \qquad \text{Equation 2-1}$$

The current of the ion beam is controlled by selecting from a series of apertures. The initial size of the aperture is used to calculate the expected current through the aperture. The apertures are designated by an expected ion current, which can be misleading. *Through time and use the actual size of the aperture changes, and as a result so does the actual ion current.* The actual current of the beam can be periodically monitored, as a blanked beam will be redirected to a faraday cup for ion beam current measurement and monitoring. The smallest aperture is typically used because of the very low number of ions that are implanted at each site, and the smaller beam spot size.

The dwell time at any particular site is programmed into the pattern generator. There are a number of methods to generate patterns: imported bit maps, stream files, or use of the pattern module. The pattern module allows for the selection of shapes (e.g. circles, rectangles, odd polygons), their sizes, position, orientation, and pattern parameters. The pattern parameters include dwell time, spot overlap (i.e. distance from site to site), raster direction, and number of passes. Discrete points can be obtained by selecting a negative spot overlap. For example, the ion beam diameter at 30 kV and 1.1 pA is nominally 7 nm: setting the beam overlap to -1000% will result in the spots being separated 70 nm on center. This method was used for the generation of the majority of patterns.

Complex arrays of patterns can easily be generated with this approach. Fig. 2-2 shows a typical array of patterns. The advantage of using multiple patterns per wafer is that a large range of pattern parameters can be assessed in a single MBE growth. All of the FIB process variables are the same for each of the patterns with the exception of dose and pitch. This ensures that from pattern to pattern within the array: focusing condition; relative ion dose; cleaning and etching exposure; desorption; and MBE growth are consistent. This allows for direct correlation of the effects of dose and pitch on pattern and growth features. The array pictured below consists of a sequence of doses at both 50 nm spacing and 35 nm spacing. Patterning at 50 nm and 35 nm allows for comparisons of patterns with a 2X increase in QD density. The individual arrays are spaced 15 µm on center. The range of ion doses range from 20K to 350 ions/site.

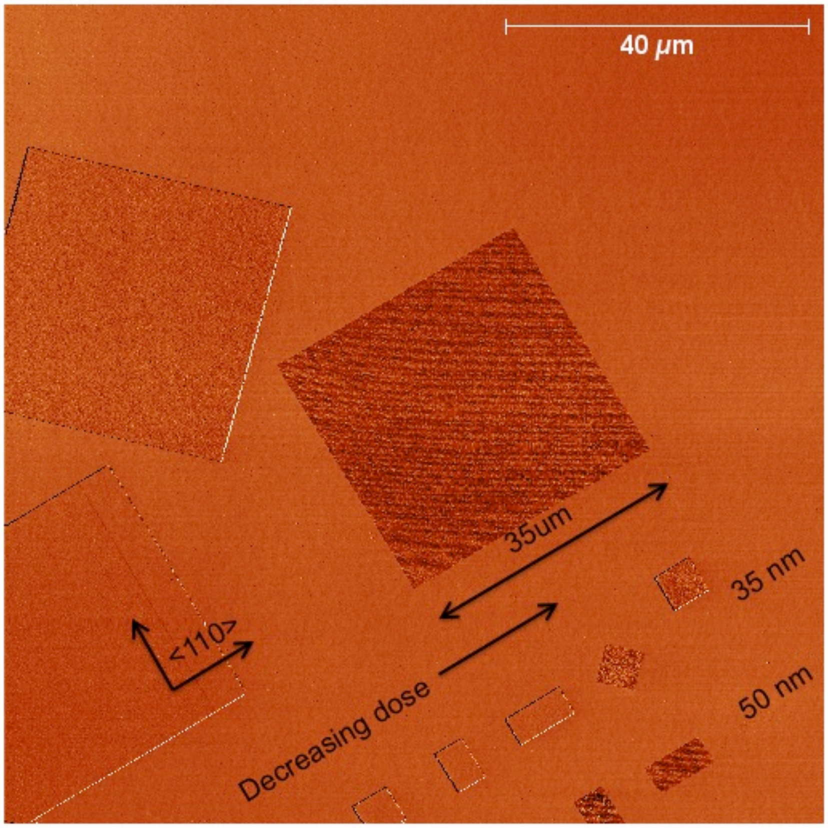

**Figure 2-2: AFM phase image of pattern XLIX. The values 35 nm and 50 nm refer to the pattern pitch used along the respective rows of patterns.**

One critical aspect of patterning with FIB is the focusing condition. Because the focusing of the FIB requires constant exposure of the substrate to ion bombardment, the surface and areas that are exposed to FIB during this process are highly irradiated. To prevent uncontrolled ion damage to the patterned region, the FIB is initially focused on the scribed feature. Once optimal focus is achieved the substrate is offset 1 mm and then the pattern is generated. This allows for the pattern to be generated on a pristine surface. Additionally, it allows us to locate the pattern readily since we know where it is in proximity to the optically visible fiducial. Fig. 2-1 shows the wafer as it is loaded into the FIB from the system's navigation camera (Nav-Cam). Movement to any location is as simple as placing the mouse cursor on the location and clicking.

To achieve optimal focus, the scribed mark is identified and used for focus (typically in excess of 100kX). The ion flux increases as magnification increases, and substrate material and features used for focusing, e.g. scratch marks, are often sputtered away. Within Fig. 2-3 (a), a region is highlighted (in green) where sputtering occurred while focusing at a higher magnification. Previously sharp features of the diamond scribed mark are rounded due to exposure to the FIB beam. After optimal focus is achieved a reference pattern of pits spaced 500 nm on center is generated by exposing each site for a total of 500 ms by 100 repeated passes of 5 ms exposure (Fig. 2-3(b)). The resulting pattern and pits are then imaged with the SEM. The pits are evaluated for circularity, as eliminating astigmatism during focusing is difficult to achieve. The pattern in Fig. 2-3 (b) shows irregularity and asymmetry, i.e. additional focusing is needed, particularly astigmatic correction whereas, in Fig. 2-3 (c) the pits appear circular and symmetric. The top line of the pattern shown in (c) is from the previous pattern for comparison. (Note that the substrate is at a 52 degree angle to the electron beam which

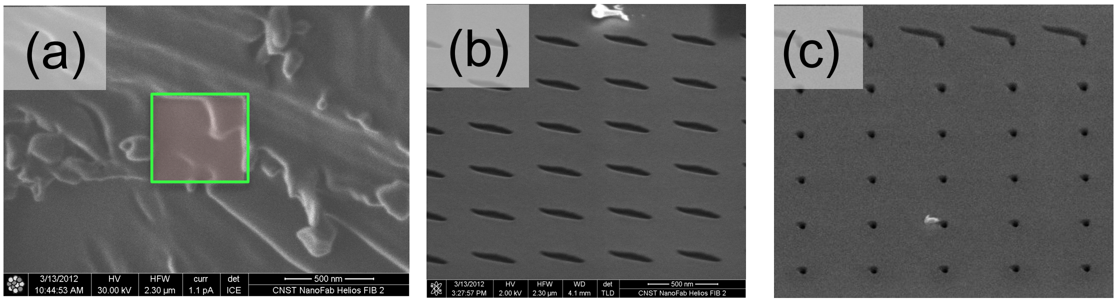

**Figure 2-3: (a) Ion beam focus. The rectangular area in the center (indicated by a green box/tinted red) is the result of focusing at higher magnification where net sputtering of the surface results. Note the rounded edges of what was originally sharp edged due to ion exposure. (b) Test pattern of sputtered pits. Note the highly astigmatic sites. (c) A second test pattern of pits after correction of the first (b). The pits are more circular. The top line of highly asymmetric pits in (c) are from a previously generated pattern shown in (b). Foreshortening in the pattern is due to the electron beam oriented 52 degrees from normal incidence during imaging.**

results in foreshortening of the pit.) Once the focusing condition is achieved, the substrate is offset in the direction opposite the fiducial; it is shown marked "Position 1" in Fig. 2-1.

***All wafers and patterns (unless specifically noted) are aligned with the <110> crystallographic axis of the Si.***

## 2.3 Substrate Cleaning/Etching

In order to ensure high quality, low defect epitaxy it is essential that the substrate is pristine prior to MBE. The Interuniversity Microelectronics Centre (IMEC) and Shiraki cleans that we use are industry standards for Si-epitaxy. [87] The cleaning sequence (see Appendix A) involves the removal of spurious hydrocarbons from the surface (IMEC solution), rinsing in de-ionized (DI) water (R=18MΩ), stripping of surface oxide (buffered oxide etch (BOE) or 5% hydrofluoric (HF) solution), encapsulation of metallic impurities near the surface through oxidation (RCA-2), removal of the encapsulated impurities by repeated oxide stripping, and passivation of the surface with a non-stoichiometric $SiO_x$. The result of this cleaning process is a wafer with a thin oxide layer that can be desorbed in the MBE at temperatures below 800 °C, leaving behind a pristine Si surface ready for epitaxial growth.

While initially the intent was to sputter pits directly into our surface, at the low ion doses we employ, pits are typically not created in the FIB. Subsequently, however, we have observed in our samples that the FIB patterned sites are preferentially etched away during cleaning, leading to pit formation at the patterned sites at ion doses much lower than previously reported. Fig. 2-4 shows the evolution of the surface morphology through the cleaning process. In Fig. 2-4 (a), where the ion dose is high, net sputtering of

Si occurs at the pattern site. It has been shown that additional exposure results in enlarged pits, while at sufficiently low ion doses, patterned sites first manifest as raised bumps. These bumps are attributed to volume expansion of the covalent solid due to ion implantation, defect formation, and oxidation. [88] We speculate that both oxidizing solutions and oxide etching solutions penetrate more efficiently through the (FIB induced) defective sites leading to enhanced etching at the patterned sites. Figure 2-4 (c) shows net removal of Si at the patterned sites.

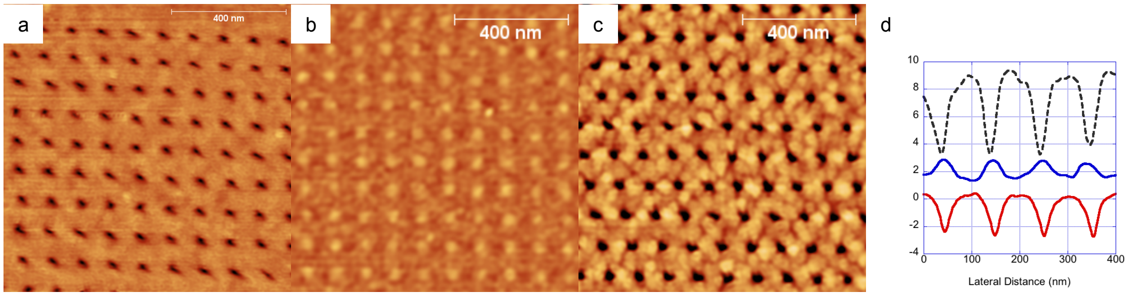

**Figure 2-4: (a) As FIB'ed 69K ions/site; (b) As FIB'ed 7K ions/site; (c) Post clean 7K ions/site; (d) AFM line scans of (a), (b), and (c) offset for clarity.**

Typically, prior to Si deposition, the passive oxide is desorbed within the MBE chamber by heating the substrate to near 800 °C. However, difficulty finding the patterns in early work led us to adopt a low temperature process, in order to eliminate over-annealing and smoothing of the patterns. This low temperature approach involves replacing the formation of the thicker non-stoichiometric oxide with “RCA-2” oxidation, and then stripping that oxide with a dilute 5% HF solution immediately prior to loading in the MBE. This low temperature process, which creates a short-lived hydrogen passivation layer, was based on work by Thompson [86] and Eaglesham [89]. In principle, this process can allow for epitaxy to be achieved at low temperature (>370 °C), provided a prebake at around 200 °C for 1 hour is performed to outgas carbon species. We desorbed the H at temperatures between 500 °C and 580 °C.

## 2.4 Molecular beam epitaxy

MBE is an ultra-high vacuum (UHV) epitaxial growth technique, where source materials are typically evaporated or sublimated by heating. Because of the low pressure, the mean free path (MFP) of the evaporated atoms is much greater than the length scale of the growth chamber. As a result, atoms (or molecules) do not interact, and so travel in a molecular flow regime, undisturbed from source to substrate, i.e. like a beam. This allows for precise control of material growth by shuttering of the material. Crystal growth by this technique is sometimes referred to as thermal deposition, as the source material is thermalized with low thermal energy, i.e. < 1 eV. Relatively high substrate temperatures ($T_s$), between 500 °C – 700 °C, and low deposition rates are required for high quality thin films.

A UHV chamber with a base pressure on the order of $1 \times 10^{-10}$ Torr is required due to the high reactivity of Si. In our chamber this base pressure is achieved by pumping on the chamber with a 600 L/s turbo molecular pump, a SAES non-evaporable getter pump, a titanium sublimation pump, and an ion pump attached to the manipulator. Residual gases can be analyzed with a Stanford Research residual gas analyzer (RGA), while pressures are monitored with a nude ion gage (NIG) and a cold cathode gage. When the chamber is backfilled with gas, the pressure is monitored with a capacitance manometer. Backfilling with Ar requires throttling the turbo pump to prevent overheating; having the non-evaporable getter and the sublimation pump allows for pumping of reactive gases during growth. To maintain the condition of the reaction chamber, samples are transferred through a load lock that typically is pumped down to < $5 \times 10^{-8}$ Torr in under 90 minutes.

The custom built hyper-thermal MBE chamber where our growths were conducted utilizes DC magnetron sputter sources for Si and Ge mounted on 6 inch linear translation stages which allow positioning of the sputter targets between 2 and 12 cm away from the substrate. In DC magnetron sputtering, the chamber is back filled with an inert gas (in this case Ar.) The sputtering targets are biased in order to produce a glow-discharge plasma. Permanent magnets located behind the targets confine the free electrons within a magnetic field, which aids in the efficiency of the sputtering process. As Ar atoms interact with the plasma they are ionized. These ions are then accelerated into the biased target, sputtering target material when the ions have sufficient energy to eject the target material, i.e. greater than the surface binding energy ($E_b$): 4.73 eV for Si and 4.29 eV for Ge. [90]

While one of the primary benefits of MBE is low levels of contamination within an ultra high vacuum reactor; sputtering requires the back filling of the chamber with, in this case, a non-reactive Ar gas to mTorr pressures, which sacrifices a primary benefit of MBE. To minimize the contamination, high purity Ar gas (99.9995% pure) is scrubbed with a hot getter pump, cold getter pump, and liquid nitrogen trap before introduction into the chamber through a fine leak valve to minimize contamination. The getters are designed to reduce contamination to parts per billion. Sputtering has other benefits however, including higher deposition rates, a wider growth parameter space, as well as the ability to deposit high melting point materials without high thermal loading of the substrate.

In sputtering, as Si and Ge atoms are physically dislodged from the substrate, they possess significantly more energy than their thermalized counterparts. The energy distribution of the sputtered atoms is described by the Thompson distribution: [91]

$$\frac{dN(E)}{dE} = \frac{E}{E+E_b} \cos\theta \qquad \textit{Equation 2-2}$$

where *dN(E)/dE* is the number of particles within an energy interval *dE*, *E* is the kinetic energy, $E_b$ is the surface binding energy, and (theta) is emission angle. A normalized distribution is presented in Fig. 2-5. While the maximum in the distribution coincides with $E_b/2$, there is a significant portion of atoms with energies well in excess of $E_b$. Atoms coming in to contact with the substrate, in addition to adsorbing could induce defects, sputter, or amorphize the substrate given sufficient energy.

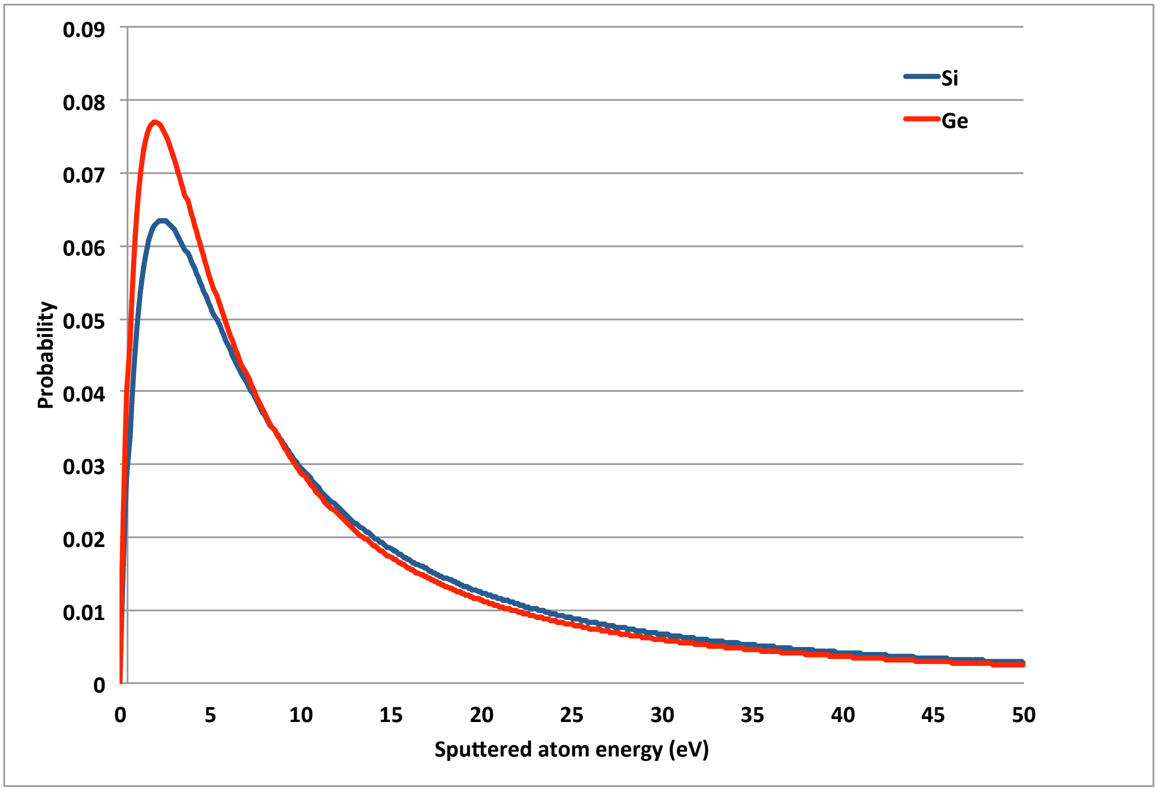

**Figure 2-5: Probability distribution of sputtered atom energy from the target**

However, since sputtering requires backfilling to pressures in the millitorr range (typically 4.8 – 5.0 mT), the actual MFP of the sputtered atoms at these pressures, calculated to be between 0.91 – 0.87 cm, is on the same order as the range of distances between the target and substrate, 2 – 12 cm. As such, the nature of the deposition depends heavily on the translation position of sputter target. In the fully extended position, close to the substrate (2 cm) a large percentage of sputtered atoms can reach the substrate directly, with substantially higher energies. While in the fully retracted position (12 cm), sputtered atoms are not truly in molecular flow, the majority of sputtered atoms will be scattered, and the majority of atoms that do ultimately arrive at the substrate do so after undergoing a random walk due to numerous vapor collisions. The MFP path of the sputtered atoms can be calculated using kinetic gas theory:

$$\lambda_{MFP} = \frac{RT}{\sqrt{2}\pi d^2 N_A P}$$ *Equation 2-3*

where $\lambda_{MFP}$=mean free path, $R$ is the gas constant, $T$ is temperature, d is the diameter of the molecular species, in this case the average of Ar and Si (3.98 Å), and $P$ is the pressure. The mean free path is plotted vs. the chamber pressure in Fig. 2-6. The pressure range corresponding to the experiments are highlighted in red. Additionally, the growth experiments were all conducted with the targets in their fully retracted position.

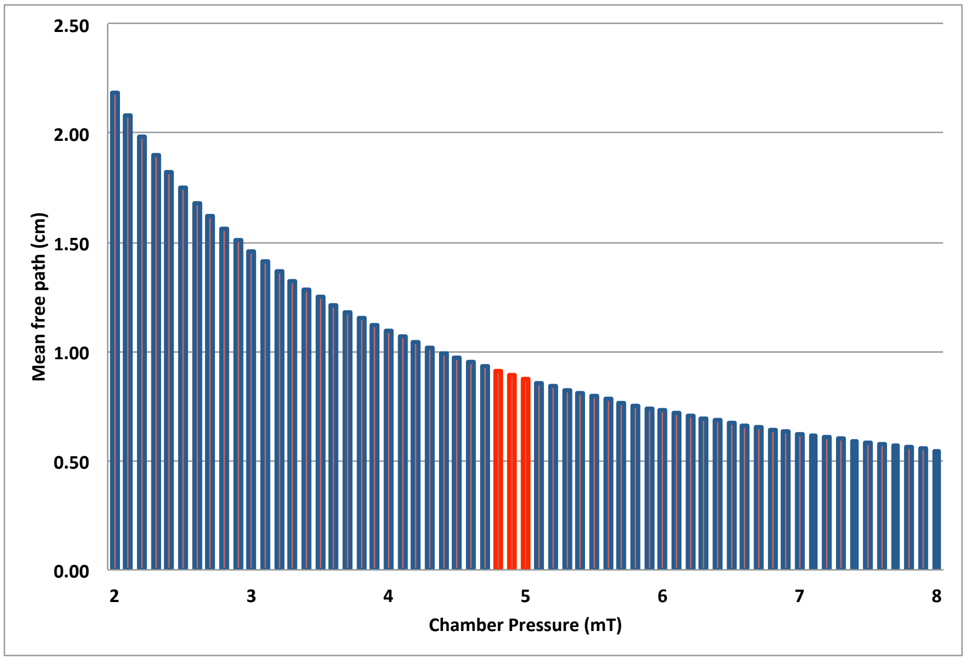

**Figure 2-6: mean free path of sputtered atoms vs. chamber pressure, the red columns indicate the operational chamber pressures for these experiments.**

Growth rates can be adjusted by adjusting the DC power to the sputter guns or alternatively by adjusting the distance between the target and the sample. To determine the deposition rates of Si and Ge, a Maxtek quartz-crystal rate monitor is used to correlate the DC current settings and translational position to deposition rate of each material. The crystal is inserted into the chamber to the position where the substrate is typically located. A quartz crystal has a resonant frequency which inversely proportional to its thickness. As material is deposited on the crystal there is an accompanying shift in frequency as a result of the added mass. The thickness of the deposited material can be calculated by knowing the density of the material being deposited.

The growth surface is monitored during both H desorption and Si and/or Ge deposition by reflection high-energy electron diffraction (RHEED). RHEED is used to probe the surface of the substrate with a high-energy electron beam impinging the substrate at a glancing angle. The low angle limits the electron beam interaction with the

2D surface lattice of the substrate. Alignment of the substrate is critical to achieve the appropriate diffraction condition. For Si (001), the electron beam is typically aligned to the [110] azimuth. Diffraction occurs where the Ewald sphere intersects with the reciprocal lattice rods.

The configuration in our chamber is illustrated in Fig. 2-7. Key features include: a differentially pumped electron gun; magnetic shielding; and a back-mirrored phosphor screen. The electron gun is differentially pumped to keep the tungsten filament within a high vacuum while the chamber is back filled into the millitorr range. The magnetic shielding is needed because the magnetron sputter guns produce stray magnetic fields which interfere with the alignment and focusing of the electron beam. Finally, while it is typical to place a CCD camera behind the phosphor screen to monitor the diffraction pattern, the configuration of the chamber has the load lock placed opposite of the electron gun. This precludes the placing of a CCD camera on the backside of the phosphor screen to monitor it. So instead, our phosphor screens are mirrored on the backside, which allows monitoring from the front.

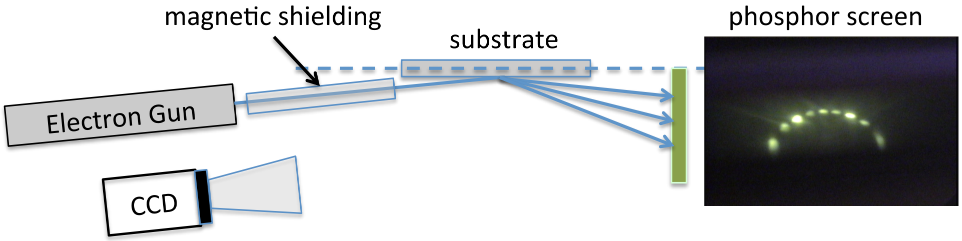

**Figure 2-7: RHEED schematic. The phosphor screen shows the (2x1) surface reconstruction of Si (001) along the <110> direction of a Si buffer.**

As mentioned previously, the Si surface is monitored during the various process steps of the growth; shown in Fig. 2-8. Figure 2-8 (a) shows the first order Laue circle of a hydrogen terminated substrate as the result of dipping in HF or BOE to strip the surface oxides and passivate the Si. The peaks are the result of diffraction from the surface. Figure 2-8 (b) shows a typical (2x1) reconstructed Si (001) surface. The (2x1) diffraction peaks, at half order positions, appear when of the surface is rid of any passivation or contamination, and when there is sufficient diffusion to promote the formation of Si dimers. This is an ideal surface on which to grow. The final figure, 2-8 (c), is indicative of a rough 3D surface. The pattern is the result of bulk-like diffraction *through* the Ge QDs formed on the surface. By monitoring these steps during the process we are assured of different surface conditions.

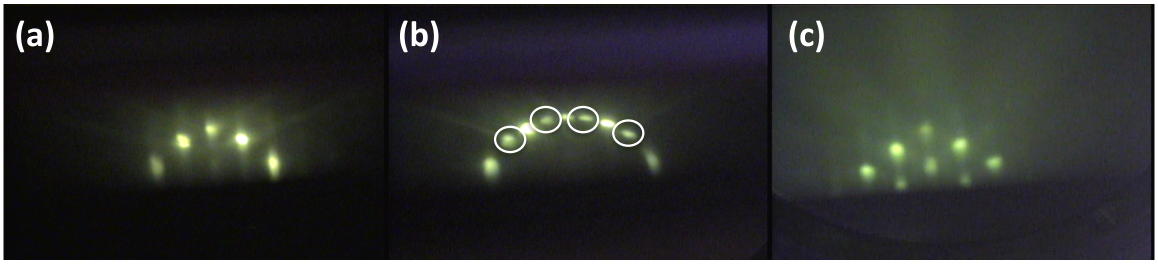

**Figure 2-8: RHEED patterns of Si (001) along the <110> azimuth. (a): pattern of a substrate stripped with HF prior to heating showing bulk diffraction spots. (b): (2x1) reconstructed Si surface after desorption of passivation. The (2x1) diffraction peaks are circled and appear in between the bulk diffraction peaks. (c): The pattern after 6 ML of Ge is deposited, showing diffraction through 3D QDs.**

It should be noted that RHEED monitors a macroscopic, random location on the substrate, since the beam diameter is of order 1 mm >> size of the patterned regions. The electron beam is typically operated at 30kV and 1.6 A.

## 2.5 AFM

AFM is an integral component to our analysis of the pattern and QD arrays. It was originally developed by Binnig, Quate and Gerber [92] who recognized that the interaction forces between a sharp stylus mounted on a cantilever and a surface can be measured by monitoring the deflection of the cantilever. There are a number of advantages of this technique compared to for example, scanning tunneling microscopy (STM), including the ability to characterize non-conductive surfaces, measure interaction forces with pN resolution, and measure samples in ambient or even wet environments. While Binnig et al. originally used an STM probe to monitor the deflection of the cantilever, more recent systems utilize a laser beam reflected off the back of the cantilever which is aligned onto a quad array detector. As the cantilever is deflected by interaction with the surface, the magnitude of the deflection is measured by the displacement of the laser on the quad array detector. (see Fig. 2-9). Rastering the scan across a surface allows for 3D mapping of surface heights.

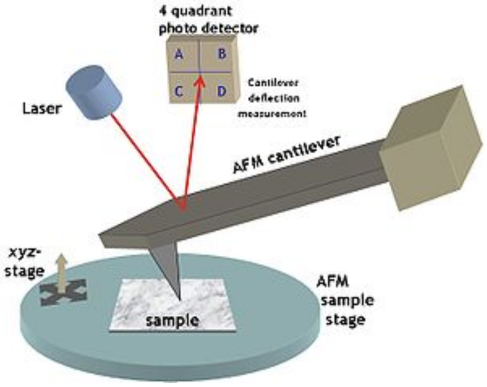

**Figure 2-9: Layout of a typical atomic force microscope (AFM)** [93]

Starting from an equilibrium position, the cantilever deflects as it nears the surface due to attractive van der Waals forces. As the cantilever is a spring, the magnitude of the force can be calculated using Hooke's law:

$$F=-kx \qquad \text{Equation 2-4}$$

where *F* is force, *k* is the spring constant of the cantilever, and *x* is the deflection of the cantilever. The deflection is determined by monitoring the displacement of the laser beam on the quad detector. There is a characteristic force vs. displacement curve for the approach and retraction of the tip relative to the surface shown in Fig. 2-10, where displacement is the stage displacement in the z-direction. The tip is initially aligned on the photodetector in the equilibrium condition (A). When the tip get close enough to the surface, attractive van der Waals forces pull the tip into the surface (B). Pushing the tip harder into the surface results in a deflection of the cantilever in the opposite direction (C). The resulting slope is a measure of the local elasticity. During retraction the tip will stick to the surface longer due to capillarity and adhesion forces resulting in a hysteresis loop.

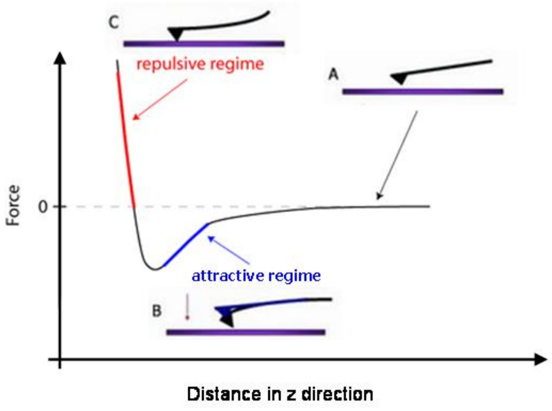

**Figure 2-10: Force vs displacement curve for AFM** [94]

The AFM can be operated in a variety of modes which are distinguished firstly by the nature of the tip/surface interaction, i.e. contact vs. non-contact. In contact mode, the tip is brought into contact with the surface until a predetermined set point is met. As the tip tracks across the surface the scanner adjusts and records the z-height needed to maintain the setpoint. The scan is created by recording the z-height at each x,y, coordinate. Due to the forces involved, there is potential for damage to either the tip or sample.

Non-contact mode is typically used when the sample is softer or easily damaged. In non-contact mode the tip is operated in AC mode, i.e. the tip is oscillated near its resonant frequency. The resonant frequency is determined by sweeping the drive frequency while monitoring the deflection of the tip. A well-aligned tip has a maximum deflection at the resonant frequency. The magnitude of the deflection tails off as the difference between the drive and resonant frequencies increases. The tip is brought close enough to the surface so that van der Waals forces are strong enough to attract the tip without actually pulling the tip onto the surface during oscillation. The force increases the magnitude of the oscillation, effectively changing the resonant frequency of the tip. As a consequence, the magnitude of the oscillation will change with the distance between the tip and the surface. In practice, the drive frequency is shifted off the resonant frequency, the tip is brought close to the surface and a set oscillation magnitude is maintained by adjusting and recording the z-height at each x, y location.

A third technique, intermittent or tapping mode is a hybrid of these techniques. In tapping mode the tip is oscillated at its resonant frequency, but then is brought close enough to the surface so that the bottom of the oscillation comes into contact with the surface. As the tip gets closer to the surface the oscillation of the cantilever is increasingly damped. The scanner adjusts the z height in order to maintain the oscillation magnitude, i.e. constant damping. The sample is scanned and the z height is recorded.

This method is preferred in ambient conditions as it is less susceptible to adsorbed water on the tip and surface.

While in tapping mode, it is possible, while collecting topographic information, to monitor the phase of the tip oscillation in relation to the drive signal. Additional material properties, e.g. changes in composition, adhesion, and friction can be delineated due to changes in the response of the tip as it comes in contact with the surface. Phase modulation is also good for highlighting changes in surface topography. Features that are almost indiscernible in height mode are clearly delineated in phase mode. In Fig. 2-11, a region is scanned in (a) height mode and (b) phase mode. While there is nothing visible in the height scan, the phase mode clearly shows the presence of a pattern. Even after flattening and filtering the height scan, the features are still difficult to see (c).

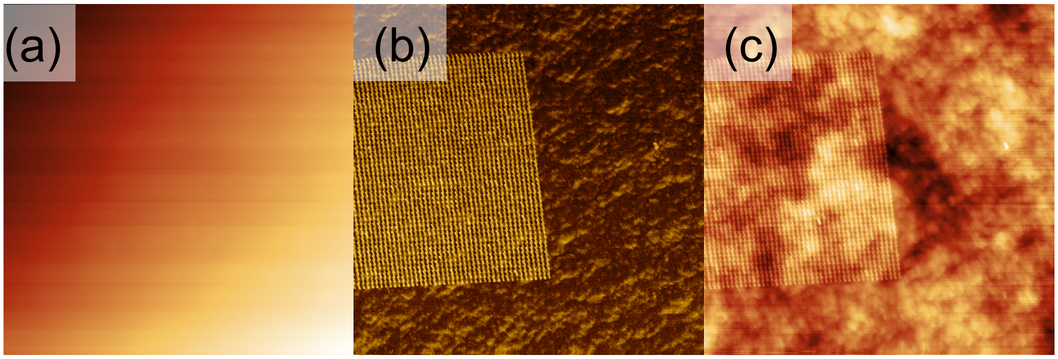

**Figure 2-11: (a) an unprocessed AFM micrograph in height mode. The same scan produces the image in (b) in phase mode. (c) the height scan post processing.**

The AFM in this study was performed exclusively with an NDT-Solver Pro AFM. It comes equipped with two distinct scan heads: universal, and SMENA. The universal head comes with interchangeable tip holders, which allows for a variety of scan techniques, e.g. magnetic force microscopy, scanning tunneling microscopy, etc. The universal head holds the tip in position while the sample is moved underneath, i.e. scan by sample. The range is limited to 13 μm x 13 μm. Alternatively, the SMENA head scans the tip across the surface: i.e. scan by probe. It has the advantage of a much greater operational range of 110 μm x 110 μm, which has proven useful in this research, firstly because of the difficulty of locating the patterns, and second because the dimensions of the pattern array are on the order of 100 μm x 100 μm. This allows for almost complete measurement of the array without resituating the tip. The SMENA configuration also allows for easy visual access to the substrate, greatly facilitating alignment of the tip to the pattern.

Two different tips were used NT-MDT NSG01 and NSG10. SEM images of typical cantilevers are shown in Fig. 2-12. The side view is shown. While the tip appears tetrahedral, the last 500 nm, i.e. the portion of the tip that interacts with the surface, is roughly cylindrical with a taper of 7-10 degrees. For perspective, the thickness of the cantilever is 2 microns. The tip radius is specified as 10 nm maximum, 6 nm typical. The NSG01 and NSG10 are similar, except for the cantilever length, resulting in spring constants of 5.5 N/m and 12 N/m, and resonant frequencies of 150 kHz and 240 kHz respectively. While the stiffer cantilever is less impacted by adsorbed moisture on the surface, the relative lifetime of the tip is shorter. More recently available tips, HA_NC "Etalons", which have very similar stiffness and resonant frequencies to the NSG01 and NSG10, have been used. The HA_NC "Etalon" tips have much tighter mechanical tolerances, as well as lower unit cost.

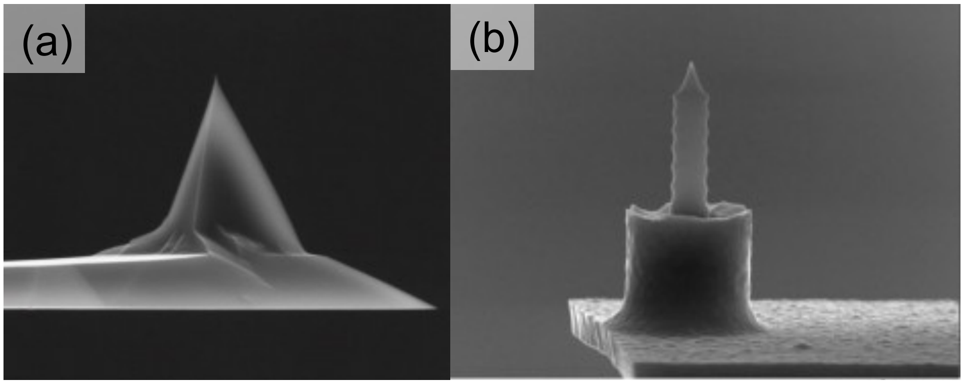

**Figure 2-12: AFM probes (a) NSG01 AFM probe. (b) HA_NC "Etalon" probe.**

While AFMs are very effective at high resolution surface characterization there are some limitations, particularly when the length scale of the lateral features is on the same order as that of the tip. This is referred to as tip convolution, which leads to under-measurement of negative or recessed features, and over-measurement of positive or raised features. Examples of tip convolution are illustrated in Fig. 2-13. In region A the undercut feature is completely undetected by the tip. As the tip scans through the pit in region B, the sharp undercut feature appears as a rounded edge because the tip is in contact with the surface on the side of the tip, not at the bottom. As the tip moves further into the pit the contact point moves further up the sidewall. When the tip finally comes in contact with the bottom surface, the bottom flat is under-measured because the tip sidewall again comes in contact with the opposite edge of the pit. This time the contact starts high on the sidewall of the tip and moves towards the bottom of the tip. Again, a sharp edge will reveal the tip curvature and will show as a rounded edge. Under-measurement will occur in very small or high aspect ratio areas where the tip cannot get down into the sample to accurately measure the depth as shown in region C. Over-measurement will occur for small positive features as shown in region D. As the tip is stepped across the feature, the feature probes the tip, revealing the shape of the tip not the shape of the feature. Features smaller than the tip, in essence, measure the tip. These over and under measurement errors can be minimized by careful tip selection. I.e. selecting tips with radii smaller than the features that are being measured, and selecting high aspect ratio tips to measure steep features.

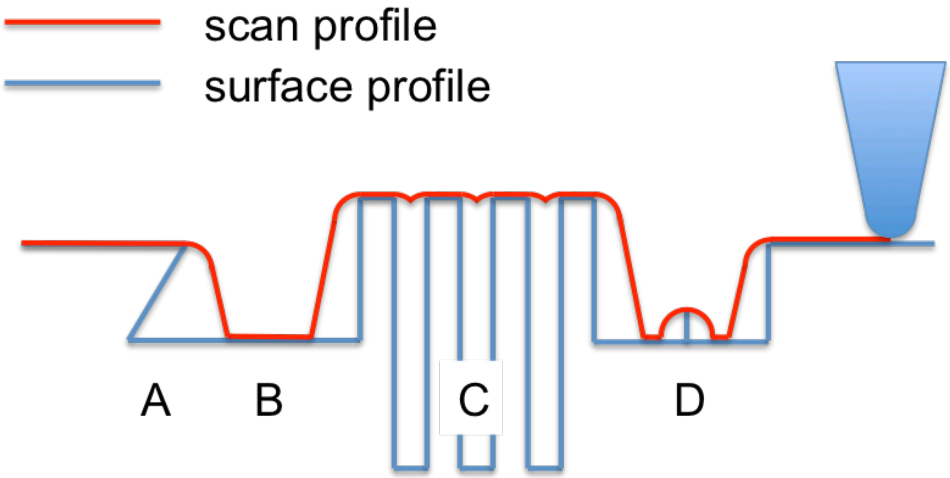

**Figure 2-13: AFM tip measurement errors.**

Tip artifacts can result from damaged tips. Features of the damaged tip may repeatedly appear in the scan (Fig. 2-14). To determine whether the features are real, or an artifact of the tip, the sample needs to be rotated and rescanned. If the features appear in the original orientation it is typically the result of a damaged tip. Contamination of the tip, where debris adheres to the tip, may result in a similar error.

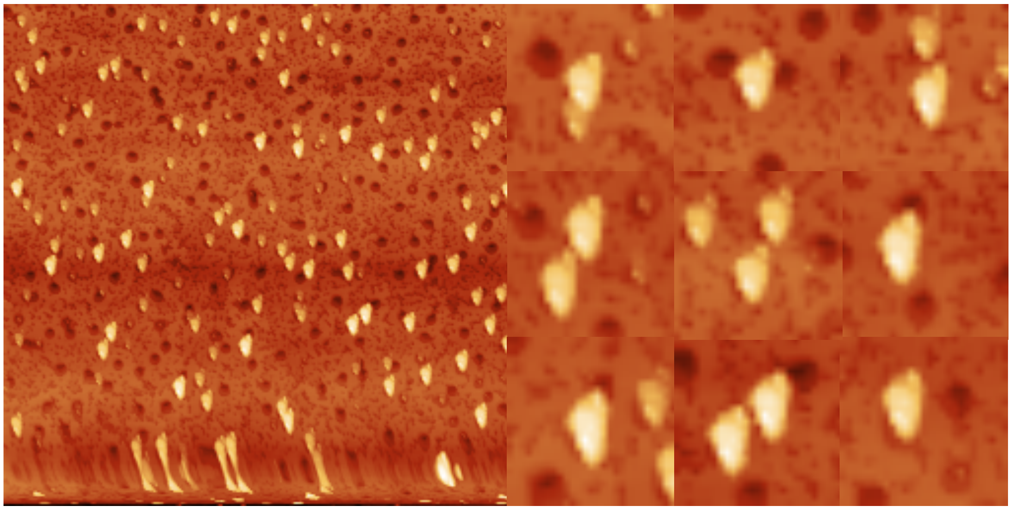

**Figure 2-14: AFM tip artifact. The presence of a repeated highly unique feature is an indication that there may be a tip artifact. Sample surface on the left. On the right are 9 different examples from the pattern where this feature repeats itself.**

Finally, post processing of the raw data is required to discern small surface features. Piezo ceramic tubes are commonly used to manipulate the tip or substrate, and while they are very efficient at small nanoscale motions, they have two distinct deficiencies which need to be accounted for: hysteresis in the piezo ceramics, and the coupled XZ and YZ motions.

Hysteresis in piezo ceramics is common, and it can impact the measurement of a surface. When moving from one scanned region of the sample to another, it is possible to see the effects of ongoing drift in the resulting scan. The distortion due to drift can be minimized by waiting a few minutes before beginning a scan. In practice, a line scan can be repeated until the scan is repeatable, i.e. little to no drift is apparent.

The motion of the tip or the sample is typically actuated with the use of a single piezo ceramic tube. To create the motion various voltages are applied to the specific leads on the tube. Expansions and contractions within the tube create the XY translations and control the z height of the tip with respect to the sample. The resulting trace of the tip is not perfectly flat, but a parabolic arc. The magnitude and scale of the features on the surface, e.g. step edges, are often much smaller than the vertical displacements actually measured. In order to see the detailed structure of the surface, third or fourth order parabolic fits may be subtracted from the raw data to flatten the linescans and reveal the detailed topography (Fig. 2-15 (a)).

In addition to removal of the polynomial background (Fig. 2-15 (b)), other processing steps that are implemented to facilitate characterization of the surface include: correcting scan line offsets (Fig. 2-15 (c)); band pass filtering using the fast Fourier transformation (Fig. 2-15 (d)); and median filtering (Fig. 2-15 (e)). Fig. 2-15 (f) is the result of using a watershedding algorithm to identify local maxima (i.e. QDs) in the surface.

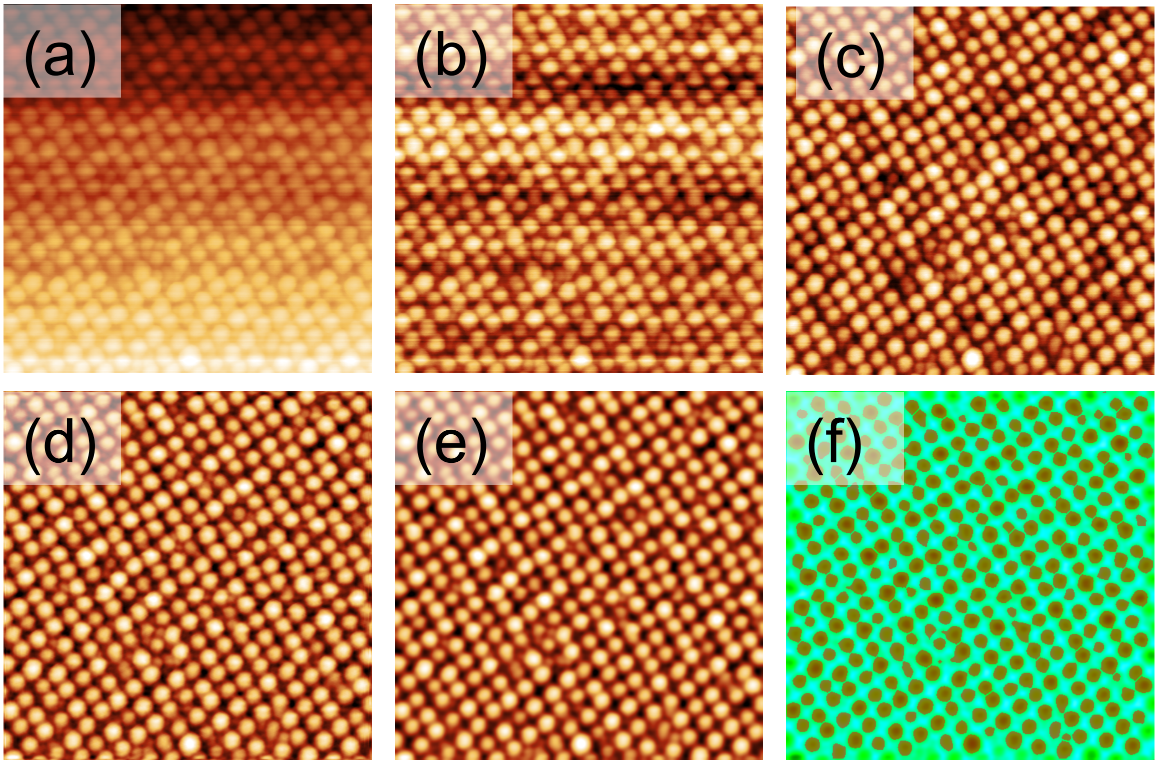

**Figure 2-15: An (a) unprocessed AFM height scan, (b) after a removal of a polynomial background, (c) after line scan height offset correction, (d) after band-pass filtering using**

**the fast Fourier transformation, (e) after a 5 point median filter, and (f) local maxima identification.**

## 2.6 Transmission Electron Microscopy (TEM)

Transmission electron microscopy (TEM) is an invaluable tool for the material scientist. The material sample is thinned until it is electronically transparent (typically less than 100 nm), and a high energy beam of electrons is used to image the sample. We used two microscopes for these studies: an FEI-Titan with a tungsten field emission filament operated at 300keV, energy filtered TEM (EFTEM) capability and a high angle annular dark field (HAADF) detector; and a JEOL 2000FX with a $LaB_6$ filament operated at 200keV. Each was equipped with a double angle tilt sample holder.

TEM has been a vital part of our investigation, primarily to corroborate our conclusions drawn from our AFM studies. We have used bright field, (BF) condensed beam electron diffraction (CBED), and high angle annular dark field (HAADF) to corroborate our AFM studies, to learn about the underlying microstructure of our patterns and to verify the existence and configuration of QDs.

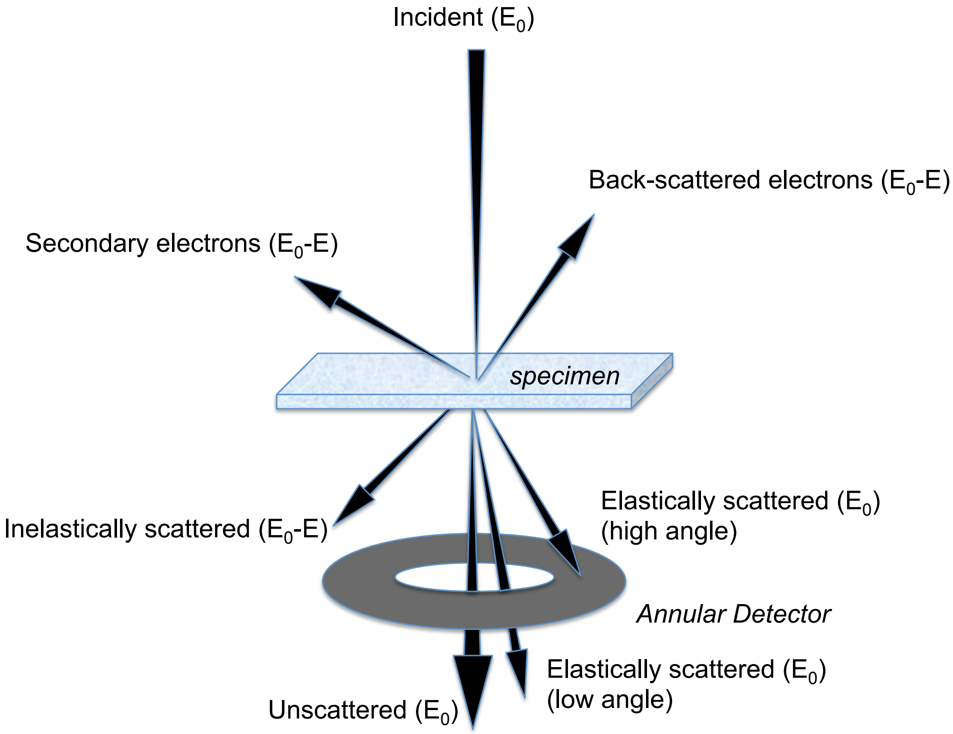

**Figure 2-16: Electron-sample interaction.**

A diagram of electron-sample interactions is provided in Fig. 2-16. The basic principle of TEM is that electrons will interact with a sample and transmit through, provided that the sample is thin enough. Careful interpretation of transmitted electrons can provide insight into μ-structure, crystal structure, the presence and nature of defects, as well as chemical composition and configuration. The various modes, or techniques take advantage of the different transmitted electrons.

Conventional TEM images are created by Bragg scattering of electrons, which in crystalline materials will diffract and interfere constructively when the Bragg condition is met. The Bragg condition:

$$n\lambda = 2d\sin\theta \qquad \text{Equation 2-5}$$

where $n$ is an integer, $\lambda$ is the wavelength of the electron beam, $d$ is the distance between two parallel planes, and $\theta$ is the angle of the incident beam relative to the normal of the plane. The resulting image in the back focal plane is the diffraction pattern of the crystal(s) which contains critical information about the crystal structure. Contrast will occur due to attenuation of the electron beam, e.g. sample thickness, or changes in the diffraction condition which can be caused by e.g. strain or defects.

Another imaging TEM based imaging process is high-angle annular dark field (HAADF), otherwise known as z-contrast imaging, incorporates scanning transmission electron microscopy, in the generation of images. A condensed beam, or probe, is rastered across the surface, and the scattered electrons are collected in an annular detector. Atoms with a larger Z have a larger scatter angle, and will scatter more electrons onto the detector, thus making higher Z atoms appear brighter in the image. Thus Ge appears brighter than Si because of its larger Z. Images in figure 2-17 are the QD stacks imaged in both conventional bright field, and HAADF-STEM modes.

Some electrons experience energy loss in the course of transmission. Inelastically scattered electrons are produced by core interactions with the sample, and because they pass through the optical system, they can be used to make images. Energy-Filtered TEM (EFTEM) takes advantage of this phenomenon by utilizing an energy slit to capture a narrow band of energies at one time. Since the energy of the scattered electrons is chemically dependent, chemical analysis can be achieved by acquiring a series of energy filtered images without the time intensive requirements of EELS or EDS.

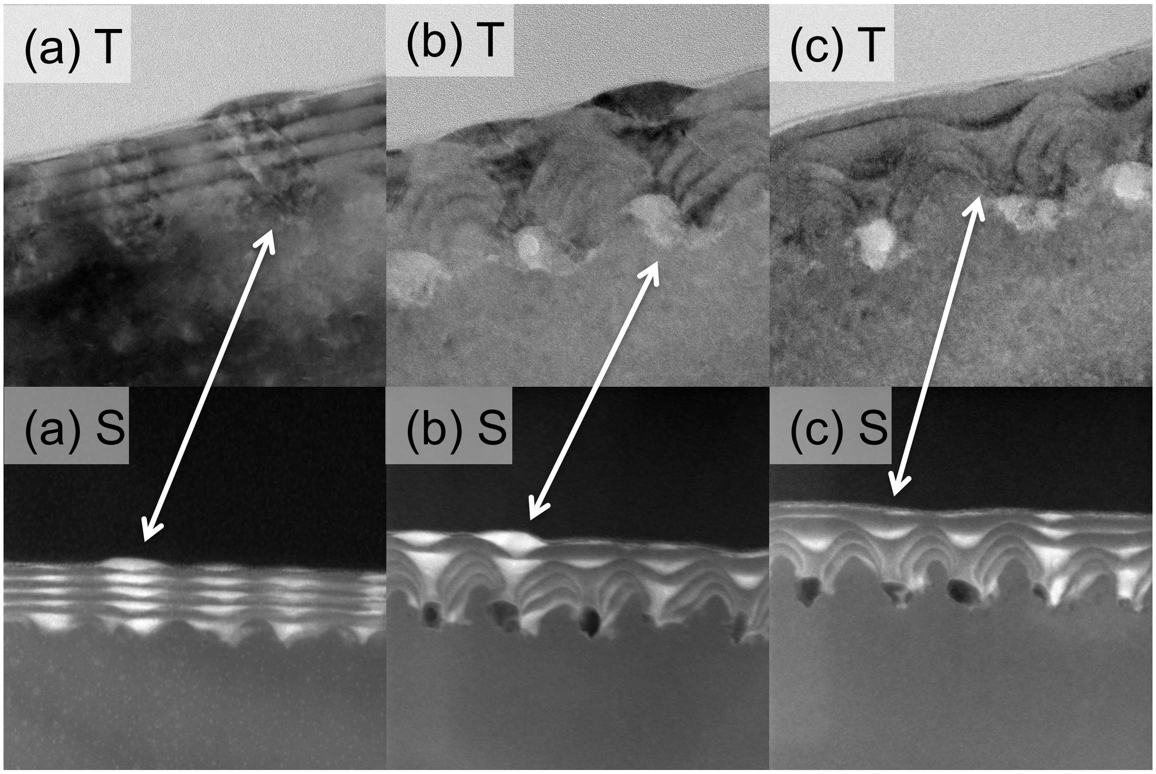

**Figure 2-17: TEM micrographs of a 5-layer QD crystal in both bright field and HAADF modes. Arrows indicate corresponding QDs.**

## 2.7 TEM sample preparation

Due to size considerations of our patterns, i.e. typically < 10 um, TEM sample preparation requires the use of FIB assisted sample liftout and polishing. The process is done in a Dual Beam FIB similar to the one used for our patterning. The area from where we need the sample is identified with use of the SEM. First a protective electron beam induced deposition (EBID) carbon layer is deposited followed by an EBID platinum coating. (Fig. 2-18 (a)) This protects the sample from damage during the liftout process. Steps are then machined, i.e. sputtered with FIB, into the substrate to expose a slice of Si about 1 μm thick, which is attached to a needle at the Pt surface. (Fig. 2-18 (b)) The sample is cut out with FIB, polished with progressively lower FIB energies and higher glancing angles, and attached to a grid. The result is an electronically transparent section (Fig. 2-18 (c)).

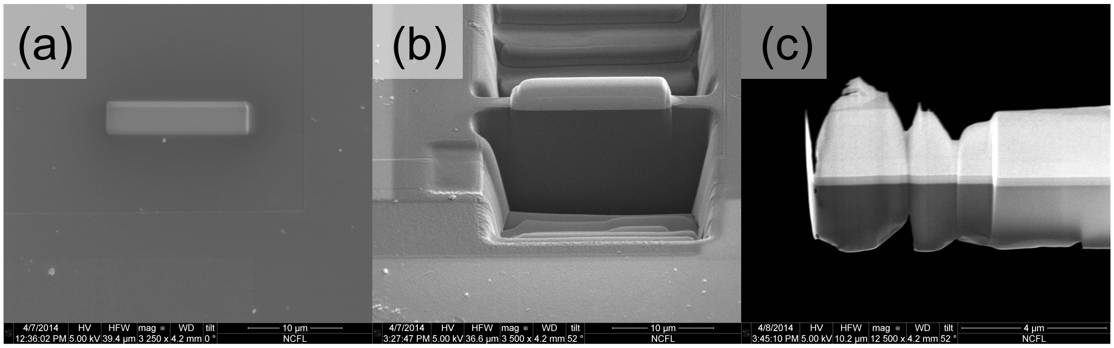

**Figure 2-18: SEM images of (a) a deposited protective layer of platinum. (b) sequentially machined steps into the Si substrate expose a sample for liftout. (c) An electronically transparent polished sample.**

FIB liftout was performed at Virginia Polytechnic Inststitute by James Tuggle, and at Penn State University by Joshua Maier.

## 2.8 Scanning electron microscopy (SEM)

Instead of using transmitted electrons for image generation, a scanning electron microscope scans the electron beam across a sample, which generates both secondary and back-scattered electrons. A detector, typically an Everhart-Thornley detector, collects a sampling of the electrons, and the image is created by mapping the detector intensity with the beam position. Secondary electrons (< 50 eV) are created by inelastic interactions of the high energy electron beam and the valence electrons of the sample. Each incident electron may produce multiple secondary electrons. Secondary electrons are particularly good for topographical information for two reasons: first, only the secondary electrons produced near the surface escape the sample because of the low energy, and second, the secondary electron yield is highly dependent on the incident angle of the electron beam on the surface, with the yield decreasing with increasing glancing angle.

The SEM has proven a very useful tool to examine our patterns in a quick and efficient manner as illustrated in Fig. 2-19. It is used routinely to qualitatively assess our focusing condition during patterning (a), it can provide a clear precise overview of a sample (b), it can provide both qualitative and quantitative information regarding the quality of a QD growth (c) and (d).

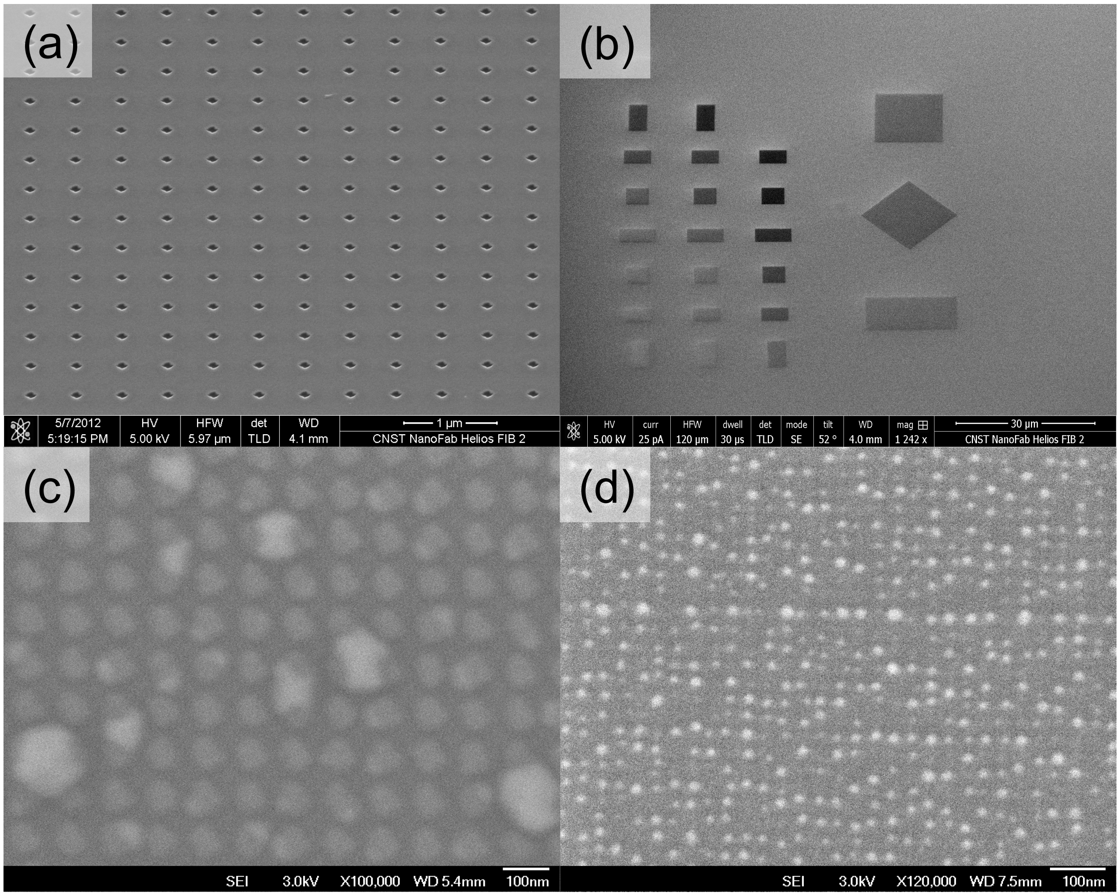

**Figure 2-19: SEM images of (a) fiducial pattern, (b) patterned array, (c) huts and domes on 100 nm pitch patterned surface, (d) QDs grown on 35 nm pitch pattern.**

# 3 Early Process Development

*"We have a habit in writing articles published in scientific journals to make the work as finished as possible, to cover up all the tracks, to not worry about the blind alleys or describe how you had the wrong idea first, and so on. So there isn't any place to publish, in a dignified manner, what you actually did in order to get to do the work." –Richard Feynman, Nobel Lecture 1966*

The initial goal of this project was to grow quantum dot meso-crystals (QDMCs), where the "lattice parameters" of the QD array could be controlled by directing a seed layer of QDs, and then extending the crystal in the third dimension using the strain field in a Si layer to direct the ordering of Ge in subsequent layers. QDMCs of this description have been fabricated using EUV lithography. [7,19,74] Our first step was to develop a process using focused ion beam patterning to control the initial QD layer, [22,24,25,80,83] and then develop the necessary growth protocols to extend the QDMC in the third dimension. Specific challenges include: directing nucleation at reduced length scales, i.e. below 100 nm, re-planarizing each QD layer with a Si cap or "interlayer", and reproducing the seed layer positioning in the subsequent layer. An advantage of patterning with FIB is the ability to serially write unique patterns without the need for masks. While we have grown some QDMCs, our primary focus has been on understanding the results of our 2D seed growths at these reduced length scales.

## 3.1 Early process development

Using the aforementioned studies as a starting point, a method was developed to create highly ordered QD patterns to use as a foundation for crystal growth. As mentioned in chapter 2, we started with the assumption that it was necessary to sputter sufficient material to create a pit in the substrate surface during patterning. We examined a range of doses between 700 ions/site – 69,000 ions/site by first generating individual patterns of various doses with pitches of 100 nm, and AFM confirms that at the highest doses, pits are created in the surface as-irradiated (previously shown in Fig. 2-4, reshown in Fig. 3-1), but even at doses as high as 21K ions/site, amorphization results in raised features, although the subsequent cleaning results in well formed pits that we use as a template for our patterning process (Fig. 3-1). As an aside, efforts to expose a patterned sample and then observe the raised features in the SEM were unsuccessful due to a lack of material contrast and feature height.

A series of patterns of decreasing dose are shown in Fig. 3-1, highlighting some observable trends and common features. The SEM micrographs in the first column were scanned just after patterning, as it is important to confirm that the focus condition is adequate. Close inspection of the arrays (Fig. 3-2) reveals some ellipticity in some of the patterns, an indication that the focus wasn't particularly good to begin with. Creating and examining a fiducial pattern at the outset to assure a well focused beam became standard practice. The micrographs also reveal a trend from lower right to upper left of increasing ellipticity and size. The final pattern (Fig. 3-2 (c)) is an array generated with an interdot pitch distance of 30 nm to highlight the FIB's capability to form extremely dense pattern arrays, and the integrated SEM's ability to image at such small lengthscales.

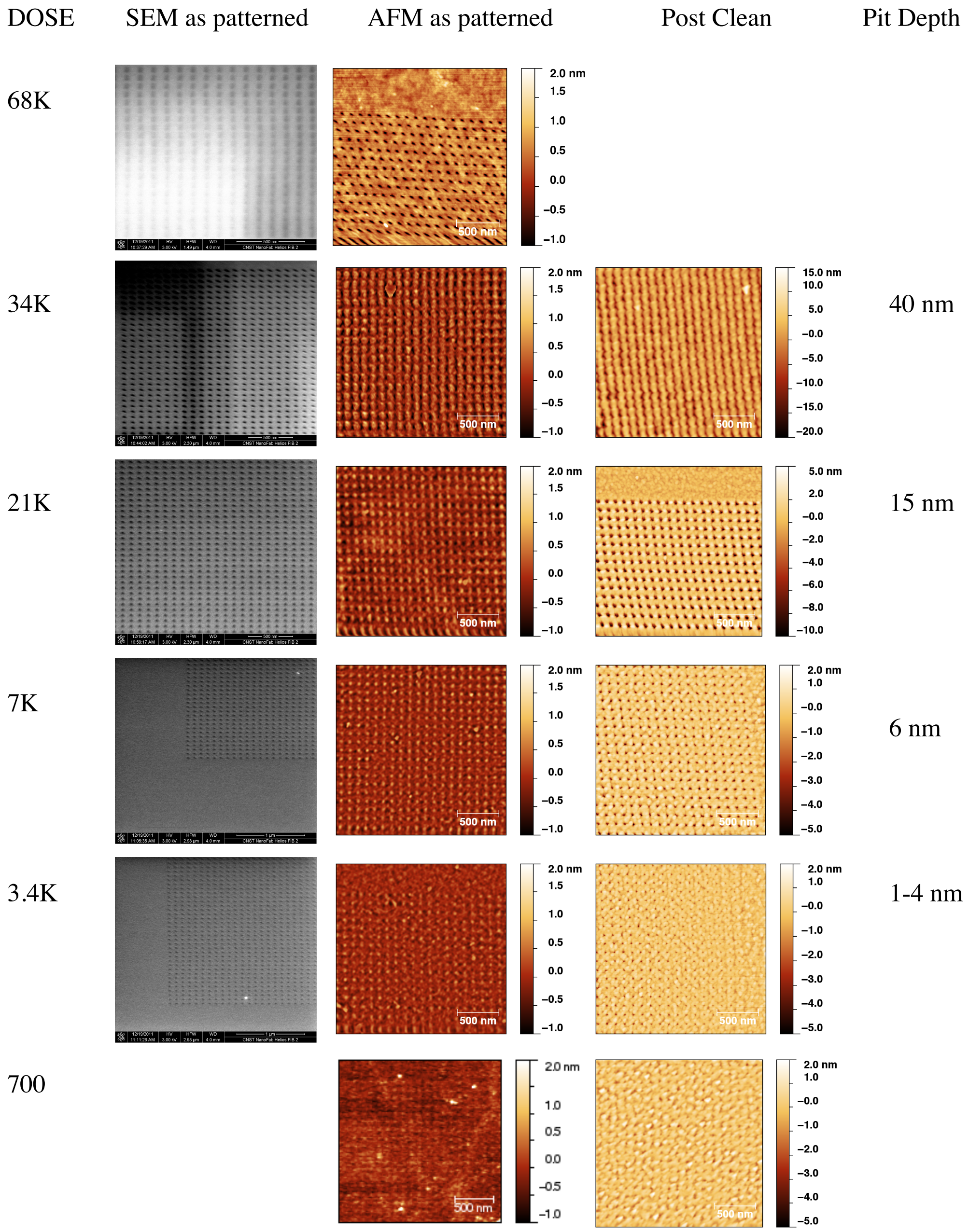

**Figure 3-1: Patterns of varying dose as they appear (1) in SEM mode just after patterning, (2) AFM as patterned, and (3) AFM of patterns after a standard IMEC-Shiraki clean with the passivation oxide stripped with BOE.**

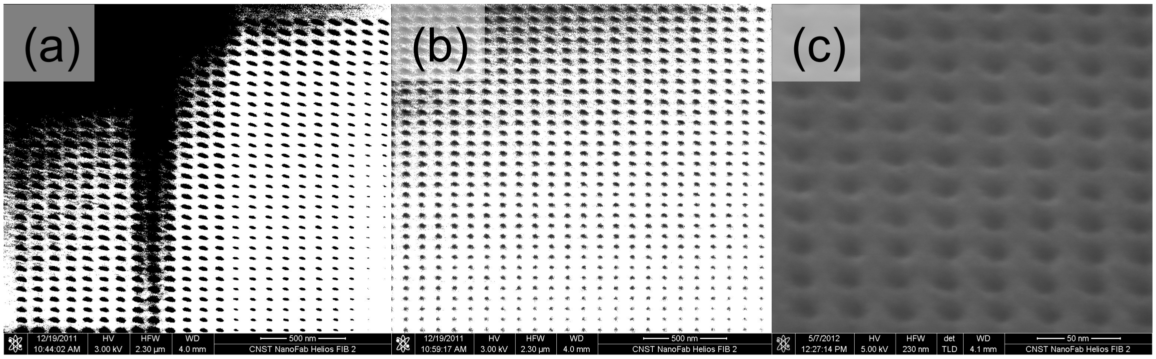

**Figure 3-2: Filtered SEM micrographs highlighting the ellipticity in both (a) 34K ions/site, and (b) 7K ions/site patterns. There is a general trend of increasing size and ellipticity moving across the patterns from bottom right to upper left. (c) pattern at 30 nm pitch.**

## 3.2 First growths: loss of pattern at high temperature

As described in chapter 2, one of the requirements of the cleaning process is to passivate the Si wafer prior to entry into the growth chamber. This is done to ensure that the surface is isolated from the atmosphere prior to growth. Whatever atmospheric contamination occurs will be removed during an outgassing of the wafer during the growth process. The IMEC-Shiraki cleaning process that we use for our standard quantum dot growths leaves the surface with a sub-stoichiometric $SiO_x$, where x is less than 2. This is removed by ramping the temperature to between 780 °C and 800 °C, where the surface oxide desorbs. This is monitored using RHEED. When a clear 2x1 surface reconstruction is apparent, typically taking 10-12 minutes, the wafer is cooled to the growth temperature of the experiment, typically 450 °C. A number of these early samples are exhibited in Figure 3-3.

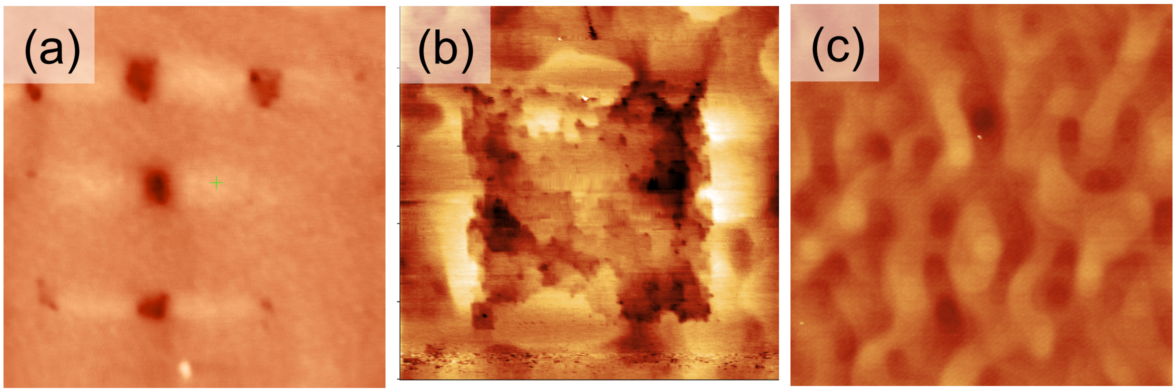

**Figure 3-3: AFM micrographs of (a) 2x2 µm scan of a fiducial pattern (700K ions/site) after high temperature desorb showing loss of pattern features. (b) 8x8 µm scan of a high dose pattern showing loss of pattern features and Si step edges within the patterned region. (c) 15x15 µm scan showing complete loss of a low dose pattern after high temperature desorb.**

It is clear that recrystallization and substantial Si diffusion occurs during the desorption process as evidenced by the loss of the large pit features in the fiducial pattern (a) and the presence of step edges elsewhere (b) and (c), thus eliminating pattern features and preferred QD nucleation sites. While temperature increases surface diffusion, the surface oxide enhances the surface mass transfer of Si even more. [95] Surface Si reacts with the oxide to form SiO which volatizes. This occurs around the edges of voids in the surface oxide. The process works as follows:

$$Si + SiO_2 \rightarrow 2SiO \qquad \textit{Equation 3-1}$$

When the oxide is gone, the enhanced transport ends.

An alternative, lower temperature method for removal of the oxide and passivation was identified, which involves the stripping of the oxide in hydrofluoric acid (HF), and then desorbing the hydrogen (H) terminated surface at or above 550 °C. [86,96] Eaglesham demonstrated that Si epitaxy was possible at temperatures as low as 370 °C, even without desorption of the hydrogen on the surface. We incorporated a 30 second, 5% HF solution dip prior to loading of the wafer into the MBE chamber in order to avoid the high temperatures required for removing an oxide. While we have not verified this, it is conceivable that removing the oxide prior to insertion into the chamber would have prevented the loss of patterns, even at the elevated temperature. Grydlik et al. [20] have found this step to be vital in the preparation of their samples to prevent loss of patterning during an extended high temperature (700 °C) outgassing.

## 3.3 QD growth on low temperature desorbed surfaces

Removing the oxide with 5% HF solution prior to introduction into the MBE reduces the desorption temperature by needing only to volatize H rather than $SiO_x$. With this modified process, the post-desorbed surfaces retain pattern features at lengthscales below 100 nm. Our first successful QD growths were completed with the help of the Reinke group, utilizing the growth chamber of their scanning tunneling microscope (STM). Samples were cleaned, stripped of any oxides, and then mounted to a substrate holder using tantalum strips, which were spot welded in place. The samples were outgassed overnight, the hydrogen was desorbed at 550 °C for five minutes, and finally, 5.7 ML (8Å) of thermally evaporated Ge was deposited at a rate of 0.1ML/min at 420 °C. AFM micrographs of 50 nm pitch patterns of various doses are shown in Figure 3-4.

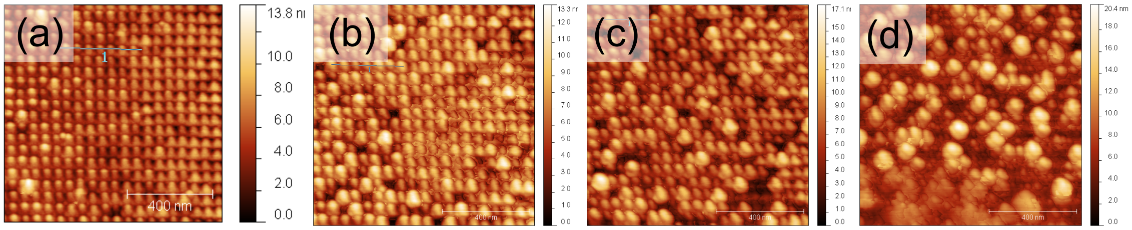

**Figure 3-4: 1 µm x 1 µm AFM micrographs of Ge (5.7 ML) deposited at 0.1 ML/min (0.0023 Å/s) on patterns dosed at (a) 7K ions/site, (b) 3.4K ions/site, (c) 2.0K ions/site, and (d) 700**

**ions/site. Each pattern has a pitch length of 50 nm.**

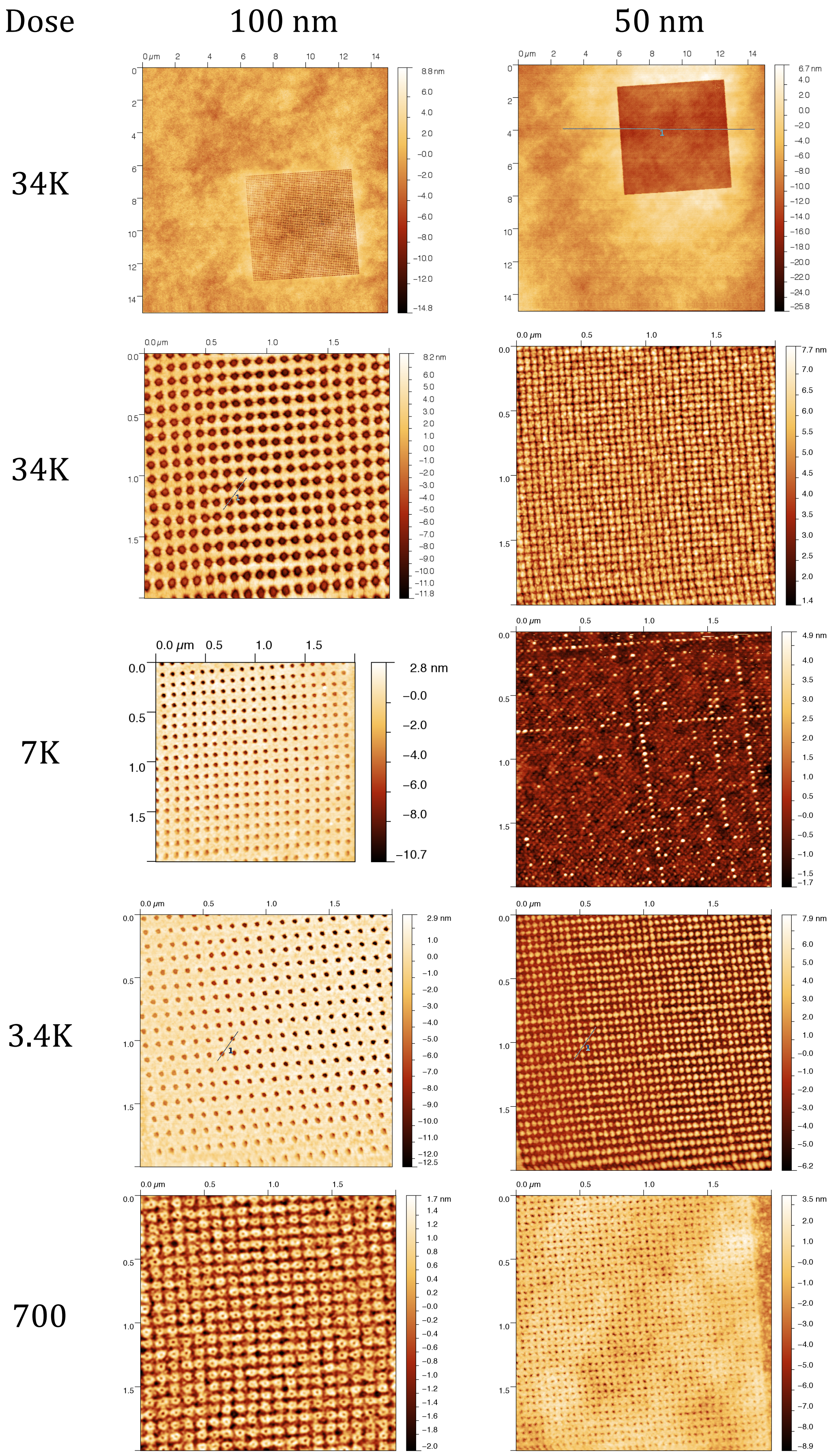

**Figure 3-5: AFM micrographs of Ge (5.5 ML) deposited at 0.1 Å/s at 450 °C on patterns dosed and spaced as shown.**

Additional growths were conducted in our MBE chamber. One sequence of patterns ranging in dose from 34K ions/site to 700 ions/site, and at pitch lengths of 100 nm and 50 nm is presented in Figure 3-5. The sample was prepped, patterned, and cleaned. The desorb temperature was at 580 °C; 5.5 ML of Ge was deposited at 450 °C. The series exhibits features common to many of our growths; features that we will address throughout this thesis.

At a high dose of 34K ions/site, 50 nm pitch the entire patterned region etches below the surface, while at 100 nm pitch, the pattern is retained and flush with the surrounding surface. (Fig 3-5, row 1) We attribute this effect to cascade overlap, where the sub-surface defective region of one patterned site overlaps with a defective region of another patterned site. The defectivity allows the RCA-2 solution (oxidizer) to penetrate across patterned sites below the surface during cleaning, and when the oxide is removed the entire area goes with it. It is interesting to note that for doses of 34 K and 7 K ions/site at 50 nm pitch, there is a residual pattern remaining after this phenomenon occurs.

The growth surface of the 7K ions/site – 50 nm pitch is shown in Fig. 3-6. We consider the raised features in (a) are QDs based on the AFM evidence. Profile scans of suspected dots as indicated in panel (a) are taken in the <100> crystallographic direction. The corresponding dots in panel (b) are circled in red, and appear because the scaling of the local slope plot was configured to highlight where in the scan slope angles are close to that of a {105} facet (11.3° +/- 1°). The angle of the sidewall of the dots is 11.4°, as shown in figure (c). The base of the QDs are 50 nm across. The QDs have the appearance of enhanced growth above misfit dislocations, but given the small Ge thickness and the height modified interface it seems unlikely.

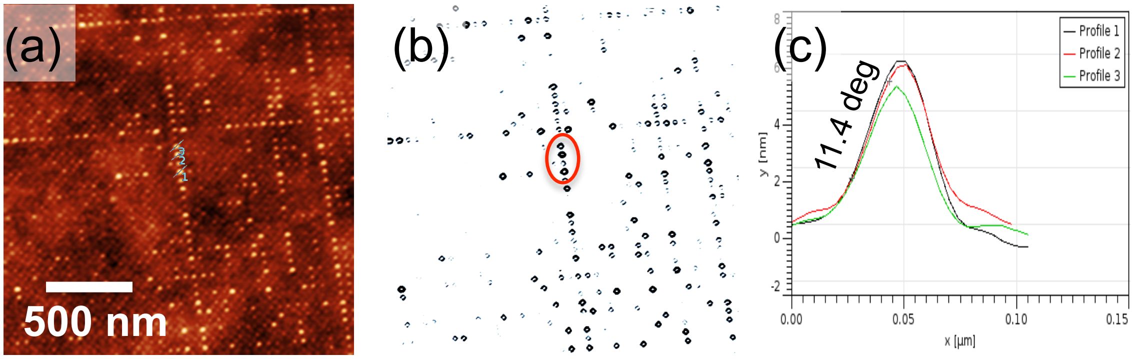

**Figure 3-6: (a) AFM micrograph of 7K ions/site pattern at 50 nm showing surface heights. (b) a slope plot of (a), where the range of angles shown in dark correspond to the {105} facet 11.3° +/- 1° . The red circle contains the QDs profiled in (c) Profile of selected QDs as shown in (a).**

# 4 2D Quantum Dot Arrays

*"Research is what I am doing when I don't know what I am doing.." –Wehrner von Braun*

In this chapter we develop a set of metrics to assess the quality of the individual arrays including periodicity, location, QD volume, and FIB site to QD correlations, as these are the critical features of the arrays. With these metrics in place we are able to assess the arrays to identify and describe trends in the growths. We can then explore various growth conditions and assess their impact on the overall quality of the array. Finally we observe that our QDs form as domes and nucleate unexpectedly on the tops of our features, not in the pits. We discuss our observations and potential explanations for this unexpected behavior.

## 4.1 Pattern fidelity vs dose

Ge deposition on FIB-patterned substrates produces ordered QD arrays to varying degrees. Fig. 4-1 shows a series of AFM micrographs of Ge QDs at 50 nm pitch with decreasing dose. There is a select range of ion doses that reproduce the underlying pattern with a high degree of fidelity. At 7000 ions/site (Fig. 4-1 (a)) the Ge does not replicate the pattern with any kind of fidelity. It appears in this scan the pattern is largely eroded, and is similar to the scan from the un-patterned region (Fig. 4-1 (f)). For the patterns where QDs ordered to some degree, we evaluated them for 1) location of QDs with respect to the 2D lattice site, 2) the size distribution of the QDs, and 3) site errors, which include vacancies and multiply occupied sites.

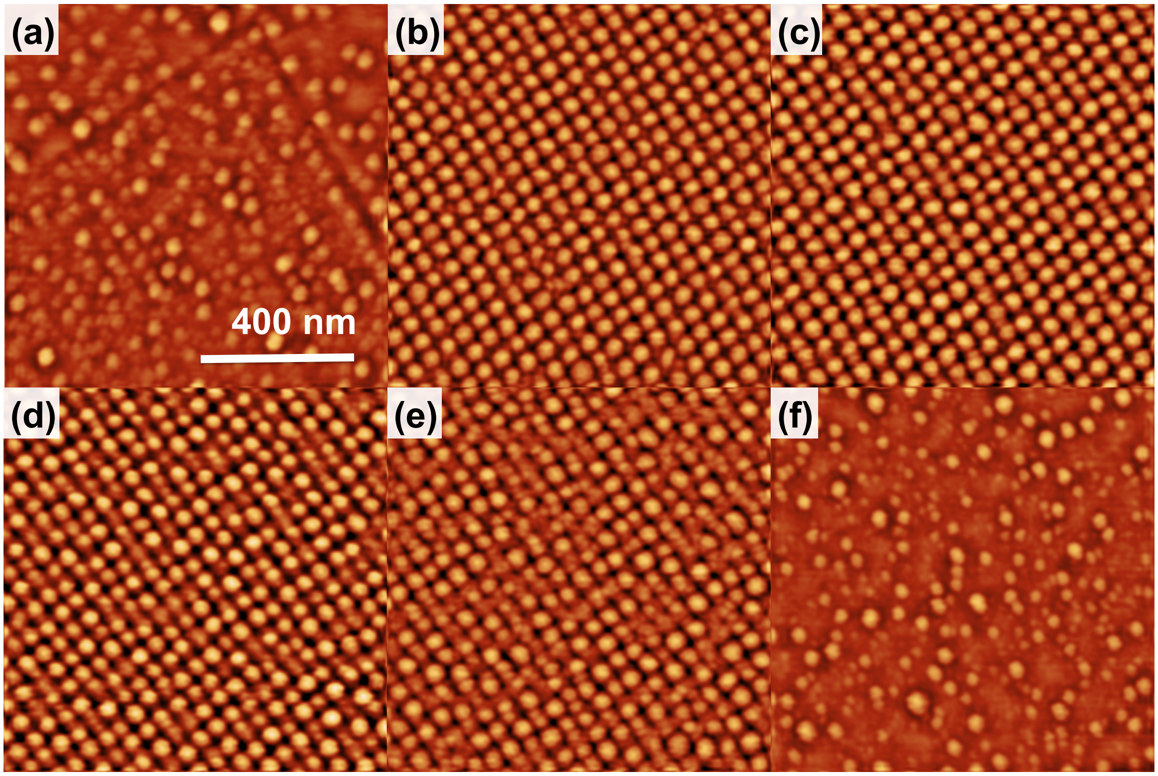

**Figure 4-1: 1 µm x1 µm AFM micrographs showing the Ge QD morphology on patterns formed with Ga+ doses of (a) 7000 ions/site, (b) 3400 ions/site, (c) 2000 ions/site, (d) 1400 ions/site, (e) 700 ions site, (f) off pattern. All samples were from a single growth.**

## 4.2 Pattern periodicity

To characterize periodicity, we evaluated the two dimensional fast Fourier transform (2D-FFT), by looking at the power spectrum density function (PSDF) for each AFM scan (Fig. 4-2). In all of the cases the primary peak is located at 0.19 nm$^{-1}$, which corresponds to a 52.6 nm row-to-row distance. The lattice vector orientations for 3.4K and 2K doses are at 96° to one another, which indicates there is a distortion in the lattice, i.e. the unit cell is oblique, with an internal angle of 84° (Figure 4-3 (a)). Comparing the AFM to an SEM of the same sample, the PSDF of the SEM shows that the pattern is actually orthogonal, and that the pattern and lattice distortion in the AFM is an artifact of

| Dose | Dot centroid position | 2D-FFT | PSDF (k = 1/spacing) |
|---|---|---|---|
| 3.4K | 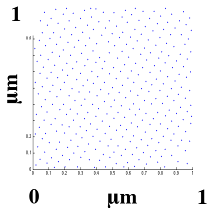 | 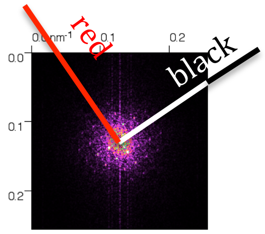 | 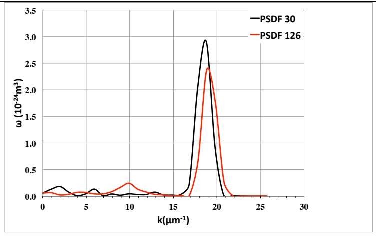 |
| 2K | 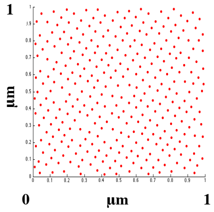 | 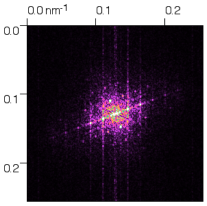 | 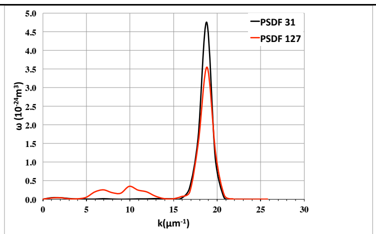 |
| 1.4K | 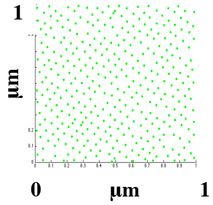 | 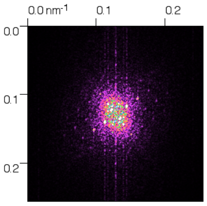 | 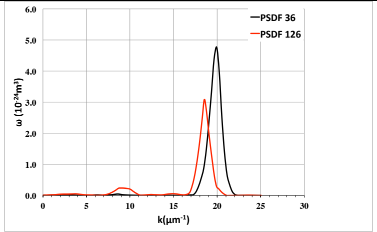 |
| 700 | 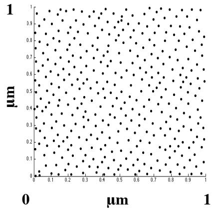 | 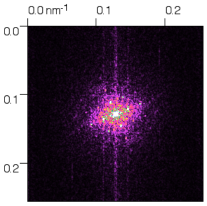 | 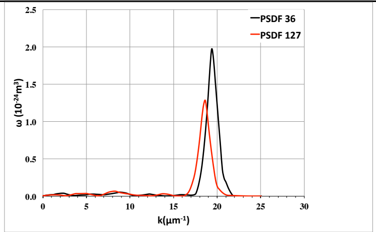 |
| off | 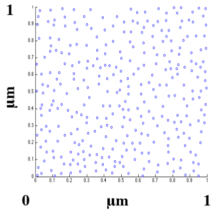 | 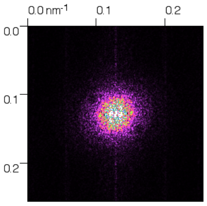 | 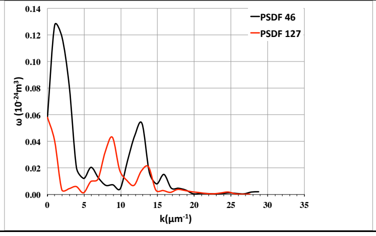 |

**Figure 4-2: column 1) Dose, column 2) Dot position plots, the data is from the centroid location of each identified dot from thresholding process, column 3) FFT from AFM, and column 4) plots of PSDF.**

the scan. However, the PSDF of the SEM also suggests that the pattern is not square. The interdot spacings from the PSDF are 49.1 nm and 46.2 nm for the x and y axes respectively. Some loss of dimensional accuracy can be explained by scaling errors of the TIFF image in the analysis software, as the pixel to distance conversions are done by estimating the scale; the difference in the relative lattice spacing is harder to explain, as it would require a 20° tilt in the sample during imaging. Finally, the amplitude of a PSDF peak is directly related to the identifiable components of a particular spatial period, in the case of the AFM, ~52.6 nm. The relatively large amplitude for 3.4K, 2K, and 1.4K at that spatial frequency suggests these arrays are of a high quality. The results for an off-pattern scan are provided for comparison in Fig. 4-2.

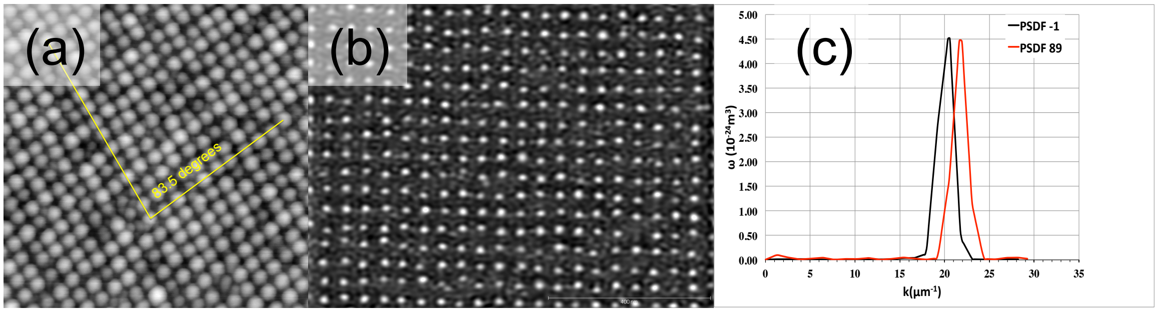

**Figure 4-3 (a) 1 μm x 1 μm AFM micrograph of 3.4K ions/site pattern. The inscribed angle was measured in ImageJ. Note the slight deviation from the centerline of the QDs. (b) SEM of the same sample. (c) PSDF generated from SEM.**

## 4.3 QD size distribution

The most appropriate figure of merit for uniformity of the QD "size" is a normalized distribution width:

$$\gamma = s/<V> \qquad \textit{Equation 4-1}$$

where $s$ is the standard deviation and $<V>$ is the mean volume. A primary challenge in determining the QD volume is choosing an appropriate threshold to represent the value of the baseline height. For these samples, 1 x 1 μm AFM scans are selected from the center portion of each sample. This yields a sample size of approximately 400 QDs for each pattern. The scans were plane-flattened and filtered to reduce high-frequency noise and low frequency baseline variations.

A mask was created in the software to identify and measure the QDs. A "watershed" algorithm was used which identifies local minima (maxima) in the surface, and fills them to a baseline height, which is determined by the threshold level. Since our QDs are positive features, the surface is inverted for calculation purposes. First, the QDs are identified by the software placing a virtual droplet on the surface which flows to the lowest contiguous point. When droplets flow to the same minima they merge. An identifier is assigned to each local minima, and after all the minima are identified, the process is repeated a user defined number of times, filling the surface. The droplet size can be adjusted to optimize the filling of QDs. Erroneously identified low points can be manually eliminated. Once the initial identification part is completed, the baseline of the dot is determined by the size of the droplets and the number of iterations. This process is preferred to simple value thresholding to avoid the issues of baseline variation or variation in the heights of the QDs. Eventually, the surface fills and boundaries may form when two filled areas impinge upon each other. Data are available for the QD's attributes, including volume, height, projected surface shape, projected surface area, surface area, location, etc.

Figure 4-4 shows the effect on the masked region of the sample of increasing the number of iterations. The volume, equivalent radius, the standard deviation of each, and their respective ratios for each different threshold level are shown in the table. The mean volume increases monotonically (as shown in Fig. 4-5 (a)), with the maximum relative standard deviation for the mean volume at 550 iterations. This can be attributed to the projected area decreasing less rapidly once the QDs are “filled”. At the outset, the volume and size distribution are largely influenced by the tip of each dot. As the dots are filled more fully by increasing the number of iterations, variations e.g. QD height will begin to influence the distribution.

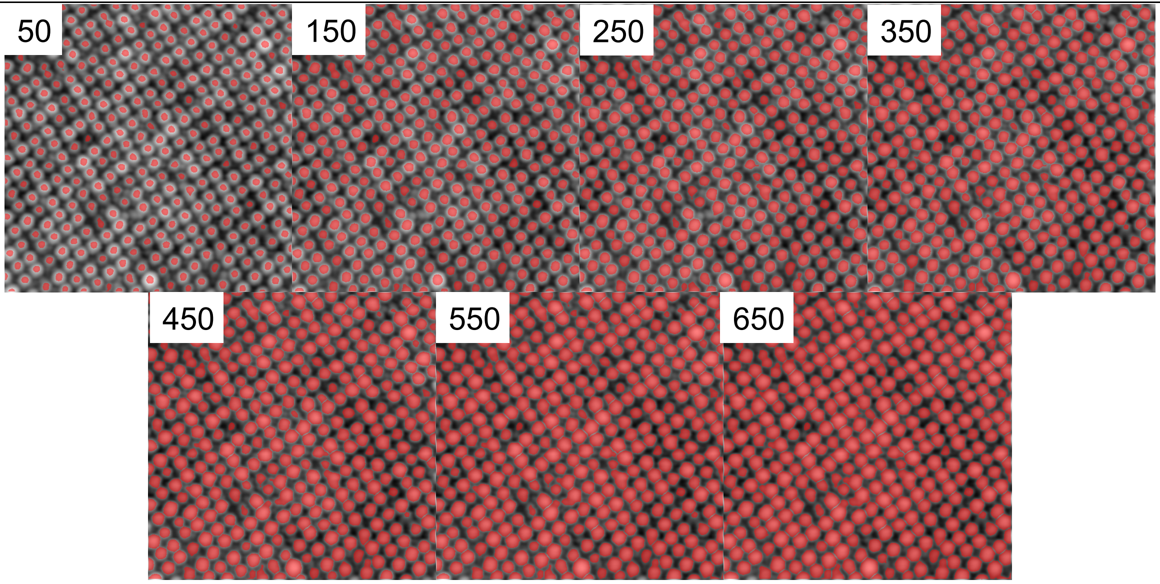

| | 50 | 150 | 250 | 350 | 450 | 550 | 650 |
|---|---|---|---|---|---|---|---|
| Mean Volume | 3.23E-25 | 1.03E-24 | 1.75E-24 | 2.46E-24 | 3.17E-24 | 3.86E-24 | 4.59E-24 |
| std dev | 9.79E-26 | 3.38E-25 | 6.94E-25 | 1.16E-24 | 1.56E-24 | 1.94E-24 | 2.22E-24 |
| γ | 0.30 | 0.33 | 0.40 | 0.47 | 0.49 | 0.50 | 0.48 |
| | | | | | | | |
| Mean Radius | 1.13E-08 | 1.54E-08 | 1.77E-08 | 1.93E-08 | 2.08E-08 | 2.20E-08 | 2.32E-08 |
| std dev | 1.30E-09 | 1.87E-09 | 2.60E-09 | 3.34E-09 | 3.64E-09 | 4.05E-09 | 3.83E-09 |
| γ | 0.12 | 0.12 | 0.15 | 0.17 | 0.18 | 0.18 | 0.17 |
| | | | | | | | |
| Height | 2.40E-09 | 4.16E-09 | 5.35E-09 | 6.28E-09 | 7.01E-09 | 7.64E-09 | 8.15E-09 |

**Figure 4-4: Fill data for various iteration settings for 3.4K ions/site dosing; the number in the left corner is the number of droplets used in the watershed algorithm.**

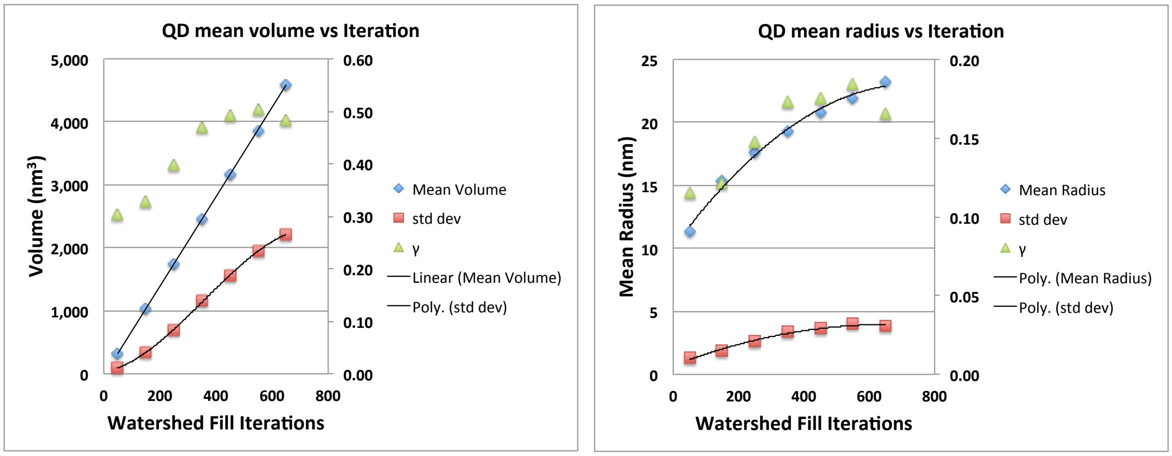

**Figure 4-5: Fill data plotted for Mean Volume (a) and Mean Radius (b) vs. fill iterations for 3.4K ions/site dosing**

For patterns where minima are clearly evident, i.e. a pattern of well formed QDs, the thresholding is straightforward. For patterns with not clearly defined minima, e.g. QDs formed on rough surfaces, the approach is much more subjective, as distinguishing between local minima in the surface relative to small QDs is more difficult. Later, as filling progresses, differences in the volumes of the QDs can lead to some QDs being underfilled, while some QDs will be overfilled and the droplet spreading quickly across the surface. We settled on 500 iterations for this set of patterns for two reasons: the first is that at 500 iterations all of the measured patterns stayed contained, i.e. no significant overfilling of QDs occurred; second, our figure of merit $\gamma$, becomes less sensitive after 400 iterations so while the overall measured volumes will increase the normalized volume distribution width does not. In terms of the normalized volume distribution width, this is a conservative measurement.

## Table 4-1: QD statisitics vs dose

| Ions/site | 3.4K-50 | 2.0K-50 | 1.4K-50 | 700-50 | 700-35 | Off pattern | 2.0K-50 500C |
|---|---|---|---|---|---|---|---|
| Mean dot volume (nm$^3$) | 3432 | 4210 | 4261 | 3855 | 2663 | 485 | 6184 |
| Std dev. | 995 | 1191 | 1693 | 1793 | 2155 | 454 | 1353 |
| γ | 0.290 | 0.283 | 0.397 | 0.465 | 0.890 | 0.935 | 0.219 |
| Mean dot radius (nm) | 21.9 | 22.7 | 23.5 | 25.0 | 18.7 | 15.8 | 23.15 |
| Std dev. | 3.51 | 3.18 | 4.99 | 6.39 | 5.55 | 6.71 | 2.27 |
| γ | 0.160 | 0.140 | 0.212 | 0.256 | 0.298 | 0.424 | 0.098 |
| Mean dot height (nm) | 4.47 | 5.16 | 5.25 | 4.19 | 3.85 | 1.12 | 7.24 |
| Std dev. | 0.64 | 0.86 | 1.10 | 1.17 | 1.62 | 0.71 | 0.894 |
| γ | 0.143 | 0.167 | 0.210 | 0.279 | 0.422 | 0.630 | 0.124 |
| Site error fraction | 5/360<br>0.014 | 19/340<br>0.055 | 54/383<br>0.14 | 122/382*<br>0.32 | 194/737<br>0.14 | | 0/379 |
| Mean dot spacing 001 (nm) | 53.1 | 53.2 | 50.1 | 51.0 | 34.6 | | 50.7 |
| FWHM | 6.2 | 4.3 | 3.3 | 5.0 | 2.1 | | 5.5 |
| Mean dot spacing 010 | 52.8 | 53.2 | 52.9 | 53.2 | 35.7 | | 52.6 |
| FWHM | 5.1 | 4.4 | 5.1 | 4.4 | 1.6 | | 3.9 |
| Mean crown volume (nm$^3$) | 591 | 917 | 912 | 103 | | | |
| Std dev. | 372 | 313 | 272 | 73 | | | |
| γ | 0.63 | 0.34 | 0.30 | 0.71 | | | |
| surface RMS (nm) | 0.839 | 0.961 | 1.007 | 0.542 | | | |

*76 vacancies, 46 multiple occupancy

We collected data from a series of patterns using this approach. It should be noted that the volumes will be overestimated firstly because of tip convolution (see Fig. 4-3 and Fig. 2-13); in figure 4-3, the AFM (a) shows dots that largely fill the space, whereas the SEM (b) fills only a fraction of the space. The SEM will underestimate the size of the QD because of the inability to differentiate the outline of the QD near the base from the wetting layer. The actual size of the QDs is likely somewhere in between. Secondly, incorporation of the substrate in the thresholding process is probable. As previously described, one of the key indicators that the QDs are overfilling during thresholding is when spreading on the surface occurs. In the case where the surface is

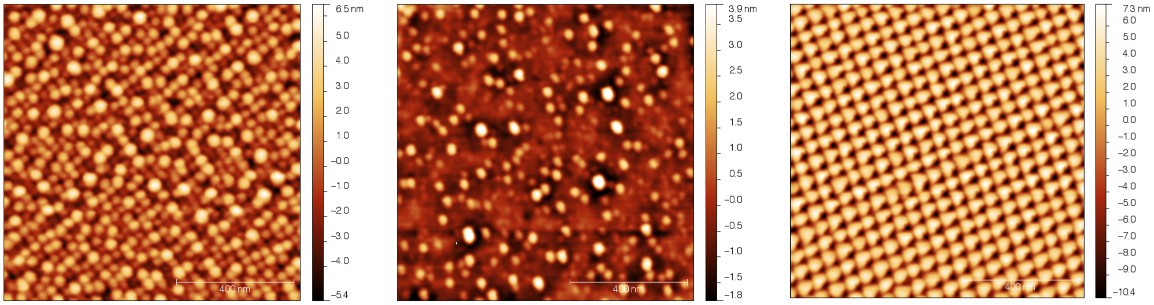

**Figure 4-6: 1 µm x 1µm AFM micrographs of patterns included in table 4-1. (a) 700 ions/site @ 35 nm pitch, (b) off pattern of the same sample grown at 450C, and (c) 2 K ions/site @ 50 nm pitch grown at 500C.**

highly corrugated in two dimensions it is much more difficult to detect. The data for the series of samples is summarized in Table 4-1. AFM micrographs for samples reported in Table 4-1 but not shown previously can be found in Fig. 4-6.

From figure 4-7, doses 3.4K and 2.0K have a similar normalized distribution width ($\gamma$), which then increases at lower dose, while the mean volume is at a maximum in the 2.0K to 1.4K ions/site QDs, and then decreases at 700 ions/site.

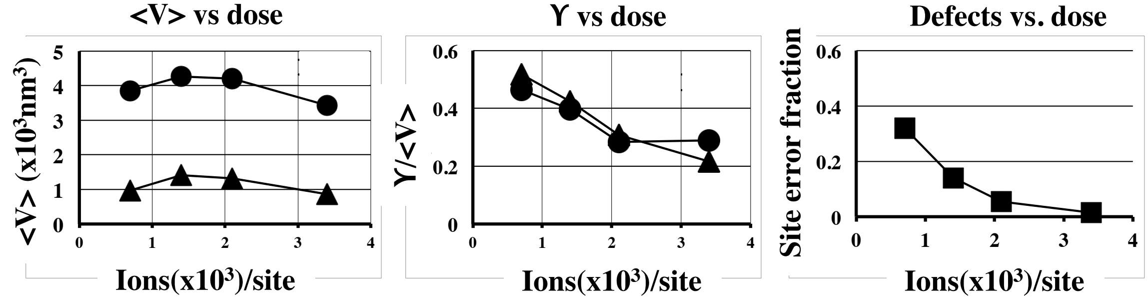

**Figure 4-7: Plots of (1) mean volume <V> of QDs (filled circles) and crowns (filled triangles) vs. dose, (2) $\gamma$/<V> of QDs (filled circles) and crowns (filled triangles) vs. dose, and (3) site error fraction vs. dose.**

## 4.4 Site error fraction

The site error fraction (fraction of FIB sites with no QD, or multiple QDs) is determined by manual counting of the sites where QDs are expected to be:

*Site error fraction = # errors/# potential sites* *Equation 4-2*

They are categorized as occupied by a single QD (no error), multiple QDs (error), or no QDs (error). Each 1 μm x1 μm sample of a 50 nm pitch array contains close to 400 QDs. Well-formed arrays are typical of the larger arrays from which the imaging area was selected. The results of our assessment of these patterns is summarized in Table 4-1, while the site error fraction vs. dose is plotted in Fig. 4-7.

## 4.5 The effect of temperature on growth

Four separate sample series were prepared identically to the series of samples in Fig. 4-1 except for growth temperature. Each was dipped in HF, desorbed at 550 °C, and then 5 ML of Ge was deposited at different growth temperatures as indicated in Fig. 4-8. Statistics were compiled for each of the samples. At 500 °C the patterns show improvements in uniformity vs. growth at 450 ºC. The results for 2.0K ions/site pattern at 500 °C is included in Table 4-1. Comparing it to 2.0K @ 450 °C, it includes a decrease in $\gamma_{<V>}$ from 0.28 to 0.22, a decrease in $\gamma_{<r>}$ (mean radius) from 0.14 to 0.10, and a decrease in $\gamma_{<h>}$ (mean height) from 0.17 to 0.12. There were also zero site errors compared to 19/340. The mean volume distributions were plotted for the 2K ions/site dose for each of these temperatures, 450 °C, 500 °C, and 550 °C, see Fig. 4-9. The distribution broadening clearly indicates there is a loss of pattern fidelity as there exists some coarsening and coalescence of QDs at 550 °C and 625 °C. The coarsening on patterned substrates is clearly reduced relative to the corresponding off pattern micrographs.

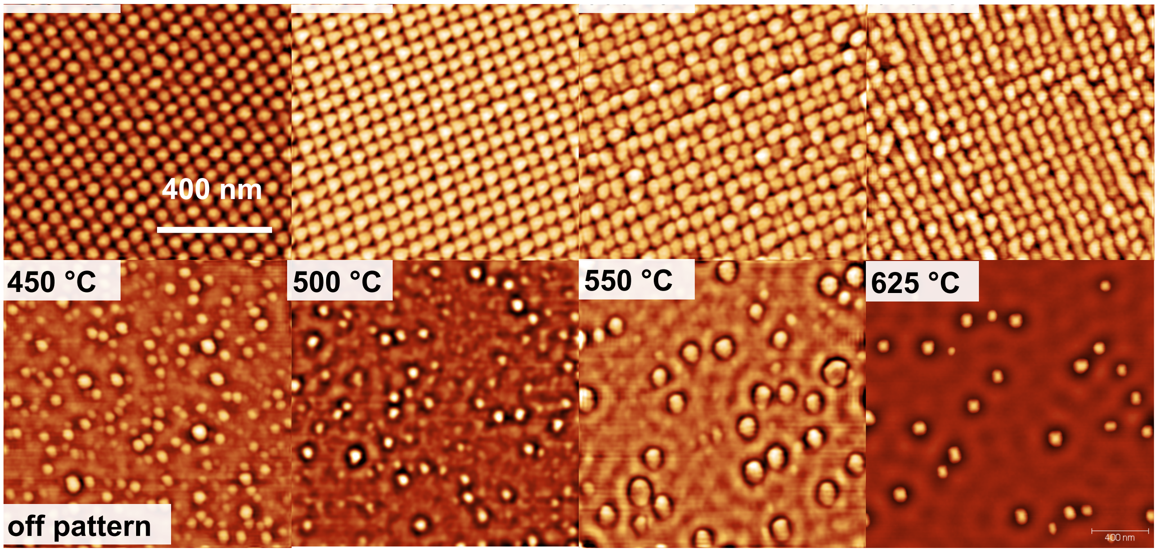

**Figure 4-8: Top row: Four samples showing QD growth on 2.0K ions/site patterns at four different growth temperatures. Bottom row: off pattern scans from the corresponding wafers.**

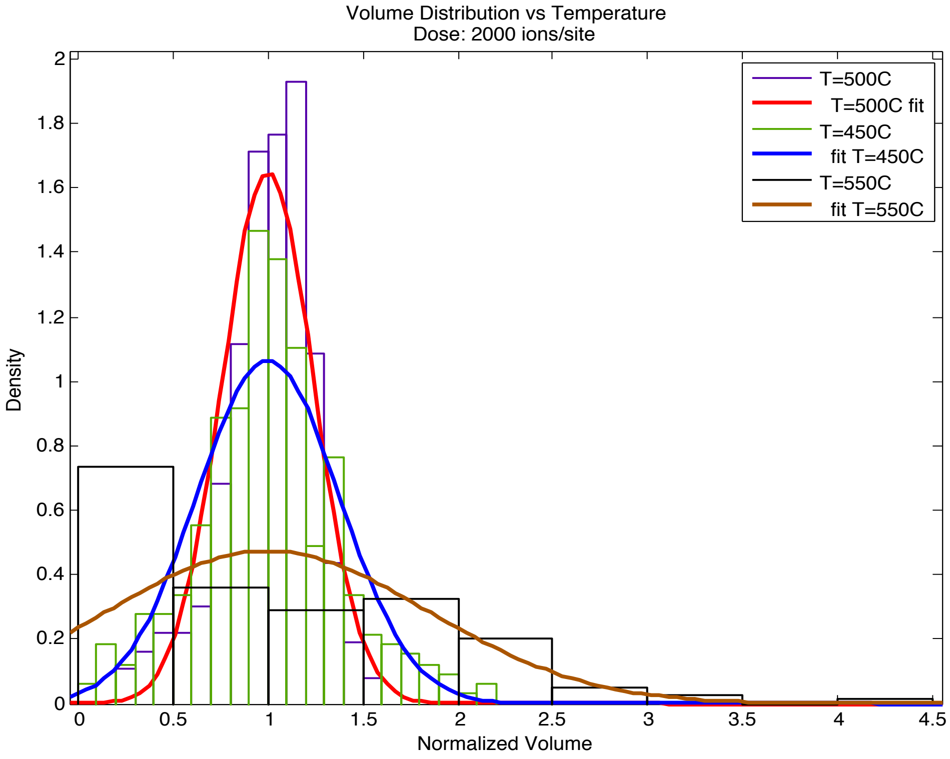

**Figure 4-9: Histograms of the normalized mean volumes for 2K ions/site dose at 450 °C (green), 500 °C (purple), and 550 °C (black). Gaussian fits to the data are also plotted: 450 °C (blue), 500 °C (red), and 550 °C (brown).**

## 4.6 Surface morphology

Trepidation arose when some of our low coverage patterns with Ge QDs appeared in the AFM as very similar to the Si surface patterns. We were concerned we were not nucleating QDs, but that conformal growth of the Ge might be occurring on the pre-imposed surface pattern. To investigate this we scanned a series of samples in identifiable regions that we could return to, e.g. pattern corners. We then selectively etched off the Ge and examined the same areas without the Ge. This enables a direct comparison between the QD formation and the underlying substrate, and allows us to identify the driving forces behind the nucleation of QDs.

There are two common Ge etches, $H_2O$ at 90 °C, [97,98] and hot dilute $H_2O_2$ (30%) at 90 °C. [98–100] $H_2O$ doesn't etch Ge directly but does etch $GeO_2$. Ge oxidizes in $H_2O$ and then the $H_2O$ etches the oxide. The etch rate for 100% Ge is ~ 200 Å/min; $H_2O$ does not etch $Si_{1-x}Ge_x$ for $x < 0.60$. The etch rates for $Si_{1-x}Ge_x$ in $H_2O_2$ at 90 °C are 4,000 Å/min for $x=1.00$; 1,000 Å/min for $x = 0.80$; and 0 for $x < 0.60$. We used hot $H_2O$, which successfully removed the Ge as shown in Fig. 4-10.

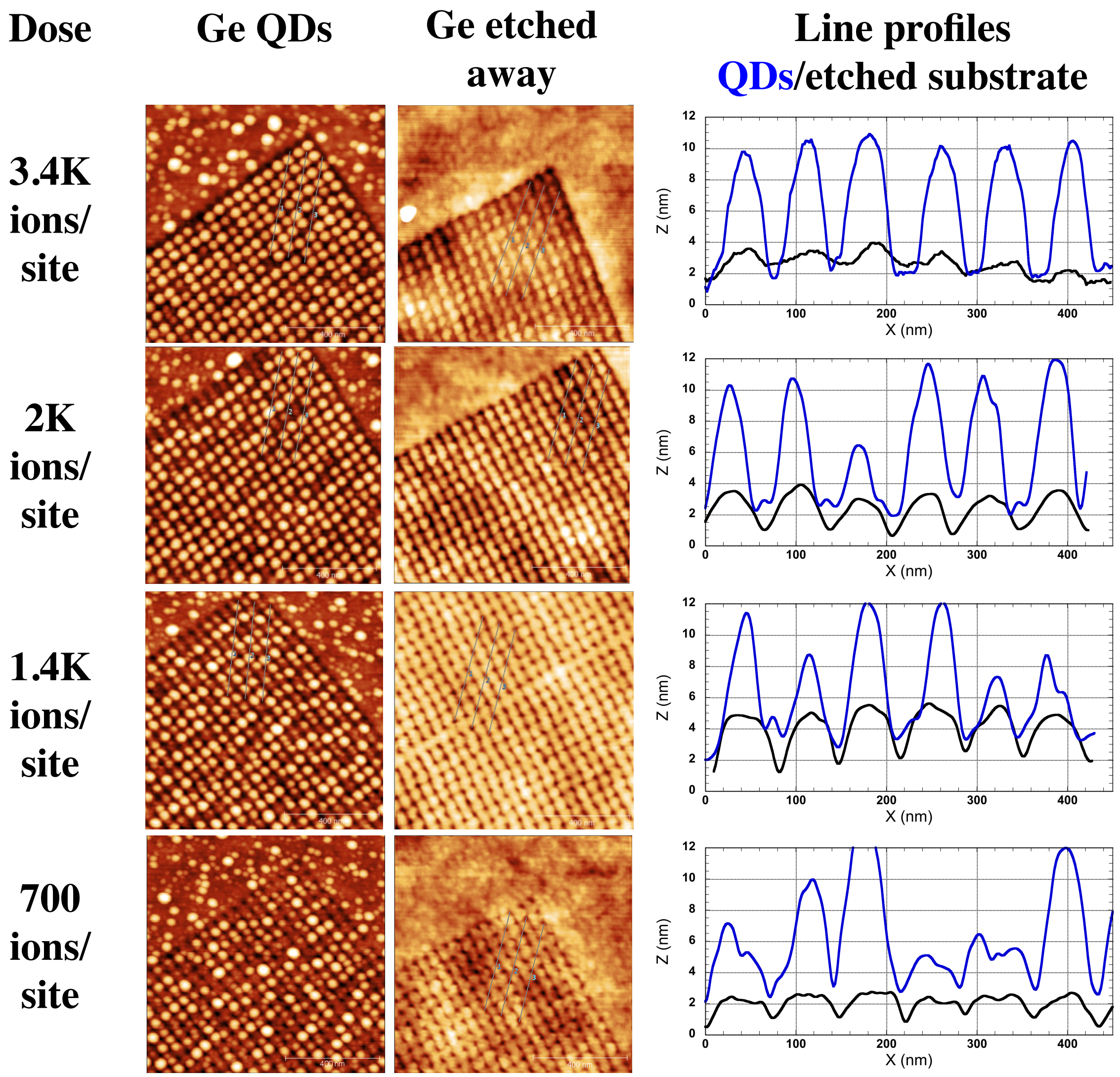

**Figure 4-10: Corner scans of a series of patterns of different dose. In column (1) 5.5 ML of Ge, column (2) Ge etched off, and (3) correlated scans with Ge (blue) and without Ge (black).**

Under close examination (Fig. 4-10) it becomes evident that the QDs are forming in the four-fold region *in between the patterned pits*, in the "on top" position in contrast to many of the previous reported experiments where self-assembly of the QDs is directed to the pits. Additionally, the underlying pre-imposed morphology does not seem to possess the classic "pit in terrace" morphology, where discrete pits are formed into a planar surface, with the exception of the 700 ions site pattern. At higher doses the surface appears more continuously modulated. (Fig. 4-10 column (3))

We measured the stripped samples in the AFM and compiled statistics for both the pits as well as the "crown" (the regions between four nearest-neighbor pits). Periodicities of the pits were measured with an overall average mean distance of 50.3 ± 2.1 nm and a mean FWHM of 4.0 nm. The results of the pit spacing measurements are summarized in Table 4-2.

The normalized volume distributions for both QDs and the underlying crowns are nearly identical for each successive dose, with a broadening distribution with decreasing dose (Fig. 4-11). The uniformity between the QD volume distributions and that of the crowns could be an indication that the Ge just conformally coats the surface, however there is a significant volume difference between the surfaces with QDs and without. There arises from the difference in the amplitude of the surface modulation between the etched and un-etched surfaces: the etched surface has a height modulation of 2-3 nm, whereas the un-etched surface has height modulations of 8–10 nm. Finally the maximum surface angle for the etched surface is 8° - 10°, where the un-etched surface has surface facets of 25°. While there is sufficient Ge mobility to form QDs on the crowned surface, the suppression of coarsening at such short length scales is a strong indication that deposited material is largely confined to the 2D unit cell defined by an array of four pits and the crown in the middle. Crown volume data is included in Table 4-1.

**Table 4-2: Pit spacing measurements**

| Pit spacing | | | | | |
|---|---|---|---|---|---|
| Dose | 3.4K | 2.0K | 1.4K | 700 | average |
| x (nm) | 49.0 | 51.8 | 51.8 | 51.3 | 51.0 |
| x-FWHM (nm) | 4.0 | 3.8 | 3.6 | 4.9 | 4.1 |
| orientation (deg.) | 28 | 22 | 21 | 23 | 23.5 |
| | | | | | |
| y (nm) | 46.5 | 48.5 | 50.7 | 52.9 | 49.7 |
| y-FWHM (nm) | 3.3 | 3.3 | 4.0 | 4.9 | 3.9 |
| orientation (deg) | 112 | 113 | 114 | 115 | 113.5 |
| angle (deg) | 84 | 91 | 93 | 92 | 90.0 |
| | | | | | |

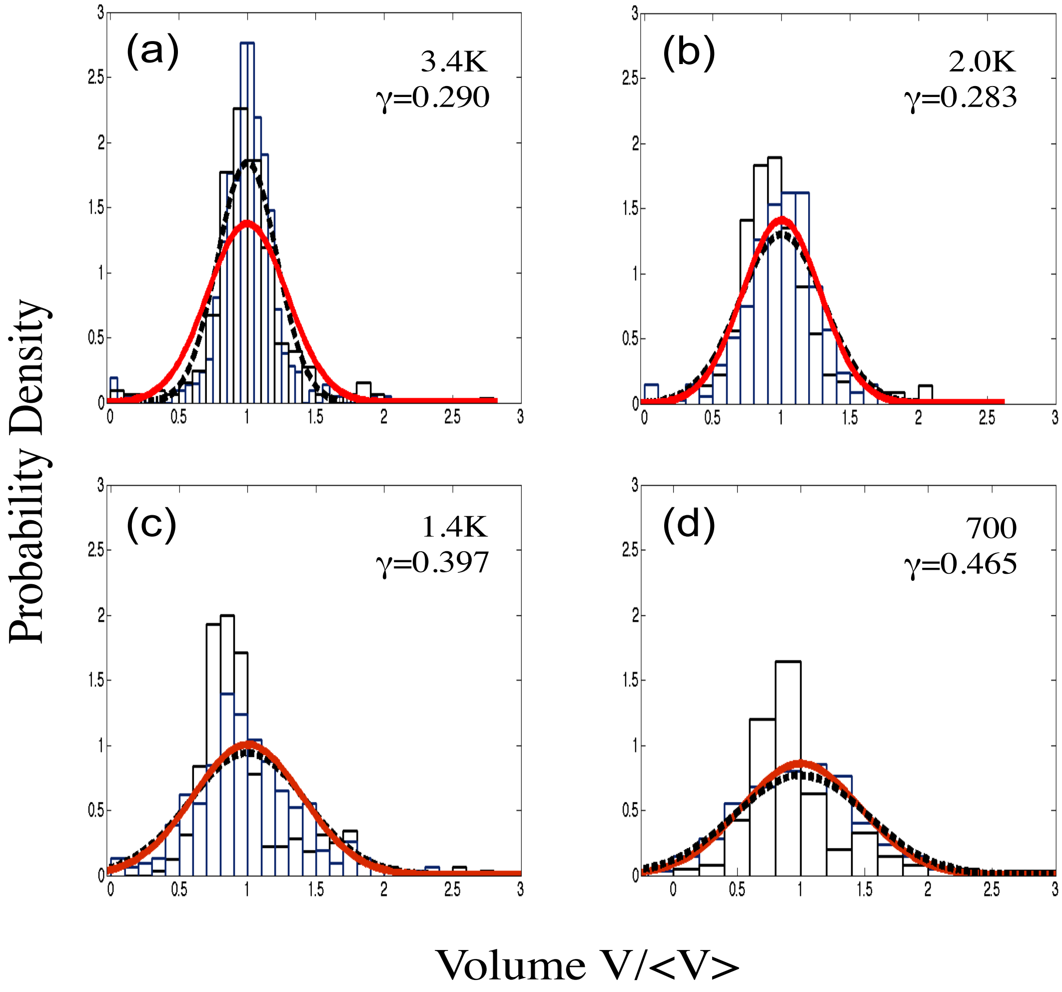

**Figure 4-11: Normalized volume histograms and Gaussian fits for both QDs (red) and crowns (dotted black) plotted as probability distribution functions.**

## 4.7 TEM: 3.4K ions/site

Working with Joshua Maier at Penn State University, we were able to obtain cross-section FIB liftouts from both the 3.4K and 700 patterns after stripping the Ge. The 3.4K pattern is 4 μm wide and the entire cross section of the pattern can be seen in Fig. 4-12. There are 79 observable patterned features, and the following identified features are numbered: 1, 10, 20, 30, 40, 50, 60, 70, and 79. The magnified section illustrates the direction of the numbered features between 38 and 42.

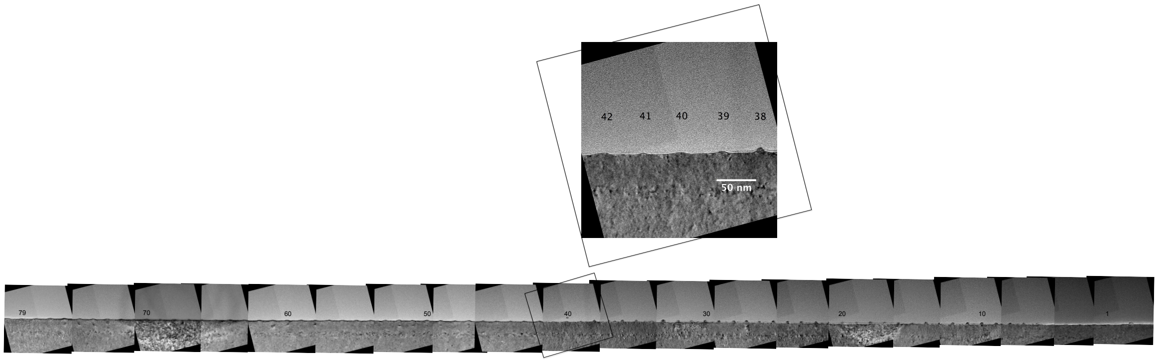

**Figure 4-12: TEM cross-section of 3.4K ions/site patterned surface, after growth and Ge etching. TEM micrographs are stitched together to create the cross section. Features 38-42 are enlarged for clarification.**

There are two distinct regions in this pattern cross-section: the left side where the Ge wet-etched cleanly (dots 39-79), and the right side where the Ge QDs were preserved, due to passivation of the Ge surface following residual contamination from previous AFM scans (dots 1-38). These regions are clearly delineated in the HAADF-STEM images as the Ge appears bright white relative to the Si substrate in the images (Fig. 4-13). In image 4-13 (a) there is no Ge on the surface while in image 4-13 (b) there are pronounced Ge islands.

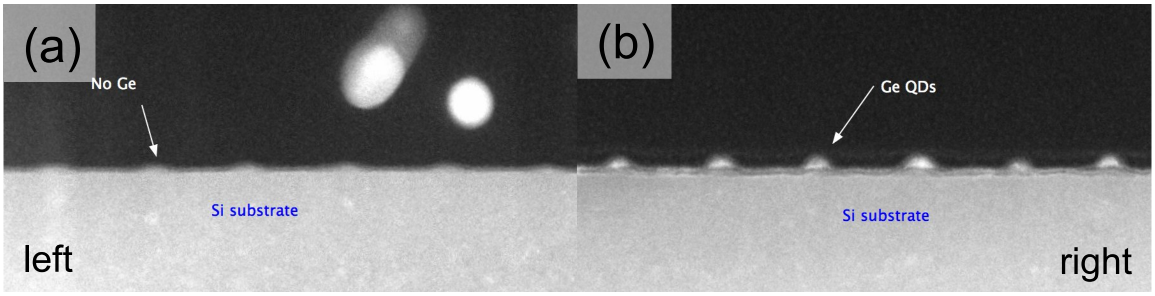

**Figure 4-13: HAADF stem images of 3.4K ions/site pattern after Ge etching. (a) Region where etching removed all Ge. (b) Region where Ge remained due to some previous contamination.**

The morphology of the etched Ge surface is ***different in TEM than what we expected.*** Instead of a sinusoidal surface with pits and or crowns, we have a surface with small Si peaks on a relatively smooth surface. The AFM of the sample (Fig. 4-14 (a)) suggests that we have crowns, whereas a linescan in the <001> direction in the array shows a continuous surface modulation with an amplitude of 2 nm. (Fig. 4-14 (b)) Linescans taken along <110>, showing the saddle points in between the crowns have surface modulations between 0.5 – 1.0 nm (Fig. 4-15 (c)). By properly scaling the z-height of the AFM data, we can superimpose it onto the TEM micrograph for comparison (Fig. 4-14 (d)). The AFM scan is clearly overestimating the shape of the “crown” which is in fact a small peak, and while the AFM measures the vertical heights accurately, there is characteristic difference between the AFM profile and the profile revealed by TEM.

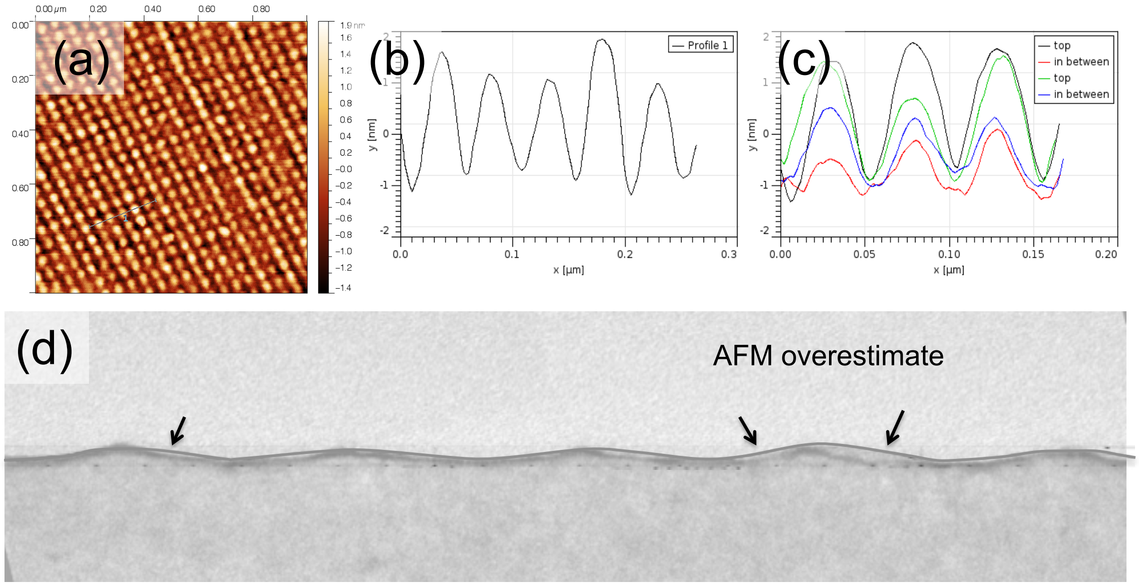

**Figure 4-14: (a) 1 µm x 1 µm AFM micrograph of 3.4K pattern after removal of Ge. (b) a linescan in the <001> direction of the pattern. This linescan is inscribed on (d). (c) Multiple linescans on the AFM micrograph: two scans over crowns <001>, two scans through the pits. (d) BF TEM cross-section of the sample with AFM linescan (b) superimposed, showing AFM tip convolution, and volumetric overestimation.**

Tip convolution is a likely suspect, but given that the mounds are 40 nm across with a height = 2 nm, using a spherical approximation and a simple radius calculation would suggest that the tip radius is > 56 nm.[1] The tip specification is < 10 nm, with 6 nm being typical, so either our tips are much worse than specification or something else is responsible. We also considered that the TEM section only sliced through a small portion of a larger surface feature, but since the spacing between rows is only 50 nm, this would require the cross-section to be of order 25 nm thick.

Figure 4-15 is a TEM image showing the same sample with a sequence of peaks spaced at 50 nm. The apices of the peaks are measured to a baseline inscribed on the

---

[1] R_tip = (1/2H)*(R_AFM^2 – R_TEM^2)

image. The peak heights range from 1.7 nm to 3.2 nm. The inscribed angle at the apex was measured for each dot. The angles range from 159°-153°, meaning the sidewall angles are in general ≥ 10°. The last feature, dot 38 (two dots to the right of 40), is capped with a round topped Ge cluster (see enlarged inset). The overall height of the dot is 7.24 nm, with a radius of 5 nm. The surface feature which it stands on measured 2.9 nm, but had a significantly larger sidewall angle, ~ 22°.

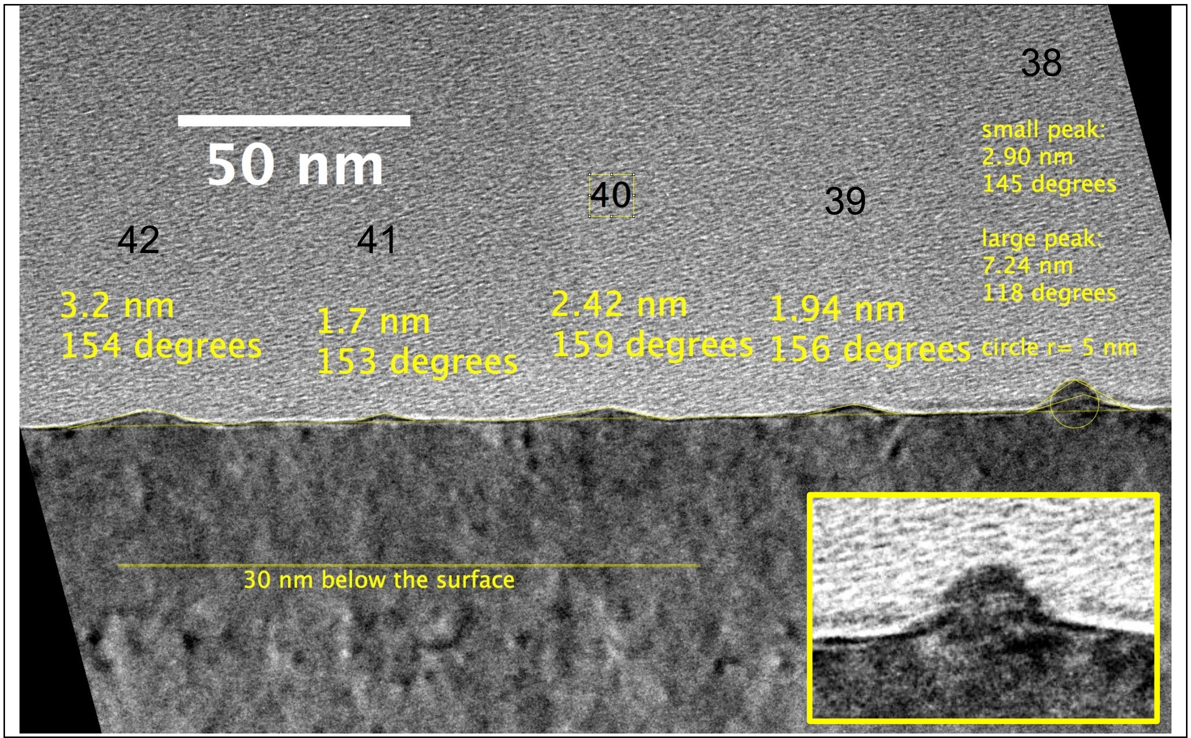

**Figure 4-15: XTEM of peaks 42-38 (numbered). The heights of the peaks and the inscribed angle of the peak are shown. View along <110> zone axis. Processing done in ImageJ. Inset: Magnified peak 38.**

## 4.8 TEM: 700 ions/site

Pattern 700, despite being patterned with many fewer ions, has a much more robust morphology in TEM. The surface is a continuously modulated 50 nm wave with an amplitude of 3 nm (Fig. 4-16 (a) and (b)). The QDs that have formed (and remain) have again formed on the crowns of the surface. The QD's also possess well-delineated facets whose inclination is close to that of {113} (Fig. 4-16-(c) and (d)). The sidewalls of the Si surface modulations are measured around 11.4° (105). We have discounted the notion that there has been a significant amount of intermixing, given the low growth temperatures, the removal of Ge after etching on the AFM scans, the absence of a Ge wetting layer or QDs on the substrate off pattern (HAADF-STEM), and the removal of Ge on large portions of the 3.4K ions/site sample. (700 and 3.4K ions/site were processed simultaneously).

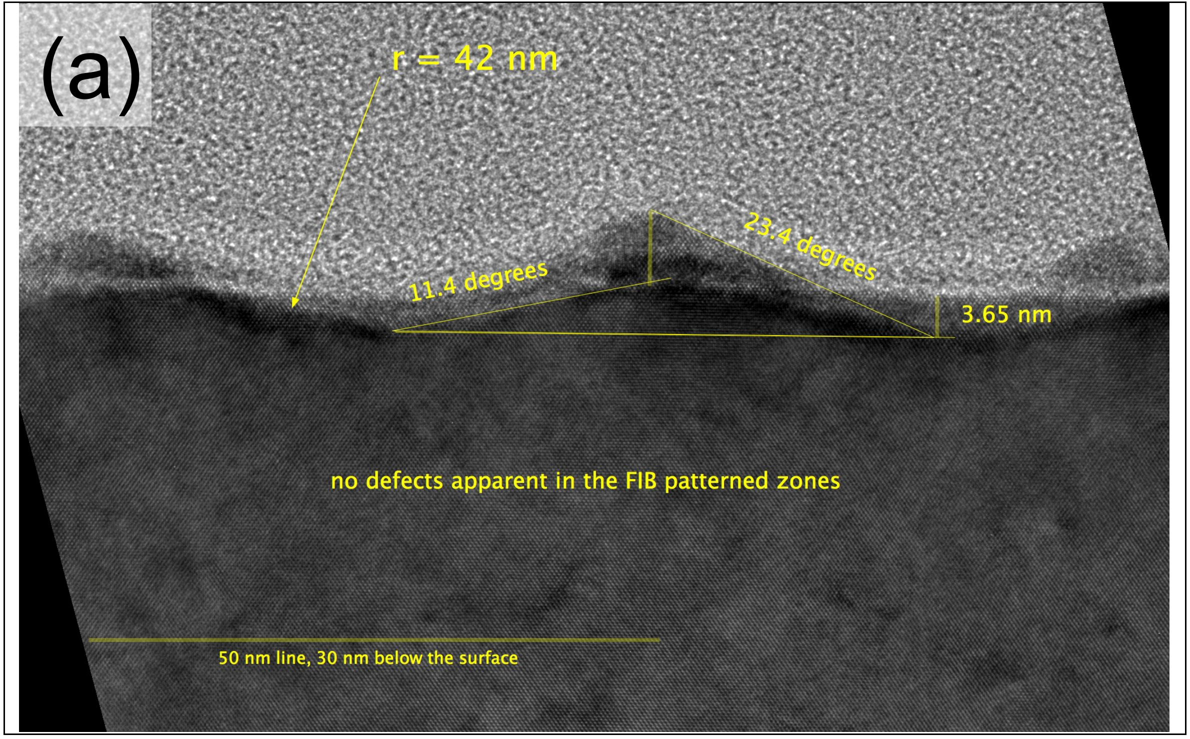

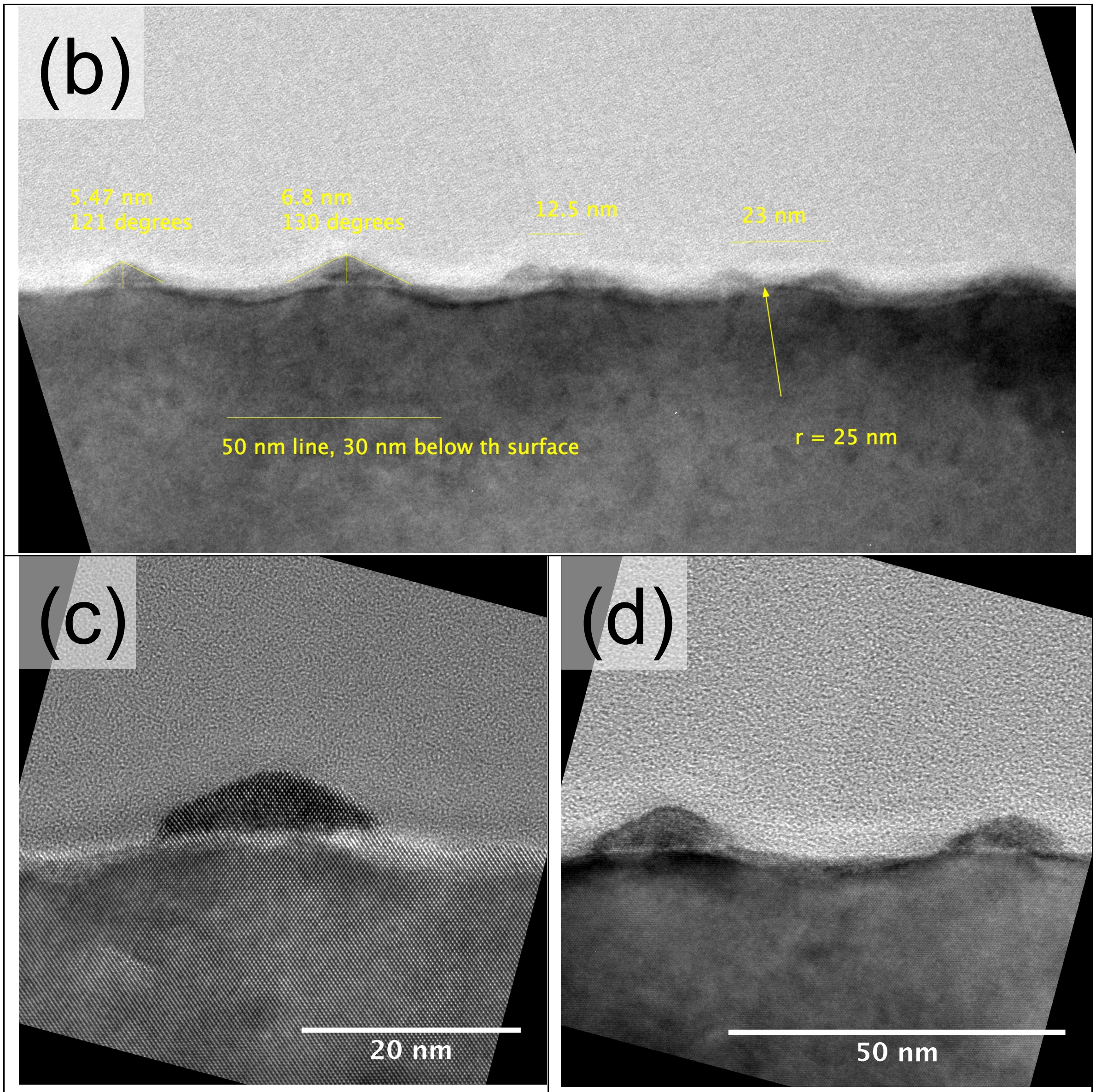

**Figure 4-16: Figure 4-21: (a) TEM micrograph of 700 ions/site sample. <110 zone axis>. The surface is characterized by a large sinusoidal pattern and faceted QD growth on the crests (crowns) of the surface. (b) series of QDs on crests. (c) and (d) Ge QDs <110> zone axis.**

Similar to the 3.4K ions/site sample, there is evidence of surface contamination from AFM scans of the post-growth (but pre-etched) surface (Fig 4-17).

*The formation of QDs on the crowns of this modulated surface is remarkable*. The high-resolution images of Fig. 4-16 show lattice planes running through the crystals from the substrate, confirming epitaxial growth. This confirms that the mass transport of Ge to the tops is intrinsic in nature and driven by the energetics of the configuration, as opposed to other factors. For example, one hypothesis we considered for QDs forming on our crowns instead of pits prior to the TEM data, was the potential for retained defectivity within the pits from the FIB processing, where the sticking coefficient would be low within the pits. However, at least for this sample, the higher-resolution images indicate that this is clearly not the case.

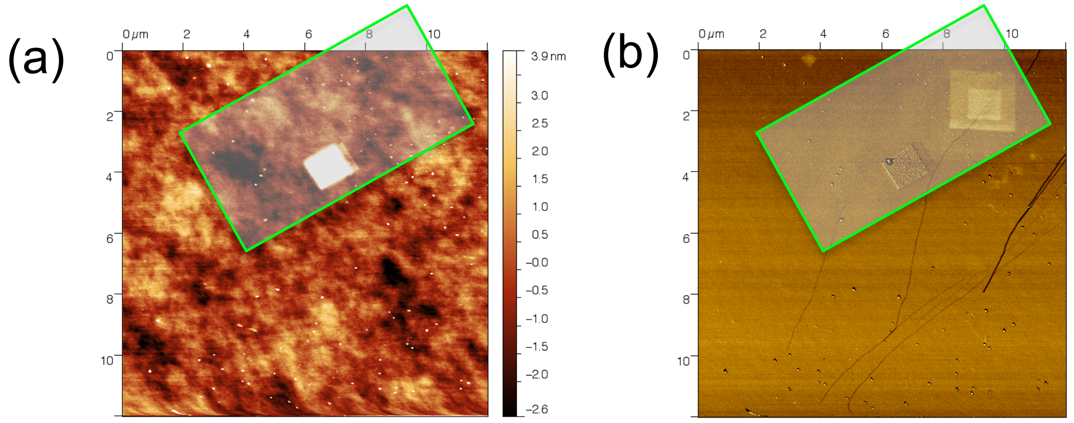

**Figure 4-17: Preservation of Ge on the surface after etching occurs in areas following AFM by a diamond like carbon tip. The two AFM micrographs are of the 700 ions/site pattern in (a) height mode, and (b) phase mode. There is evidence of morphological change after AFM and after Ge etching. In (a) the surface is clearly height modulated, whereas in (b) the phase information shows there is surface is affected in more than on area. The pattern is outlined in green for clarity.**

## 4.9 Why do QDs form on the crowns?

There are numerous studies to suggest that isolated pits in a surface are the preferred nucleation site for Ge QDs on a Si (001) substrate. Grydlik et al. [20] demonstrated that Ge will form monodispersed QD arrays provided that the wetting layer is carefully controlled, that the growth temperature is sufficiently high, and that deposition rates are sufficiently slow to allow for high enough diffusion lengths that exceed the pattern spacing. The growth temperature of 600 °C and deposition rate of 0.05 Å/s, lead to diffusion lengths of 10 μm. The relatively high temperature leads to a fair amount of intermixing too. The group has created arrays with pitch spacing varying between 350 and 3400 nm. Other factors, including pit shape and sidewall angle influence the QD growth.

In related work, Vastola [77] investigated the affect of pit sidewall inclination on the preferred nucleation site by comparing the elastic energy density of Ge wetting layer in a pit vs. the elastic energy density of the wetting layer on a planar surface. He found that as the pit sidewall increases relative to the substrate surface, the elastic energy density of the Ge decreases, at least until a sidewall angle of 20°. After that, the elastic energy density increases with increasing angle, until after 40°, where QDs prefer nucleation on the outside edge of the pit. He also notes that the elastic energy density of the wetting layer is lower for a steeper sidewall angle and negligible for small angles.

Small pitch lithographic patterns have been created using EUV lithography, [7,74] where small pits are formed with RIE, and modified with a low temperature buffer. The pits for their 90 nm pitch patterns were small, 12 nm across and 3-4 nm deep, whereas the QDs grown had a diameter of 35 nm. The QDs still nucleated at the pit despite the overfilling of the pit.

Portavoce et al. used Ga+ FIB to produce pits (7000 ions/site) in a Si (001) substrate. [25] After a controlled annealing, (1 min at 550 °C) the surface topography (i.e. pits) nucleating the QDs was small: 10 nm across with a depth of only 1 nm. QDs with a lateral dimension of 20 nm are formed at a sub-critical thickness with a CVD growth at 550 °C. Pascale et al. also used ex-situ Ga+ FIB to create pattern templates. They were able to create mono-dispersed arrays in their arrays at low temperature (400 °C), but at high temperatures QDs formed in the spaces in between the patterns.

We have created highly dense, ordered arrays of QDs, but despite the preponderance of studies that QDs want to form in pits, our QDs seem to be forming on in one case peaks, and in another the crowns of our patterns, i.e. places in the pattern with positive curvature. Our sidewalls, between 10° - 25°, fall within the prescribed limits for pit nucleation. Our "pits" do however differ in some key respects. First, they are not isolated pits in a planar surface. The two samples presented in TEM are dramatically different. The first shows a surface that has evolved into peaks on a surface. The peaks are small with sidewall angles close to the {105} facet angle (11.4°). The second is a sinusoidal, continuously modulated surface, also showing sidewall angles close to the {105} facet. Finally, our patterns are at a much smaller length scale than the typical report. Behavior on our patterns may be greatly impacted by our pattern length being much closer to the intrinsic length scale of Ge heteroepitaxy.

Two theoretical studies have proposed that crown nucleation is favorable to pit nucleation under certain conditions. The first is a 2D solution for the elastic energy for the nucleation of Ge islands on a patterned surface. [17] They have a simple saw tooth model where they look at nucleation on the apex, sidewall, and the valley: strain relaxation is accomplished through variation in the film thickness, when surface energy is *isotropic* islands will nucleate first in the valley where the critical size and energy are lowest. However, for sufficiently high surface energy anisotropy, e.g. a surface with high curvature, the nucleation barriers for valleys and apexes disappear. Notably, this can lead to nucleation of QDs with smaller critical sizes. Given that the two cases are degenerate, it explains why nucleation may occur on the apex, but not why it does.

The second model is a continuum model that considers the Asaro-Tiller-Grinfeld (ATG) instability modes of strained films on 2D "egg carton" patterns. The model tracks diffusional flow in response to the local surface chemical potential, accounting for elastic relaxation, anisotropy, and wetting. [101] A phase space (Fig. 4-18) predicts the localization of islands, e.g. top, bottom, disorder, etc., based upon the film thickness and an instability ratio $\lambda_n/\lambda_{ATG}$ where $\lambda_n$ is the wavelength of the underlying pattern, and $\lambda_{\mathrm{ATG}}$ is the ATG instability wavelength. Localization on the top of the patterns is predicted for instability ratios between 1 – 3.

$$\lambda_{ATG} = 4\pi\gamma_w/3M\varepsilon^2 \qquad \textit{Equation 4-2}$$

where $\gamma_w$ is the Ge wetting layer surface energy : 61 meV/Å$^2$ , [102] and $M$ is the biaxial modulus of Ge with $\varepsilon$=0.04: 152 GPa . [33] For these values, $\lambda_{ATG}$ =17 nm, and $\lambda_n/\lambda_{ATG}$~ 3 at 50 nm. By matching our values to the kinetic phase diagram of Fig. 4-18, we should expect nucleation on the top, e.g., on the crowns of our patterns. This conclusion is being further tested in ongoing work in the Floro group.

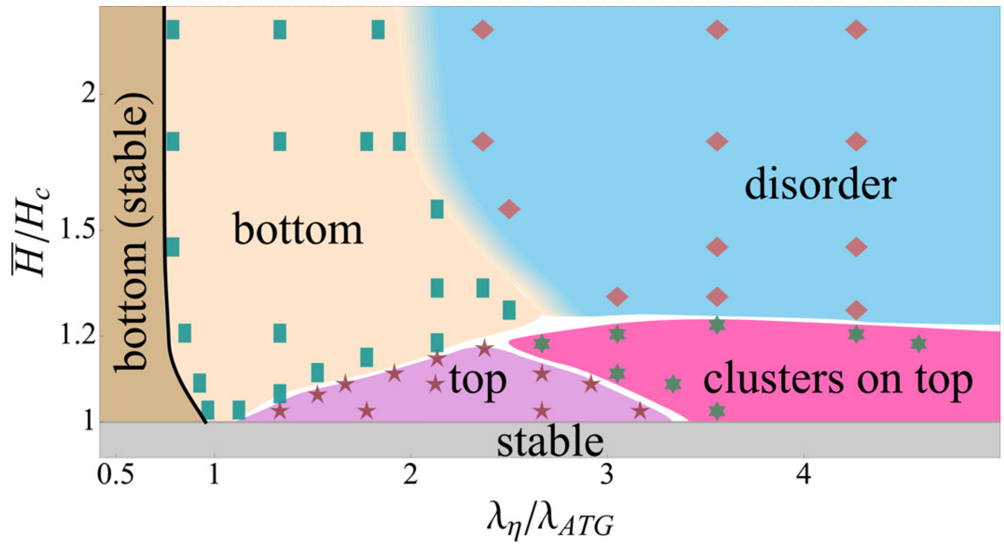

**Figure 4-18: Kinetic phase diagram predicting the localization of the quantum dots on a sinusoidal pattern as a function of the pattern instability ratio $\lambda_n/\lambda_{ATG}$ and film thickness. $H/H_c$.** [103]

# 5 Key Challenges in the Directed Self-Assembly using FIB

We have demonstrated the ability to produce well ordered 2D QD arrays at interdot distances of 50 nm using FIB to create a template to direct the nucleation sites. The 50 nm spacing is closer than previously achieved using FIB-based patterning. To produce a QDMC requires replicating the seed layer in the third dimension. Three dimensional ordering been accomplished on randomly nucleated, unpatterned substrates to create vertical chains of QDs, [3,57] as well as lithographically-produced ordered patterns, [7,74,104] most recently at 35 nm interdot distance. [7] This occurs by alternately growing Ge layers to form S-K QDs, and then depositing a Si "interlayer", which can at least partially replanarize. The whole process can then be repeated multiple times to build up the QDMC, where each successive layer of Ge dots should align with the underlying layers. These Si interlayers have inhomogeneous strain fields that direct the aligned nucleation of new quantum dots. Through careful control of growth temperature, Ge layer thickness, Si interlayer thickness, and deposition rate, replication of the seed layer is possible. For FIB patterned substrates at 50 nm, the challenge of extending growth in the third dimension is made more difficult by the formation of dome-like QDs and their tendency to form on the positive features of our patterns, which amplifies morphological features in our surfaces and may lead to pattern breakdown.

In this chapter we discuss our attempts at growing multi-layer crystals, and the natural progression from morphologically-driven nucleation to strain-based nucleation (i.e., heterogeneous strain in Si interlayers due to buried stressors), and the special challenges we faced. We will discuss the formation of voids that form near the interface for long growths, and inconsistencies within the patterned samples, that raise questions concerning the repeatability of patterns from pit to pit, as well as pattern to pattern. We will discuss how reducing the interdot distance to 50 nm creates issues, especially when using FIB-based patterning at typical ion energies of 30kV.

## 5.1 QDMC Growth

In discussing the various QDMCs we've grown, a few parameters are of main importance. Unless otherwise noted, the lateral pattern pitch (periodicity) will be 50 nm. We will use the following nomenclature to describe the QDMCs: N(Ge-$h_{Ge}$ /Si-$h_{Si}$ ). The individual Ge layer thicknesses are given by $h_{Ge}$, *in units of (004) Ge monolayers*, while the individual Si layer thicknesses are given by $h_{Si}$ *in units of nanometers*. N is the number of Ge/Si bilayer repeats – note, however, that while N will be an integer, *we usually do not grow the last layer of Si*, in order to allow us to perform AFM on the final Ge layer in order to assess QD morphology and patterning. For example, 5(Ge-8/Si-6) contains 5 layers of Ge each being 8 ML thick, separated by 4 layers of Si, each being 6 nm thick.

We were able to grow QDMCs containing local regions with ordering, with up to 5 repeat layers of Ge, see Figure 5-1(a), although this was only revealed with TEM. According to AFM, we were able to maintain a high degree of pattern order for growths with 2 or 3 repeat layers of Ge (figures 5-1(b) and (c)), which are morphologically similar to the monolayer QDs we have presented. However, as the number of layers in the QDMC is increased, there is a corresponding decrease in pattern fidelity as seen in AFM (Figure 5-1 (d)). A thorough understanding of what is causing the deterioration of the pattern required cross-section TEM.

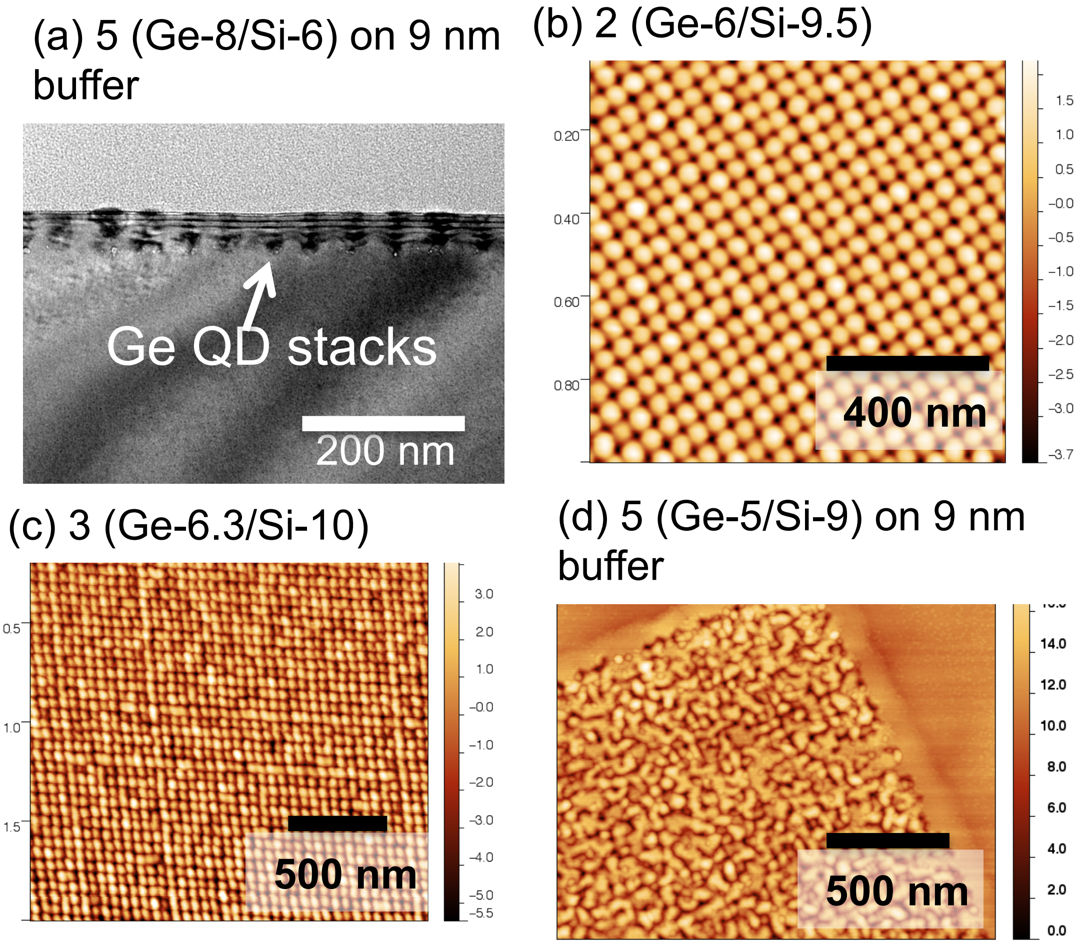

**Figure 5-1: Multilayer Ge QD growths. (a) TEM of a 5(Ge-8/Si-6), on a 9 nm buffer; (b)-(d) QDMCs of increasing layers (b) 2(Ge-6/Si-9.5): (c) 3(Ge-6.3/Si-10) ; (d) 6(Ge-5/Si-9), on a 9 nm Si buffer layer.**

Close examination of the pattern in figure 5-2 (a) shows coalescence Ge across of a number of pattern unit cells; a partial re-planarization is occurring. QDs are forming in the pit features in the surface with occupancy < 100%, however, the underlying periodicity is still evident. In figure 5-2 (b), we have a bi-layer sample where coalescence of Ge along one direction of the pattern has occurred (this is not believed to be an AFM artifact). However, cross-sectional STEM reveals a much different morphology than would be assumed from facile interpretation of the AFM micrograph. First, most of the QD-like morphology actually arises from the Si substrate. Classic Ge QDs are not observed – instead the Ge forms a partially conformal film, with some net aggregation at the crowns of the pattern, but there are also inverted Ge dots filling some pits. The Si interlayer actually seems to amplify the morphology, rather than smoothing it, which is odd. High-resolution TEM shows there is some residual extended defect formation in the pit bottoms, which would tend to repel Si, leading to a buildup on the crowns in this case. Nonetheless, the process is still epitaxial as confirmed in bright field TEM. It is clear that QDMC formation from our seed layers is not a straightforward endeavor. We have shown AFM evidence of ordered QDMCs to three layers, with on-crown QD formation, while we have also observed competition for Ge from pit features in subsequent layers. Attempts to re-planarize using the Si interlayers have not proven successful. The 6 nm Si in figure 5-2 (c) is growing in a conformal mode, or even slightly amplifying the corrugation. The balance required between Si interlayer thickness and re-planarization, while still maintaining a sufficiently strong strain field for this configuration is a challenge.

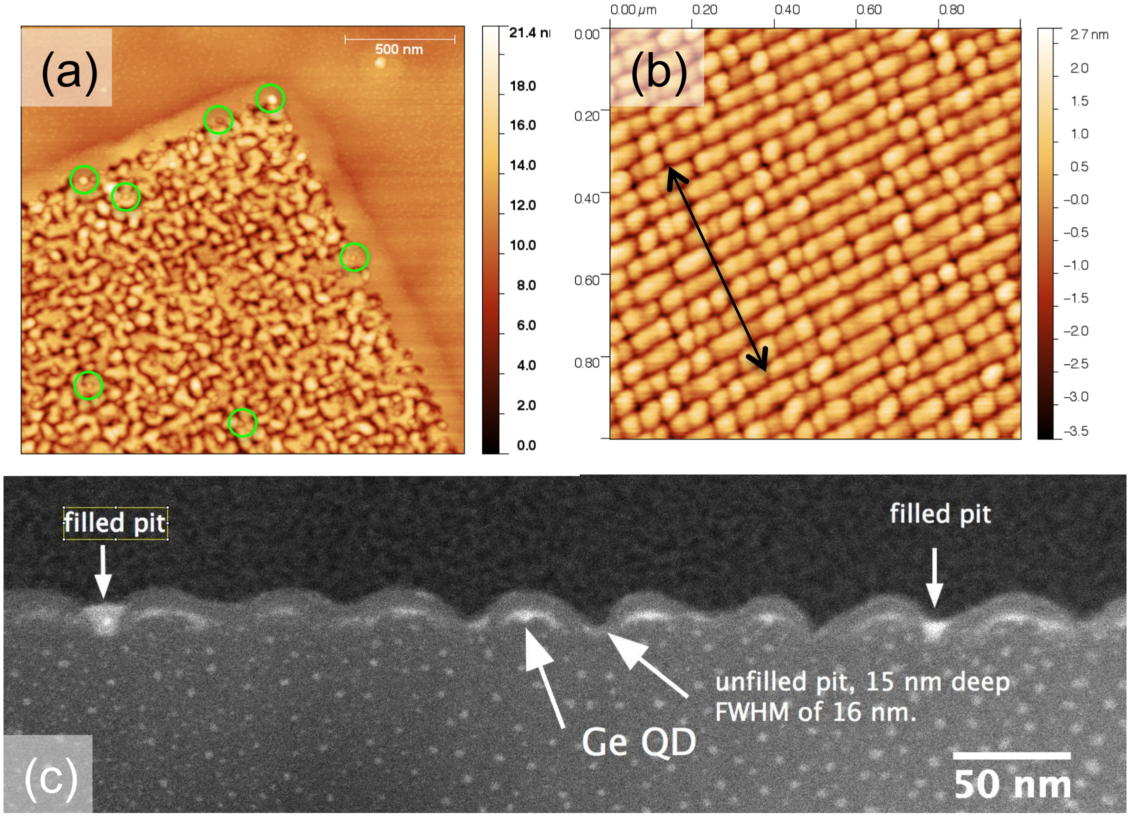

**Figure 5-2: (a) This is the same image as found in as Fig. 5-1(d), 6(Ge-5/Si-9) nm on a 9 nm Si buffer. Some QDs, circled in green, show Ge QDs forming on the top surface in pits. (b) 2(Ge-6/Si-6) on a 6 nm Si buffer. The arrow indicates the orientation of the STEM cross section shown in (c). The two Ge layers can be seen as bright features, but note that the small white dots in below the layers are metallic contamination from sample preparation.**

As mentioned at the beginning of the chapter, vertical alignment of QDs occurs due to an inhomogeneous strain field in the Si cap created by the buried Ge QDs. We can see aligned QD columns in Fig. 5.1 (a) with ordered Ge QDs on the top surface that positionally replicate the ordered Ge QDs on the first (seed) layer, although the morphology is irregular. We initially relied heavily on AFM characterization of the QDMC surface morphology, and from that hypothesized on crystal quality, and growth evolution mechanisms. However, when we finally obtained high quality FIB-liftouts and TEM cross-sectional imaging, we then developed a better view of how the layers of the

QDMC evolve. We were also forced to confront some unexpected inconsistencies in our patterning process.

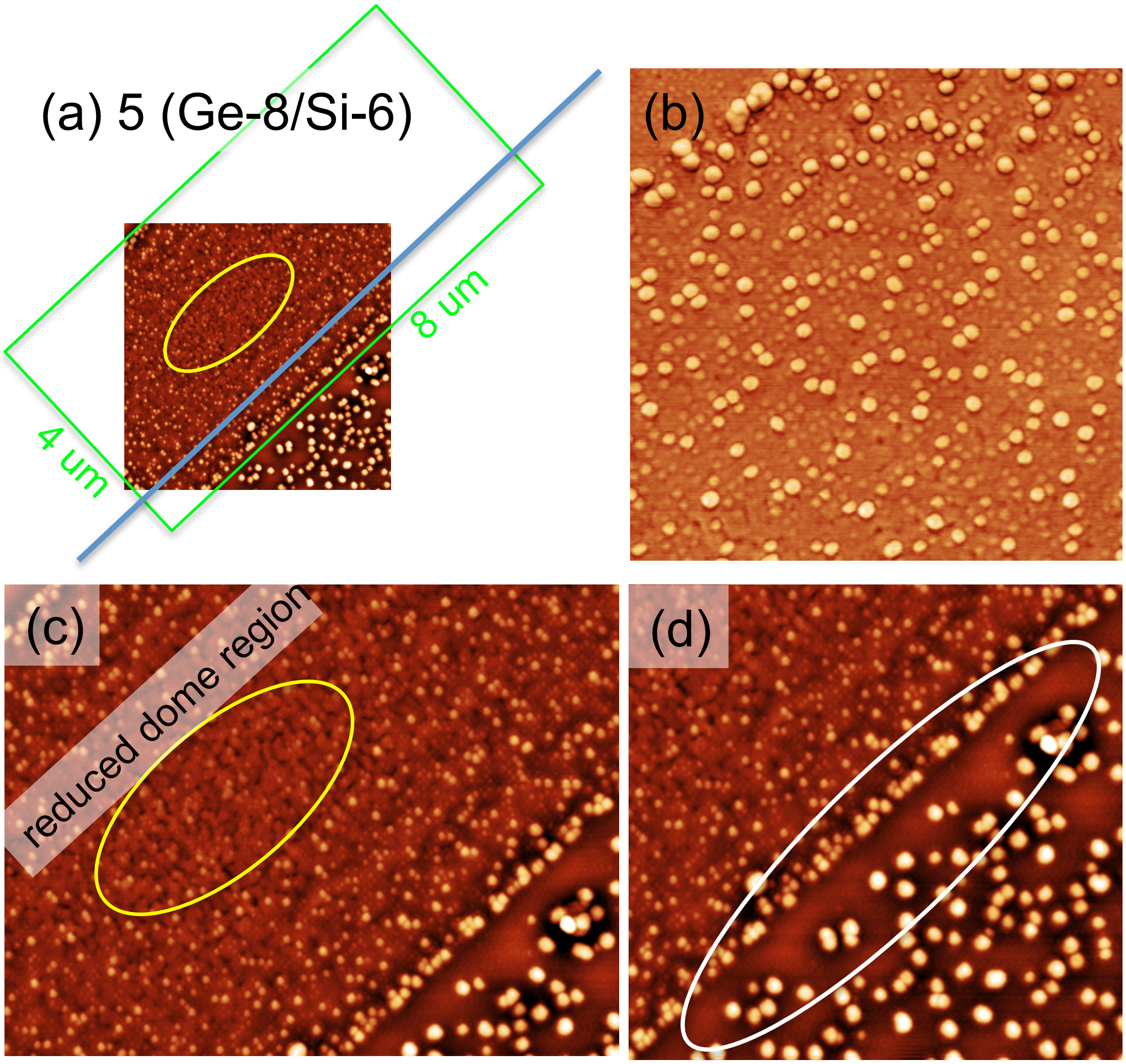

**Figure 5-3: 5(Ge-8/Si-6) on buffer QDMC shown in Fig. 5-1(a). (a) 5x5 µm AFM scan where the pattern is outlined in green, the blue line indicates the requested liftout location, the yellow ellipse indicates the region where fewer domes exist. (b) 3x3 AFM height scan near the upper edge of the pattern. (c) enlargement of the fewer dome region. (d) highlight of the denuded region next to the pattern.**

The 5(Ge-8/Si-6) QDMC, shown in Figure 5-3 (a) and (b) is intermittently covered with spatially ordered dome and hut shaped features, which suggests that alignment has propagated from the original interface through all nine layers of Ge and Si. This is the same sample as Fig. 5-1 (a), where a 9 nm Si buffer was deposited at 0.1Å/s at 450 °C. Then four alternating layers of 8 ML Ge, followed by 6 nm of Si were deposited at the same rate and temperature. There was a one minute interval between each step. Finally, 8 ML of Ge was deposited on the top surface, again at the same rate and temperature with a one minute anneal before quenching. According to XTEM, the Si interlayers in the sample shown in Fig. 5-1 (a) have mostly re-planarized. This implies that the ordering of the QDs is no longer driven primarily by surface morphology, but by the inhomogeneous strain field created by buried Ge QDs. There are a few pits in the sample indicating defects, and the reduced number of domes in the very center of the pattern in Fig. 5-3 (c) is notable, suggesting that diffusion is severely suppressed, especially given that 8 ML of Ge was deposited on the top surface. The edge of the pattern is covered with large domes which are acting as a Ge sink which leads to a denuded region adjacent to the pattern, where competition exists with the off pattern islands.

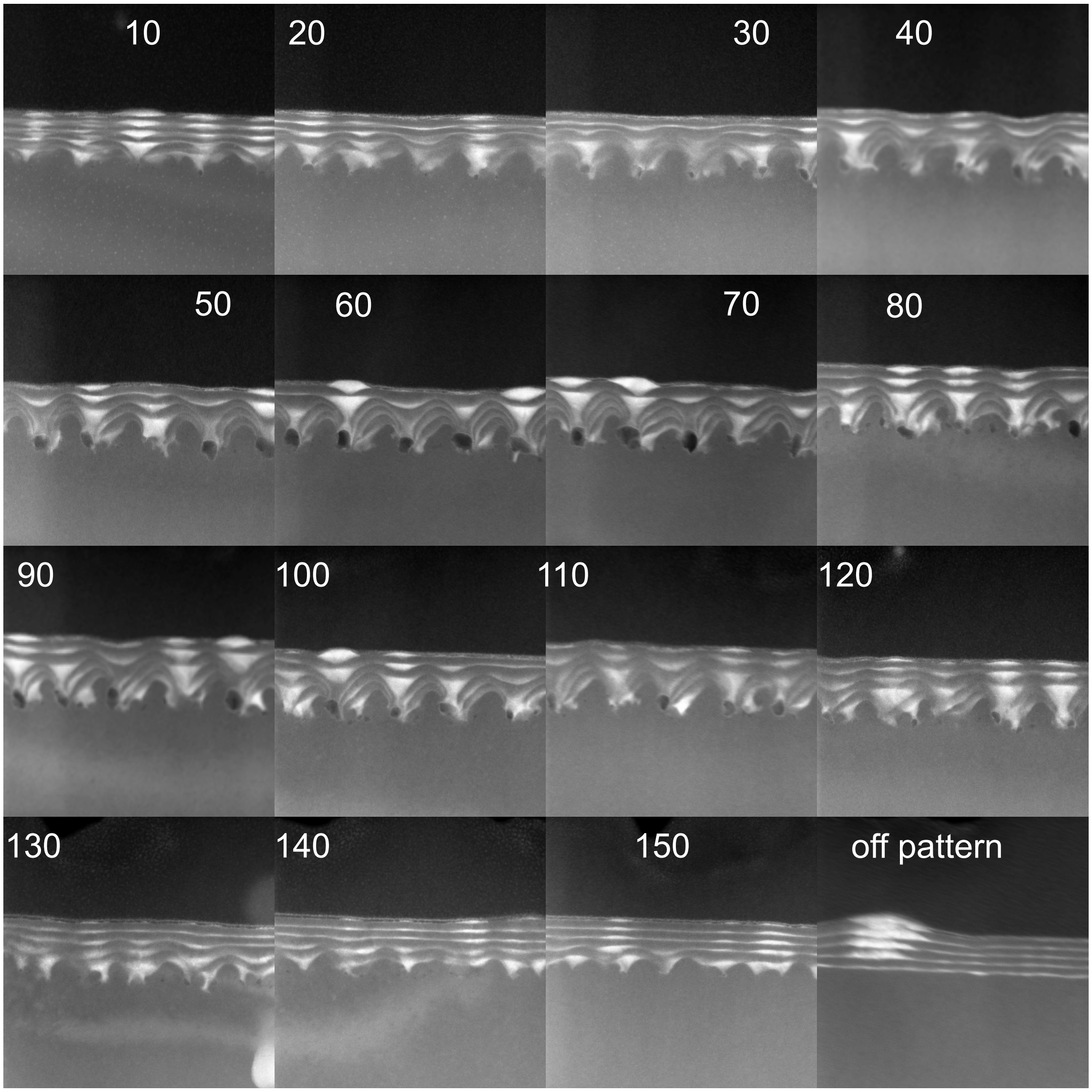

**Figure 5-4: STEM micrographs of a 5 (Ge-8/Si-6) QDMC. Every tenth dot is depicted here, to highlight the evolution of the pattern through the crystal.**

An extended TEM cross-section of the sample shown in Figs. 5-3 (a) was obtained, where the liftout was performed by Joshua Maier at Penn State University. We were able to obtain a completely contiguous, electron-transparent sample from one edge of the pattern to the other, a distance of 8.0 μm and 159 FIB sites. A sampling of the

HAADF-STEM images is presented in Fig. 5-4, where every 10th FIB site and QD is extracted. The sample is rich in features and will be discussed here in some detail.

Fig. 5-5 shows a close-up of the left edge of the patterned region. The first thing we observe is the well-formed stacks of QDs. The second thing we observe is that the first layer of QDs forms in the pits of the substrate corrugation, different than the behavior discussed in detail in Chapter 4. This may be due to the high curvature of the pit relative to the crown in between the pits. The interlayer of Si is measured at 5.8 nm (nominal 6.0nm). The first column of QDs at the lateral start of the pattern increase in size with each successive layer; this feature is corroborated by the AFM scans showing

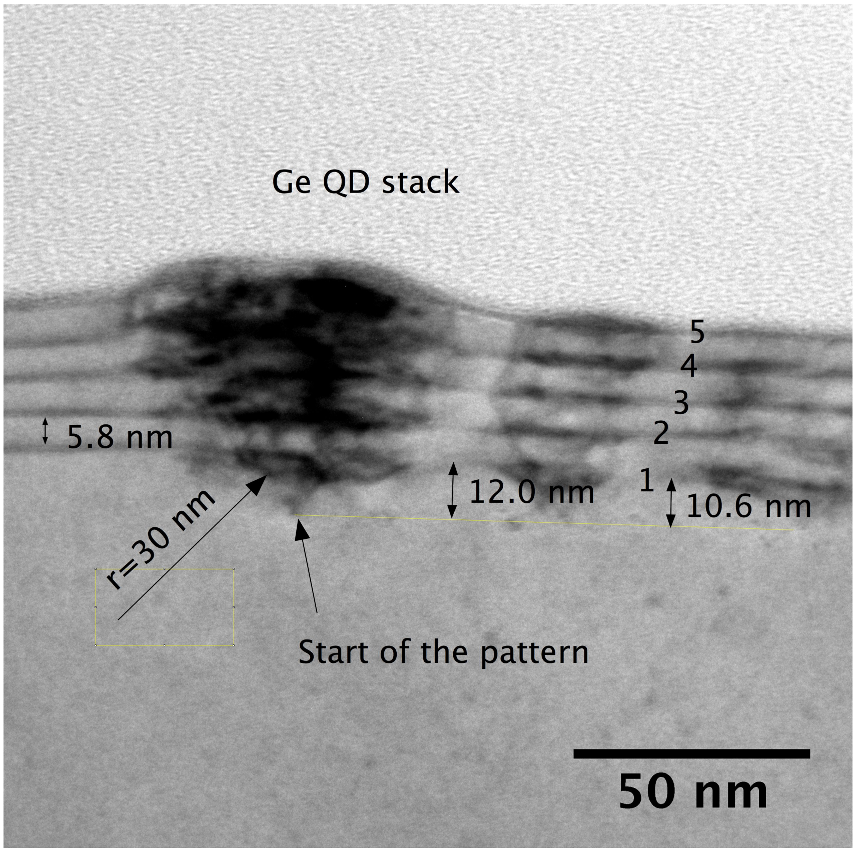

**Figure 5-5: Bright-field XTEM micrograph along a [110] zone axis. QDMC, 5 layers of 8 ML Ge deposited at 0.1 A/s at 450 °C. There is a 9 nm Si buffer and 4 interlayers of 6.0 nm deposited at the same conditions. This is the far left edge of the pattern in the contiguous XTEM cross section. (QD 1).**

coarsened QDs at the edge of the pattern. The Ge wetting layer is clearly visible in the superlattice to the left of the first column, and is apparent after it as well.

Further examination of the crystal (Figure 5-6) reveals the appearance of what we surmise are voids, based on their appearance in bright-field TEM and in HAADF STEM. They first appear as early as QD 2, and they are interspersed at a depth where the original buffer was deposited. The void at QD 11 in figure 5-6 has a diameter of 4.0 nm. Larger voids are found at dots 67 and 68 in Figure 5-7. The void at dot 67 is circled in green in each of the micrographs. The large dark objects in the bright field TEM are Ge QDs; they appear white in the STEM due to Z-constrast.

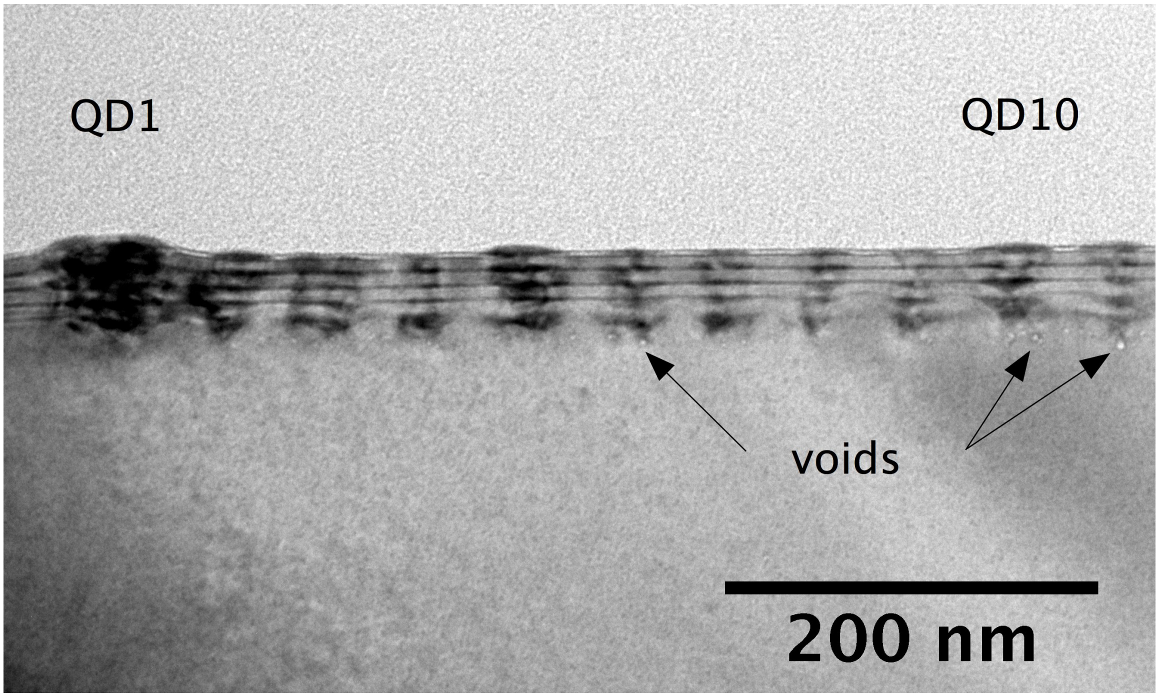

**Figure 5-6: Bright field XTEM, along a [110] zone axis. QDs 1-11, showing tiny voids appearing at base of the stack.**

From inspection of the contiguous X-STEM sample (see Fig. 5-4), the crystal remains well ordered through QD 25 where the voids start to increase in size and frequency. A clearly observable trend in Fig. 5-4 is the increase of size and frequency of the voids in the pattern toward the center of the array. Each void in the series of micrographs was identified and its volume approximated by measuring the height and width of the void. The volume was approximated by using the volume of an ellipsoid where $V=4/3\ \pi\ abc$, where $V$ is the volume, and $abc$ are the primary axes of the ellipsoid. We assumed $a=b$, since we only had the cross section of the void. The trends we described are clearly illustrated in Fig. 5-8.

A second observable trend is the increased disorder in the layers of the crystal. Towards the edges there is relatively laminar "flow" of the Si interlayer and regular formation of Ge QD vertical stacks. Proceeding into the pattern, as the layer morphology becomes more "turbulent", QD formation becomes irregular and stacks begin to appear only after a few layers of the crystal have already been deposited. Remarkably, however, given the extreme starting surface morphology of the substrate, after only a few layers the surface has replanarized, see Figs. 5-4 and 5-7.

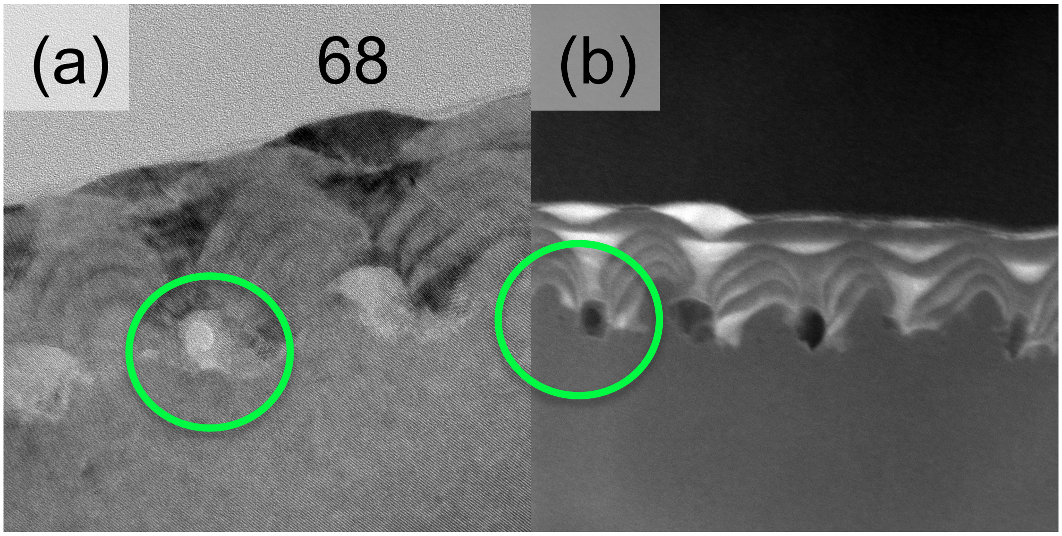

**Figure 5-7: QDs 67 and 68 shown both in (a) bright field TEM and (b) STEM. Void for QD 67 is circled in each of the micrographs.**

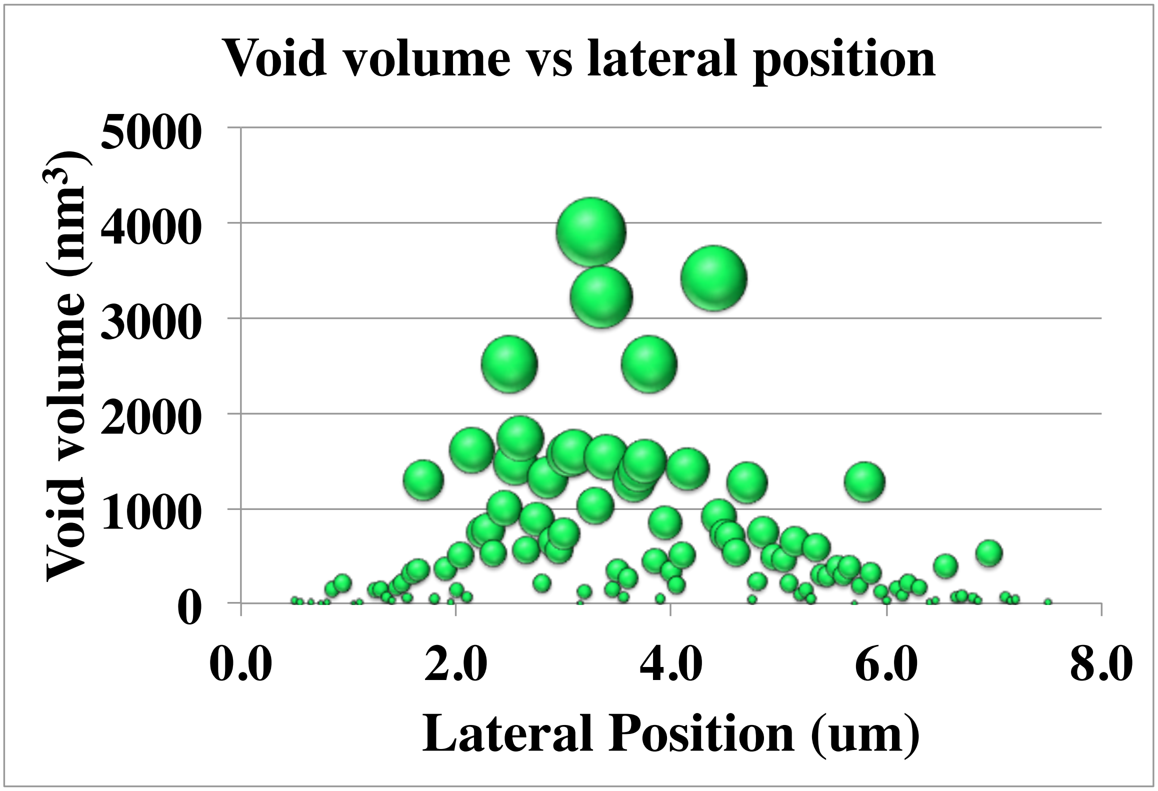

**Figure 5-8: Void volume vs. lateral position, the volume of each identified void was estimated and plotted in its position in the sample array. The size and location of the "bubble" is an indication of its estimated volume.**

One other interesting observation is that 86% of the voids are located left of the centerline of the pit and nestled on an undercut feature of the substrate. An example of the asymmetry is shown in Fig. 5-9. The centerline of the pit region, post buffer, is indicated in the figure. In all of the cases, Si and Ge deposition is visible to the right of the void (red arrows), whereas, there is no deposition to the left. Additionally, there is a deposition bias highlighted by the Ge wetting layers. The growth between the first and third Ge layers is indicated by black arrows on the left side of the substrate features and by blue arrows on the right. Finally, the post buffer morphology is extreme, i.e. steep sidewall angles, and pit regions larger than the substrate mounds in between.

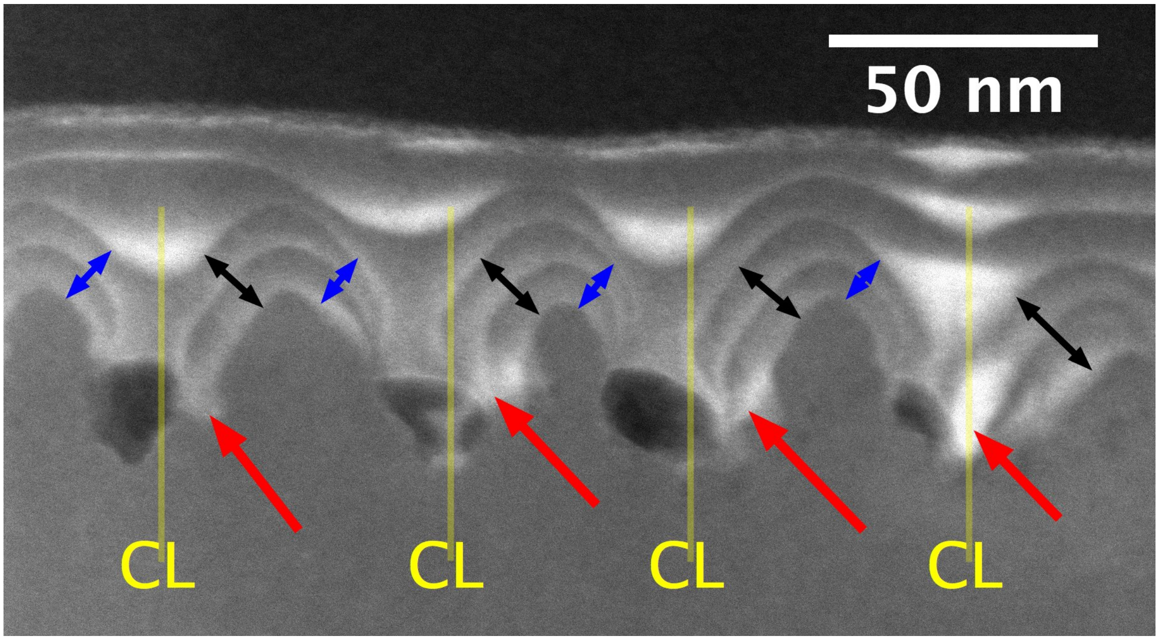

**Figure 5-9: Center region of 5-layer QDMC featuring asymmetrical void formation, Si deposition, and severe substrate morphology. Compare the lengths of the black arrows to the blue arrows to see the growth asymmetry (these arrows connect the 1st and 3rd Ge layers). The red arrows show accumulation of Si and Ge near the bottom of each original pit, always to the right of the voids.**

## 5.2 Void formation

Three theories as to the origins of the voids were considered. The first hypothesis was that the voids were the result of Ga clustering at the interface. However, the feature contrast in bright –field TEM (brighter than Si), and in STEM (darker than Si), suggests that these regions are lighter in effective mass than the surrounding Si. While we were able to confirm that Ga exists within our samples through the desorb process, i.e. the point of deposition (section 5-6), based on the TEM, (Fig. 5-7) Ga is an unlikely candidate as it has an atomic mass similar to Ge.

The second hypothesis that we considered was that the voids formed due to a supersaturation of vacancy defects during FIB implanting. We performed a volume analysis to determine if FIB induced defect (i.e. vacancy) creation could potentially be responsible. The total void volume was calculated as described in section 5-1, and the results are summarized in Table 5-1. We determined the total number of vacancies required to account the total void volume, and the same for the number of implanted Ga ions required to match the void volume. The equivalent number of vacancies is calculated by determining the number of missing diamond cubic Si atoms, using the bulk crystal lattice constant for Si (0.543 nm). The equivalent number of Ga ions was determined by using a Ga density of $\varrho$=6 g/cm$^3$, and atomic mass of 69.7 a.m.u. The number of implanted ions was calculated assuming a single row of patterned sites, i.e. 159 sites, multiplied the ion dose for this sample.

The population of voids is high and is concentrated in the center of the sample. The number of implanted ions is only a small fraction of the number of Ga atoms required to account for the volume. A sputtering yield of 2.4 ions/site [105] would not account for the volume either, however, a monte carlo simulation package (SRIM: stopping range of ions in matter) [106] estimates that a 30kV Ga ion will create roughly 300-1000 vacancies along its track. The software overestimates the retained defects because it ignores defect subsequent diffusion and recombination, [107] but as a rough calculation, retaining 27 vacancies/ion seems plausible.

## Table 5-1: Void Statistics

| **Void statistics** | | |
|---:|---:|:---|
| **Count** | 107 | **voids** |
| **Total Volume** | 60805 | **nm$^3$** |
| **<V>** | 568 | **nm$^3$** |
| **Std. dev** | 744 | **nm$^3$** |
| **MAX** | 3906 | **nm$^3$** |
| **MIN** | 5 | **nm$^3$** |
| **Lattice sites** | 3038307 | **eq. Si in lattice sites** |
| **Ga atoms** | 3152626 | **eq. Ga atoms** |
| **Implanted Ga ions** | 111300 | **159*700 ions/site** |
| **Required vacancies/ion** | 27.3 | |

Voids will nucleate to reduce the supersaturation energy of the vacancies, and the stored elastic energy, at the expense of increased surface energy. We have only seen extended void formation in one other sample, which happened to be a 6-layer QDMC. The multilayer samples require a much longer growth time than typical single or double layer growths. This particular sample took 1 hour. Hence we speculated that the longer growth times permit vacancy aggregation due to diffusion. However, using literature values for vacancy diffusion in Si: $D=1.3 \times 10^{-6}$ cm$^2$s$^{-1}$, for $D_o=2.5 \times 10^{-3}$ cm$^2$s$^{-1}$ and $E_m=0.47$ eV at 723 K. [108] we obtain a diffusion length of $x=\sqrt{Dt}$ = 600 μm for t=3600s. There is adequate diffusion length for the vacancies to get anywhere within the patterned region, but the extremely high diffusivity also means that *the long time of a multilayer crystal is not required for voids to form*. Furthermore, the variation in void size over about 1.5 μm from the edges of the pattern (see Fig. 5-8) is inconsistent with such a large diffusion length, which greatly exceeds all pattern dimensions. Hence this calls into question the vacancy aggregation model, unless the effective diffusivity is much lower in our samples, e.g., due to interactions with other residual implantation defects.

A third possible model for void formation is the anisotropic overgrowth of Si and Ge leading to “pinch-off” to form the void. Three trends are consistently observed in the XSTEM montage (Fig. 5-10): at the edges of the patterned region, the QDs are well ordered and aligned, there aren’t any voids, and the height modulation of the surface is in the 10-15 nm range (modest). By contrast, in the middle of the pattern, the crystal is not well ordered, there is a nearly one to one ratio of (large) voids to sites, and the substrate surface height modulation is much greater, 15-30 nm.

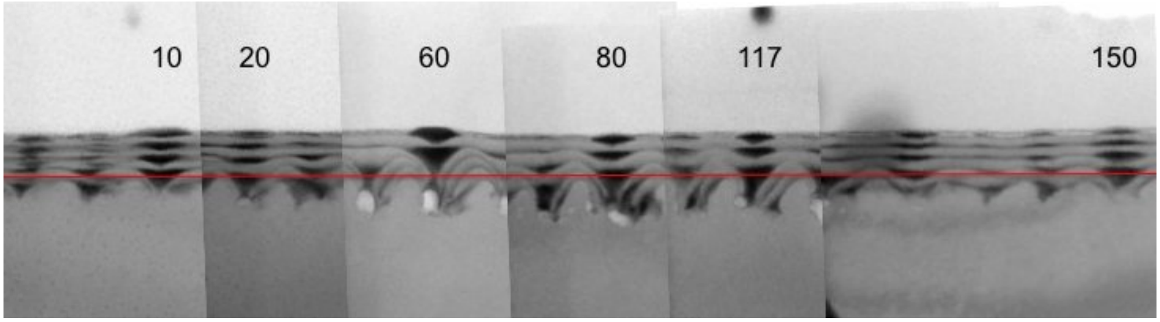

**Figure 5-10: STEM cross section montage of individual micrographs across the sample. Individual dots are identified for position correlation. Dots 10 (500 nm from the edge) and 20 (1 µm from the edge) are typical for the QD structures near the left edge. Closer to the center dots 60 (3 µm form the edge), dot 80 (at center), and 117 (3 µm from the right edge) are typical for the center region, with larger voids. And finally dot 150 (500 nm from the right edge) is in a nearly void free region. The HAADF-STEM images have been inverted (Ge is dark, voids are light).**

In order to explain this, we need to invoke some form of “pinning”, where the local growth rate is held at zero, or equivalently, an avoidance of the patterned pit minima by the Si adatoms. When the 9 nm thick Si buffer layer is deposited, the flux on the quasi-sinusoidal surface is asymmetric, because the Si deposition source was parallel to the row of dots in Figs. 5-4 and 5-10, and angled 30° from normal (Fig. 5-11). Local avoidance of the Si growth near the bottom of a pit then creates an extreme morphology, as shown in Figure 5-12, with fast vertical growth, and an overhang on the left side of each surface maximum. Self-shadowing of the flux exacerbates the morphology, and as the backside growth increases, so does the shadowing effect. Eventually the growth front of one feature (B) connects with the backside of an adjacent site (A) at a "pinch-off point", thus forming an enclosed void. After the pinch point is formed subsequent layers are unaffected by the pinning and shadowing and so growth proceeds in a more laminar mode. However, the upper surface of the void itself may round off to reduce local curvature, mediated by internal surface diffusion.

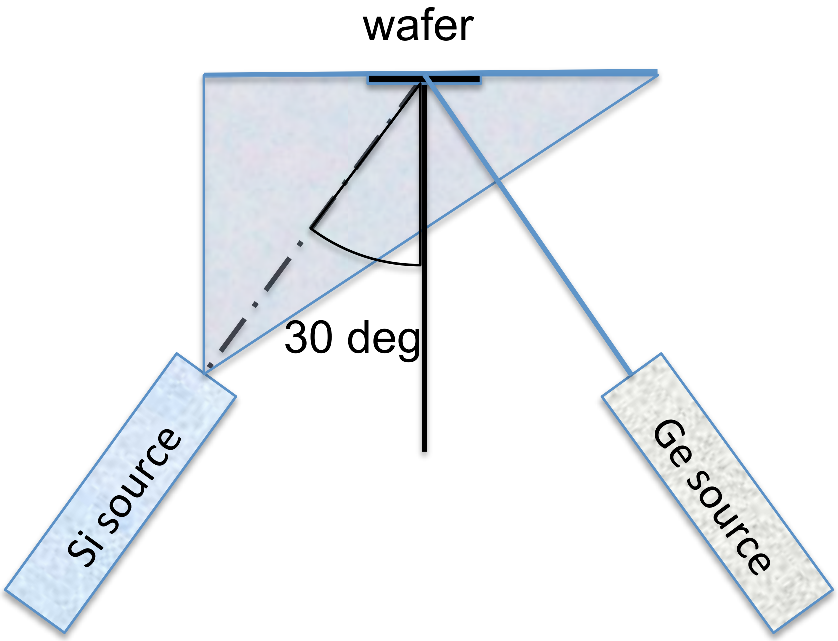

**Figure 5-11: Orientation of Si and Ge guns in MBE chamber in relation to substrate during deposition.**

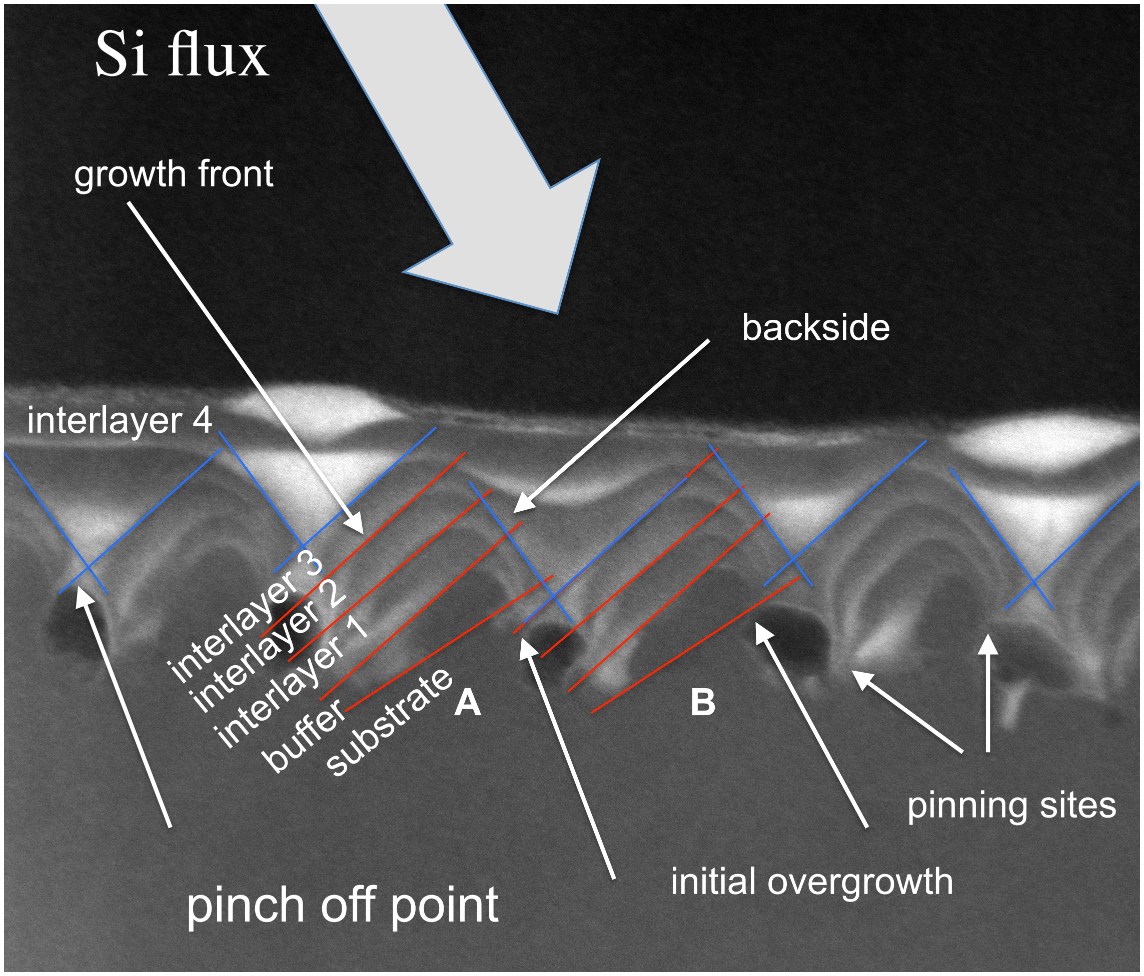

**Figure 5-12: Growth fronts in the 5-layer QDMC (red) . The orientation of the Si gun is indicated. The initial Si growth is pinned at pinning sites at each of the features. The orientation of the Si gun leads to asymmetry in the growth, and an overgrowth which forms on the backside of the feature shades the region which eventually becomes a void. The primary growth fronts for each interlayer are indicated for features A snd B. Pinch points (in blue) are created by intersecting the backside and growth fronts of adjacent features at the last layer of pinning.**

Voids do not form at sites where pinning doesn't occur. Sites where only one layer pins, or where the local avoidance of the pit minimum is very small, will have very small voids. It is uncertain why the pinning occurs in some of the sites, and not in others. Avoidance of the pit bottom by the Si buffer could result from retained defectivity (point defects or Ga, since TEM does not indicate any extended defects). The decrease in void volume from center to edge of the pattern correlation to pattern site could suggest that Ga impurities could be locally diffusing out of the patterned region.

It is also unclear why the Ge isn't suffering from the same shading effect as Si, as the Ge source is in line with, but opposite of the Si source (Fig. 5-12). Note, however, that there is often an accumulation of Ge on the lower right side of the pit, exactly where we would NOT expect it to form by line-of-sight deposition considerations alone – see Figs. 5-9 and 5-12. Ge may be more mobile than Si, and perhaps less subject to whatever is causing pinning. Furthermore, only 1.2 nm of Ge has been deposited in each layer, so a variation in thickness, at least in the wetting layer is harder to detect.

Finally, the QDMC is able to recover and replanarize when the two fronts fill the gap in between two features. The Ge layers of the 5-layer QDMC are highlighted in Fig. 5-13, illustrating the evolution of the substrate morphology with each successive layer. It becomes clear how, from a continuously modulated surface, due to pinning and the avoidance of pit bottoms, extreme surface morphology can evolve, re-creating dome like structures. Following deposition of enough material to bridge the gap between adjacent structures (in this case three layers), replanarization of the surface occurs, creating QD arrays from additional Ge deposition. (Fig. 5-1)

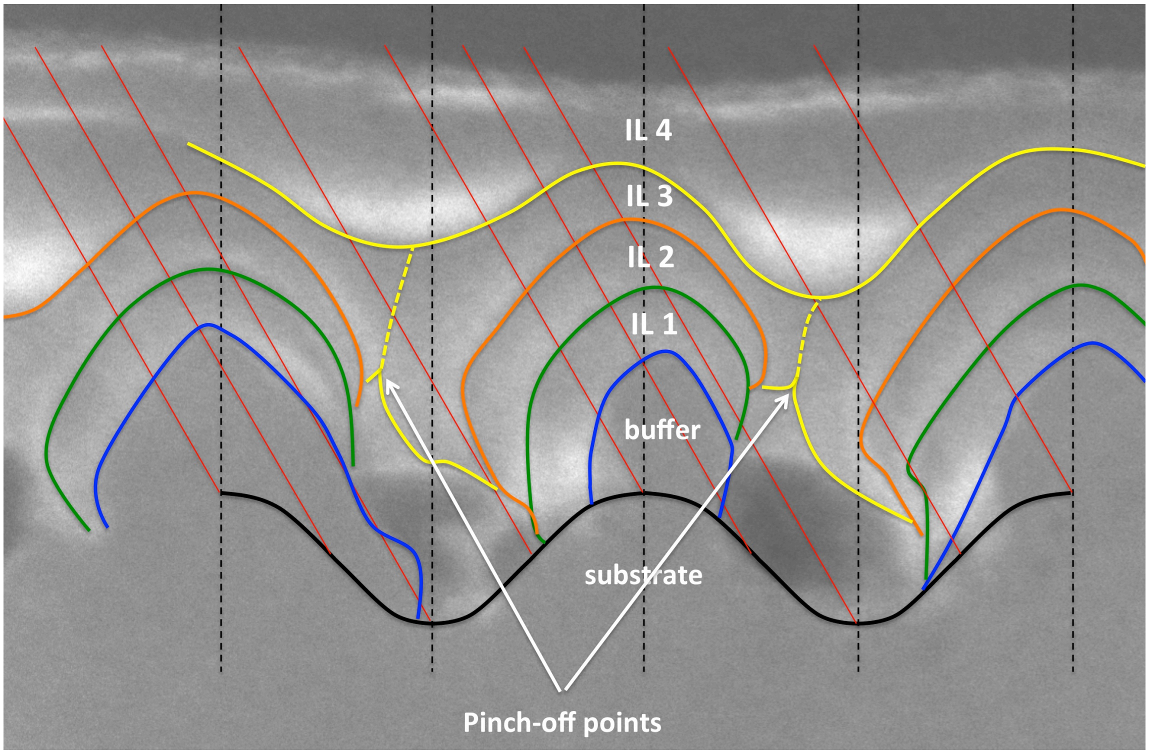

**Figure 5-13: Traces of the Ge layers in the 5-layer QDMC. The shape of the substrate is purely speculative, based on the form of the voids and identification of original pinning sites.**

## 5.3 Process variability

We have been able to produce arrays of QDs with reasonably narrow distribution widths, and typically for any experiment we will get an optimal result for some ion dose, since each sample has a wide experimental range for each parameter, e.g. dose varying between 700 and 20K ions/site, pitch varying between 20 – 100 nm, etc. This was by design, giving us the opportunity to evaluate the process space with respect to both dose and spacing, while keeping the focus condition of the FIB, the wet chemical etch, the exposure, the desorb process, the growth temperature, and the deposition flux all the same. Despite all that, subtle differences can lead to variations even within a single pattern as we've just discussed, but there are differences that manifest themselves from pattern array to pattern array as well.

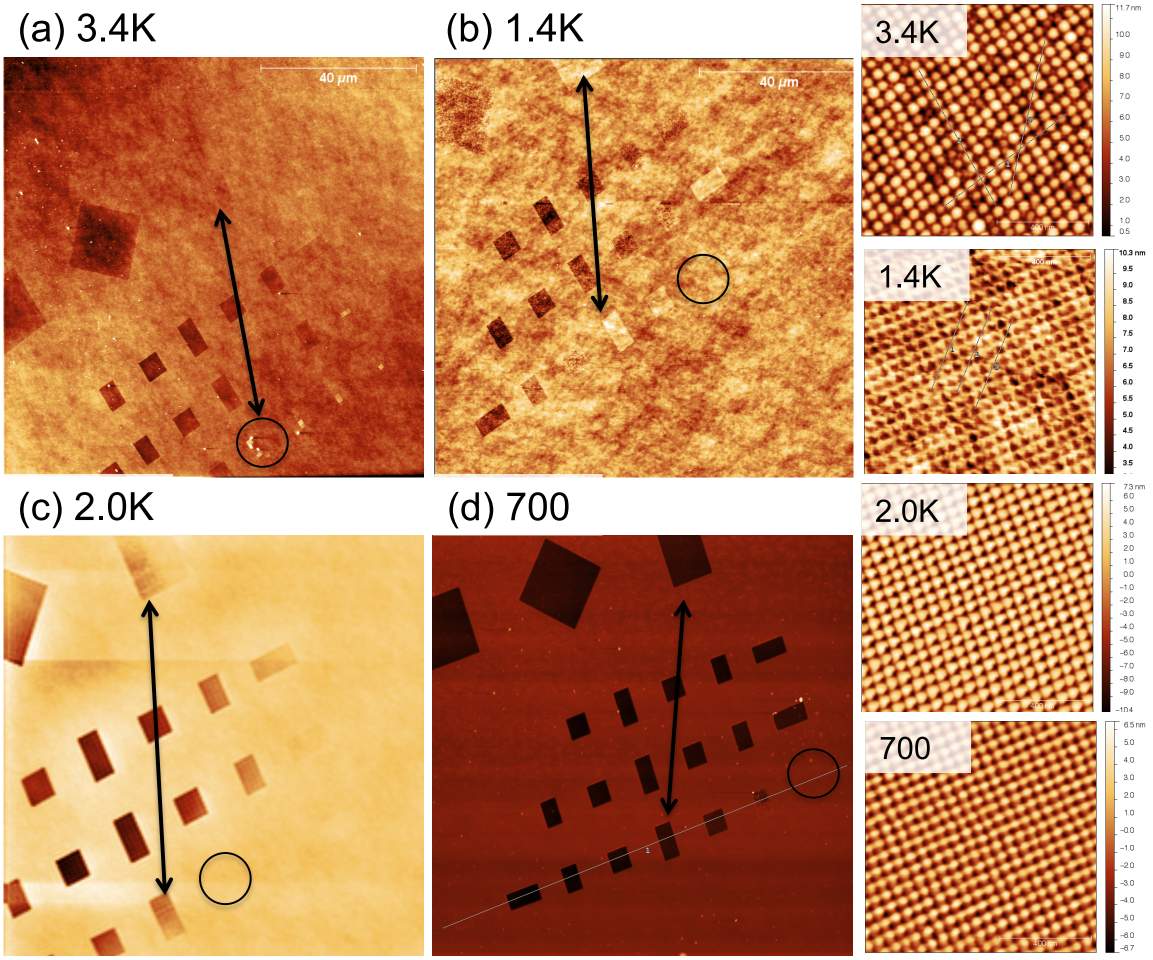

**Figure 5-14: A comparison of four 110 µm x110 µm AFM macro-scans identically patterned wafers, all patterned the same day, highlighting significant differences in patterns with the same nominal dose. The double-ended arrow shows arrays with 3.4K ions/site and 50 nm pitch, in a large-area pattern (top of the arrow) and a small-area pattern (bottom of the arrow). Circle regions are where the best pattern is retained. The corresponding scans on the right correspond to the "best pattern" for each array.**

Sometimes, in particular for pitches of 50 nm and less, when the ion doses get too high, the entire pattern can be etched away, and the pattern surface is offset below the unpatterned substrate surface, measuring in the tens of nanometers. Figure 5-14 shows a comparison of four patterned Si wafers. All the Si wafers were patterned on the same day, and processed in the same manner with the exception of the particular MBE growth parameters used in each case. The AFM macro-scans image 110 µm x 110 µm regions; darker features correspond to deeper features. When a patterned region appears to be sharp and dark, it implies that there is a very deep surface offset in the patterned region after wet chemical etching. The black circles on the macro AFM images show the region from where the "best pattern" is retained. Typically you cannot see this modulation in the macro AFM: first, the contrast is dominated by the largest features which are often the deep-etched patterns. Second, for a 110 µm x 110 µm scan with a 512 x 512 pixel array, the distance between scan points is 215 nm. Since our pitch is 50 nm, it cannot be correctly imaged. We do occasionally see aliasing in intermediate size patterns.

The arrows in Fig. 5-14 are positioned to show the 3.4K ions/site pattern in the first row (towards the bottom of each scan) and the 3.4K ions/site large area array (at the top of the scan.) In the first sample (a) 3.4K , where that dose is the best pattern, the patterns are not visible, meaning there is no resolved vertical offset in the pattern height. By comparison, the last sample (d) 700, both patterns show high contrast, meaning they have heavily etched below the substrate surface. As a result, the best pattern is found at a lesser dose, 700 ions/site. These extreme differences are concerning, and we believe they do NOT correlate with the MBE growth conditions, but must arise from processing steps (FIB patterning itself, or the wet chemical etch) prior to growth.

There are essentially three components to our clean. The first two, IMEC and RCA-2, are oxidizers, and each creates ultrathin oxides, i.e. < 10Å, for the exposures to which our samples are subjected. [109–111] The etching process works by complementing the oxidation with removal of the oxide using dilute HF (5%). Si is an etch stop for HF, so the material removal is limited to the ultrathin oxide created by the IMEC or RCA-2. It is fortuitous that FIB patterning creates defects that enables penetration of the chemicals into, and preferential etching of, defective sites. In the case, where patterns etch at depths of tens of nanometers, however, the chemicals are essentially self limiting and can't alone account for the removal of such a huge amount of material; there must exist some other mechanism that enable the chemicals to remove the material, namely defects.

The other possible source of non-repeatability is the FIB process. FIB patterning is highly automated, creating arrays of thousands of FIB sites with a prescribed dose, controlled through sophisticated control electronics. The primary difference in one patterning run vs. another, is the focus condition of the FIB. Focusing is a highly subjective process. We've tried to reduce the variability through focusing at extremely high magnifications, namely 150 kX. One aspect of focusing that can be difficult to correct is astigmatism, (Fig. 2-3). We verify roundness of our focus spot through the creation of a fiducial pattern after we reach "ideal" which is the best we can do at that time. Beam defocusing is intentionally done to limit exposure damage to surfaces that are being polished, e.g. TEM liftout samples, but these are instances where exposure is for a prolonged period of time, i.e. seconds. While it is expected that near surface morphology will be affected by a broader, less focused beam, it is not certain that the cascades below the surface will change much.

## 5.4 FIB challenges at reduced lengthscales

The combination of FIB at 30 keV and wet chemical etch has allowed us to create pit patterned arrays at ion doses much lower than previously reported, which is fortunate because it has allowed us to pattern at much lower lengthscales, i.e. 50 nm and below. As described in chapter 2, Ga ions from the FIB impact the Si substrate and sputter some atoms while displaces others within the substrate as point defects (Frenkel pairs), and the collision cascade evolves until all of the incident kinetic energy is dissipated. The number of defects produced is related to the number of implanted ions, i.e. dose. The projected range of the collision cascade is largely dependent on the ion energy. Higher energy atoms will penetrate deeper and will displace larger numbers of atoms.

We have used the software package SRIM (Stopping Range of Ions in Matter) to gain an understanding of the impact that dose and energy have on the projected ranges and the cascade volume. In Figure 5-15, we modeled a 30keV Ga beam into a Si substrate at normal incidence and modeled for doses of 1K, 10K, and 100K ions. The trace of each ion as generated by the monte carlo simulation is traced. The boxes are each 100 nm across and deep. It should be noted that the model records each ion as an isolated event and the results are summed, i.e. there are no interactions between cascades, or self-healing.

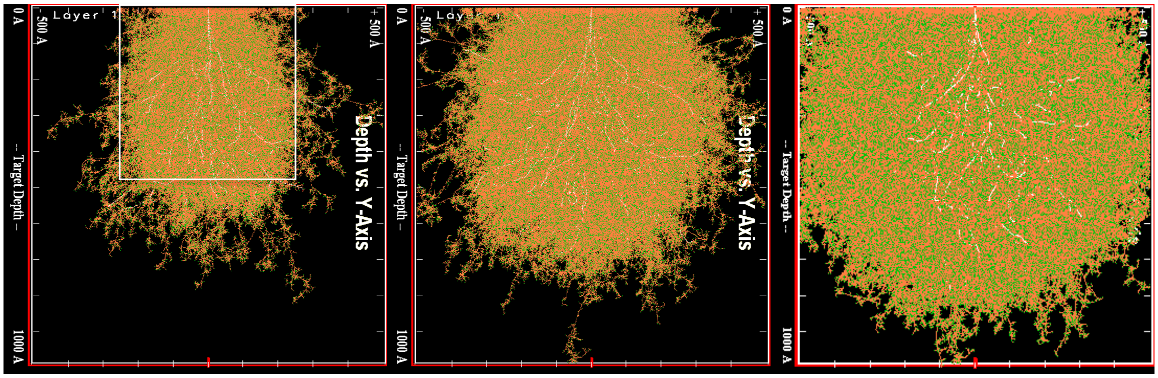

1 K ions/site 10 K ions/site 100 K ions/site

**Figure 5-15: SRIM recoil traces for a 30 keV Ga beam in Si for doses of 1K, 10K, and 100K. The white box in the first image is 50 nm across, and the other images are on the same scale.**

For doses at 1K ions and 10K ions there is virtually no recoil events outside of the 100 nm box which means that for a pattern spaced at 100 nm there would likely be no interactions between the adjacent sites. Even at 100K ions, while some recoil events occur outside of the box they are relatively small in number and would likely not have any impact. When the pattern sizes shrink to 50 nm (and smaller) the 30 keV ions have sufficient energy for adjacent FIB sites to interact through overlap in the cascades.

The number of recoils, i.e. defects, is not symmetrically distributed in depth. In figure 5-16 the depth distribution of Si recoils is juxtaposed with the 1K ion recoil plot. We can see at the green arrow, where the highest density of recoil events occurs in depth, is only about 20 nm below the substrate surface, although recoils occur as far as 80 nm below the surface.

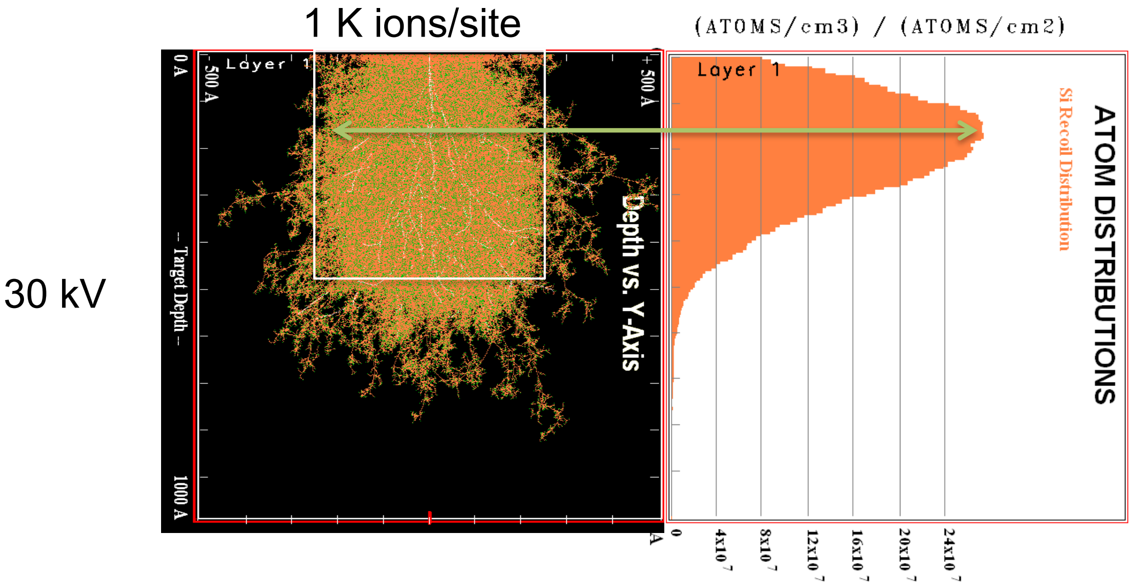

**Figure 5-16: Recoil distribution at 1K ions, and the recoil distribution at depth.**

What this suggests is that we are able to pattern at 50 nm as long as we are mindful of dose. Excessive dose results in the macroscopic pattern etching shown in figure 5-14. As the dose gets higher, the collision cascades broaden, and the interaction between adjacent FIB sites increases. When enough interaction occurs, the wet chemical etch can permeate through and etch away the entire patterned region, suppressing or destroying local surface height modulation.

A second issue that arises when patterning with FIB at 50 nm is that pits broaden with increasing dose. At large enough spacing, a pit formed into the surface will have some diameter and will be surrounded by substrate, what we refer to as pit in terrace. We were able to measure the cross section and diameter of a pit by preparing a sample with 100 nm spacing, to assure that the pit wouldn't be affected by the proximity of other pits. Even at the lowest doses, the breadth of the pits is at 50 nm, so that patterning at 50 nm, even at the lowest doses, the resulting pattern will be affected by interaction.

To visualize this interaction we obtained a small section of AFM linescan from each of the doses in the study as seen in Fig. 5-17. At low dose and 100 nm spacing the pits are discrete; at higher dose they broaden and the terrace in between disappears. To get a sense of what would happen during patterning at 50 nm a section of the dots was superimposed on the drawing. Material that appears above the intersection of the scans was removed, because it would ostensibly be removed if patterning was actually at 50 nm in the wet etch process. The anticipated surface morphology is presented which is characteristically close to what we have observed in experiment (Fig.4-10). The patterns are essentially continuously modulated surfaces with periodicity of 50 nm. Where the patterns were terrace free at 100 nm, an offset is formed with respect to the surrounding substrate. This is shown with the black dotted line for the 10K ion sample. The 20 K pattern wasn't used because there was surface interaction and pattern offset at 100nm.

Offsets occur where the pit volumes intersect below the substrate surface. This is visible for doses as low as 3K. There is an offset at 5K and an even more pronounced offset at 20K. In 20K the crown portion appears as discrete mounds on a planar surface. This offset typically has no bearing on QD formation.

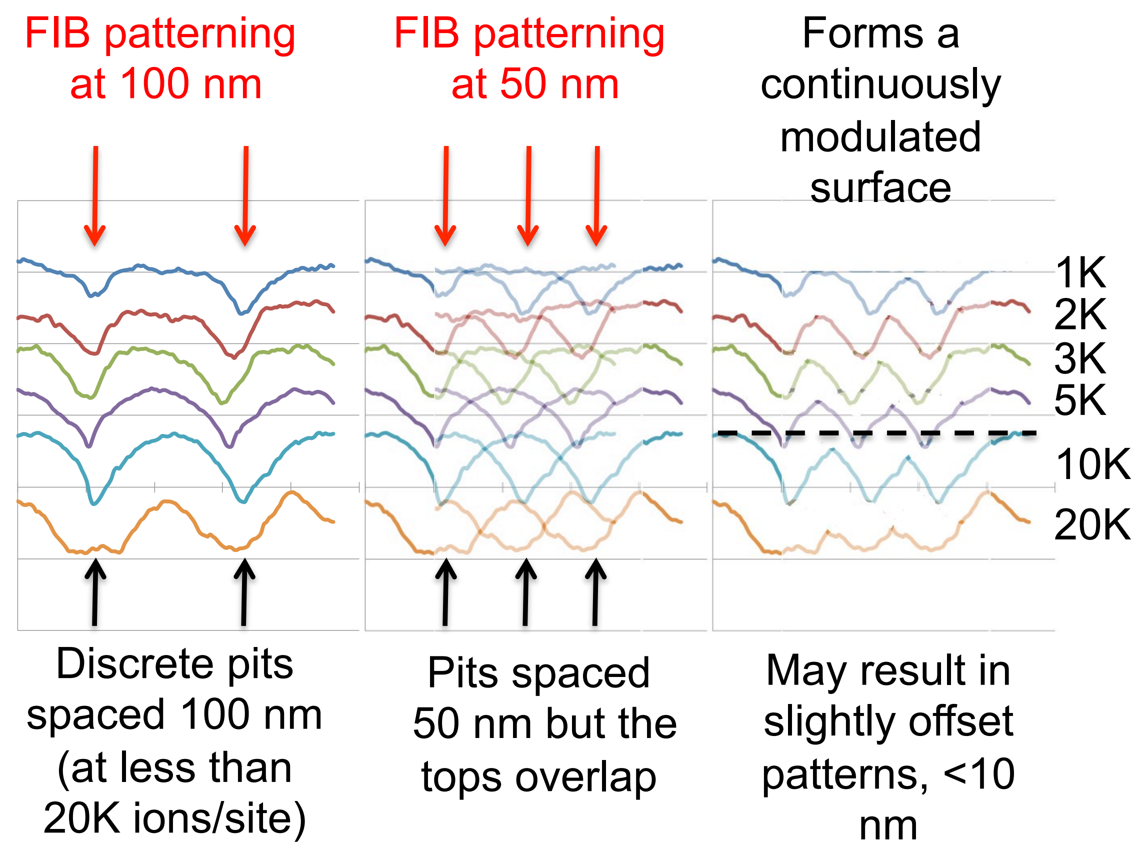

**Figure 5-17: Left: Linescans of pits at 100 nm at varying dose. Center: Linescans with a pit superimposed at 50 nm. Right: Linescans after removal of the combined pits.**

## 5.5 Gallium

Pascale et al. [83] went to great care to eliminate the gallium from their sample, while Portavoce et al. [25] were able to grow directly onto a FIB patterned surface following a short anneal. Portavoce et al. also deliberately coated a sample with a 1 ML film of Ga to determine whether the implanted Ga was responsible for changing the surface reactivity. The Ga film had no influence on the growth; the QDs formed in the pits as before. We were interested in knowing what Ga remained in the sample at the point of deposition, i.e. after cleaning and desorption.

A sample was prepared with three large 35 x 35 μm patterned areas. A high dose sample, 4000 ions/site was patterned at 100 nm to avoid over-etching during cleaning, a second was patterned at 1000 ions/site at 100 nm, and a third pattern with 1000 ions/site at 50 nm, thus having the same dose as the ions/site as the previous sample, but having the same total ion exposure as the first sample. The sample was cleaned with our standard cleaning process, placed in the chamber and outgassed, and then desorbed. Following the desorb process the wafer was quenched and a low temperature, 125 nm Si cap was deposited on top. The deposition was paused after 50 nm and a fractional layer of Ge was deposited. A second Ge marking layer was deposited at 100 nm and finally 25 nm of Si completed the cap.

The sample was sent to Surface Science Western where time of flight secondary ion mass spectrometry (ToF-SIMS) to depth profile the Ge and Ga. A 25 keV $Bi_3^+$ primary ion beam pulsed at 10 kHz was used to bombard the sample and generate secondary ions. A 249 μm x 249 μm region was sputtered using a 10keV $C_{60}^+$ ion beam at a rate of 0.072 nm/s. The results are shown in Fig. 5-18. The remaining Ga is shown in panel 2 of Fig. 5-18 (c). The bright white dot at the center is where the pattern fiducial was placed. From the table you can see that while it is brighter than the other patterned areas, the actual number of Ga ions is roughly the same, they were just patterned into a much smaller volume in order to assure over-etching during the wet cleaning to make the pattern visible by optical microscopy. The 4000-100:1000-100 ion count ratio remained constant, 197:53, however there was a measurable loss (25%) in the 50 nm pitch pattern, 197:147. The first Ge peak was detected at 25 nm below the surface and the second was detected at 70 nm. The Ga was reported to start at 114 nm. And be centered at 134 nm. Given that the second Ge surface was measured at 70 nm, we expect that the substrate surface is at 115 nm. From that depth the Ga concentration is constant for approx. 30 nm. The uniformity of the profile is somewhat surprising given implantation profiles are not constant, but the depth is expected given that our source is 30 keV. There is clear evidence that there is Ga within the samples at the time of growth, but as the profile in the substrate is uniform, we do not anticipate it affecting the growth, given Portavoce et al. ‘s results.

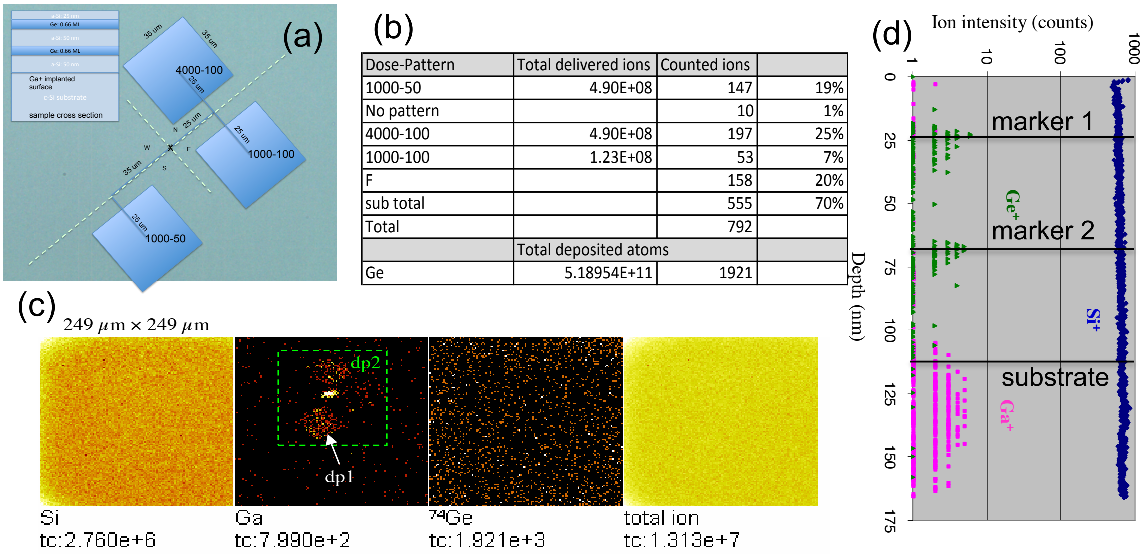

| Dose-Pattern | Total delivered ions | Counted ions | |
|---|---|---|---|
| 1000-50 | 4.90E+08 | 147 | 19% |
| No pattern | | 10 | 1% |
| 4000-100 | 4.90E+08 | 197 | 25% |
| 1000-100 | 1.23E+08 | 53 | 7% |
| F | | 158 | 20% |
| sub total | | 555 | 70% |
| Total | | 792 | |
| | Total deposited atoms | | |
| Ge | 5.18954E+11 | 1921 | |

**Figure 5-18: (a) Pattern configuration for ToF-SIMS analysis. (b) table of delivered dose by pattern site and measured residual Ga. (c) x-y plots of measured ion count for Si, Ga, Ge, and total counts. (d) depth profile showing ion counts**

# 6 Conclusions

Our goal in this work was to develop the capability and understanding to grow quantum dot mesocrystals in a two step process. The first step is the formation of ordered two-dimensional epitaxial Ge QDs arrays grown by molecular beam epitaxy (MBE) on Si (001) by directing the nucleation through morphological patterning using a focused ion beam (FIB). The second step is to extend the ordered arrays into the third dimension with additional MBE growth of Ge/Si multilayers on the initial seed layer. A key challenge was to push the patterning lengthscales down to 50 nm, well below what FIB-based directed self-assembly in the Ge/Si system has been able to achieve before. We were able to demonstrate that in principle, this is possible. But we have also uncovered numerous pitfalls and issues with FIB-based patterning. Many of these issues were hidden when just characterizing the upper surface by atomic force microscopy, and were only revealed when cross-section transmission electron microscopy was employed. Some of these pitfalls we now understand, others still require more work to unravel, and to determine whether they can be overcome.

Using FIB in conjunction with wet chemical cleaning enabled us to create surface morphology suitable for directed nucleation of QDs, but at ion doses 2 to 5 times lower than previously reported. In fact, we have found that patterning at previously reported doses leads to loss of fidelity in our process, because at 50 nm pitch, and 30keV Ga ion energy, interactions between proximal FIB-milled sites occurs, and at sufficiently high doses is catastrophic. Patterning at lower doses reduces the number and extent of implantation recoil defects. Even at low doses, however, we found using XTEM that the implanted regions do not always fully recover in our patterns due to the low-temperature Si processing route we developed in order to avoid excessive smoothing of the pattern by surface diffusion. These retained defects can pin or repel deposited material, where the

Si adatoms appear much more sensitive to local defectivity than the Ge adatoms. Inspection of the implanted pit regions in TEM for patterns exhibiting anomalous growth is not always conclusive, showing a range of defect densities, including regions or patterns with no apparent extended defects (but point defects may still be supersaturated). We emphasize, however, that even in the presence of defects, the Ge/Si layers and multilayers retain their epitaxial growth.

Clearly the FIB pattern site is a critical feature, dictating the nature of the growth for a number of layers. Future success depends on a process that eliminates this cause of pattern interruption. One potential solution is patterning at lower energies, which has the advantage of localizing the damage to the near surface region and reducing the depth of the implanted Ga. We have learned through experience that when patterning in conjunction with the wet etch, <u>it is not necessary to have a high sputter yield, just a high concentration of localized defects</u>. As FIB implantation and defect generation are the likeliest sources of non-repeatability in the pattern generation process, a clear understanding of the effects of defocus and beam shape on the defect distribution is vital.

We developed a process that routinely forms uniform arrays of ordered quantum dots on FIB patterned surfaces at 50 nm. Using AFM determined the periodicity, positional accuracy, volume, height, and surface features such as orientation or facet angle. The dots form dome like structures on the crowns, i.e. the four-field region in between four pits, which we determined by etching away the Ge from a known region of a pattern of QDs, and comparing the with-Ge and without-Ge scans. The formation of QDs on crowns is an unexpected result, given the preponderance of literature shows that Ge QDs nucleate in pits, especially when the pits are discrete entities, with intervening terraces that are relatively flat (001) surface. However, patterning at 50 nm can lead to a continuously modulated Si surface instead of pit-in-terrace. The continuously modulated surface at such a short lengthscale exacerbates surface energy anisotropy effects that reduces nucleation barriers to formation of Ge islands on top of crowns, and/or makes formation on the crowns degenerate with formation in the pit. Certainly, if there is defectivity retained in the pit, this can break the degeneracy and drive nucleation of the QD to the crown. We clearly verified the formation of the QDs on crowns, which we saw frequently using AFM, and using TEM on two patterns samples. Interestingly, in both cases, we did not observe extended defects in the pits. While we cannot rule out supersaturations of point defects or some retained Ga, these results leave open the possibility that growth on crowns is an intrinsic feature, rather than being a defect-driven response only.

Finally we have grown a number of QDMCs with varying numbers of layers. Some generalities in the results have emerged. Two- and three-layer QDMCs mimic the original seed-layer pattern morphology. But when the pattern is extended to 5 or 6 layers, there is coalescence of the Ge QDs (i.e., they are no longer discrete) and loss of extreme morphology, although the residual 50 nm pattern is still evident. Our original hypothesis was that as the QDMC gets thicker, there was gradual loss of the necessary inhomogeneous strain fields to direct nucleation of the next layer of QDs. However, after a thorough analysis by cross-section TEM, we identified a more complex process. The FIB sites are clearly pinning the Si layers, especially the Si buffer, but also the Si interlayers. Some pinning of Ge may have occurred also, but Ge was clearly migrating by surface diffusion into regions that Si was being repelled from. The Si pinning, in particular, led to development of extreme morphology within the sample. This occurs in part due to a growth bias within our MBE, where features like voids can be created by shadowing effects from tall surface features. A necessary condition of this morphology is the pinning or repulsion of Si. Without pinning there is no extreme morphology. The remarkable thing about this initially extreme evolution is that it retains the pattern periodicity, and the surface features can even appear quasi-regular. Within a 5-bilayer

QDMC sample, once the shadowing effect was “resolved” by diffusion and inflow processes as the pinning features were buried, the free diffusion of Si during interlayer growth then began to partially replanarize. Ge grown on this Si layer was then found to preferentially occur over the buried voids, typically in the lower-height features of the layer, suggesting that in the absence of the FIB site influence, that QDs will form in the pit. This argument is further supported by the formation of a well-ordered QDMC where Si pinning and the resultant voids weren’t present.

The prospects for patterning with FIB rest with a solution to the control of defectivity in the FIB implanted sites. This may be realized through limiting defectivity in the near surface region by use of reduced FIB energies, and removing the defectivity with a subsequent defect selective etch, or repairing the surface with a buffer that restores the wettability of Si adatoms. The challenge is preserving a surface morphology suitable to direct QD formation through limiting Si surface diffusion while at the same time, increasing Si surface diffusion to repair or encapsulate the defects. Additionally, while formation on non-planar surfaces lowers critical nucleation volumes, the limits are not precisely known. Models exist to predict nucleation sites on idealized periodic surfaces, however, models for irregular surfaces at small lengthscales do not yet exist. There are prospects for this technological approach not yet realized.

# 7 References

[1] Y. W. Mo, D. E. Savage, B. S. Swartzentruber, and M. G. Lagally, Phys. Rev. Lett. **65**, 1020 (1990).

[2] D. J. Eaglesham and M. Cerullo, Phys. Rev. Lett. **64**, (1990).

[3] J. Tersoff, C. Teichert, and M. Lagally, Phys. Rev. Lett. **76**, 1675 (1996).

[4] F. Meier, J. Levy, and D. Loss, Phys. Rev. B **68**, 134417 (2003).

[5] C. E. Pryor, M. E. Flatté, and J. Levy, Appl. Phys. Lett. **95**, 232103 (2009).

[6] R. Hull, J. Floro, J. Graham, J. Gray, M. Gherasimova, A. Portavoce, and F. M. Ross, Mater. Sci. Semicond. Process. **11**, 160 (2008).

[7] C. Dais, G. Mussler, T. Fromherz, E. Müller, H. H. Solak, and D. Grützmacher, Nanotechnology **26**, 255302 (2015).

[8] S. Karmakar and F. C. Jain, Mater. Sci. Appl. **2012**, 807 (2012).

[9] G. Fiedler and P. Kratzer, New J. Phys. **23**, 2836 (2013).

[10] G. Fiedler, L. Nausner, Y. Hu, P. Chen, A. Rastelli, and P. Kratzer, Phys. Status Solidi A **213**, 532 (2015).

[11] K. L. Wang, D. Cha, J. Liu, and C. Chen, Proc. IEEE **95**, 1866 (2007).

[12] C. Teichert, Phys. Rep. **365**, 335 (2002).

[13] O. P. Pchelyakov, A. V. Dvurechensky, A. V. Latyshev, and A. L. Aseev, Semicond. Sci. Technol. **26**, 014027 (2010).

[14] L. Vescan, T. Stoica, O. Chretien, M. Goryll, E. Mateeva, and A. Mück, J. Appl. Phys. **87**, 7275 (2000).

[15] S. Narusawa, T. Chiba, T. Tsuboi, N. Usami, T. Maruizumi, and Y. Shiraki, IEEE J. Sel. Top. Quantum Electron. **18**, 1830 (2012).

[16] X. Xu, T. Maruizumi, and Y. Shiraki, ECS Trans. **61**, 63 (2014).

[17] H. Hu, H. J. Gao, and F. Liu, Phys. Rev. Lett. **216102**, 2 (2008).

[18] Z. Zhong and G. Bauer, Appl. Phys. Lett. **84**, 1922 (2004).

[19] C. Dais, H. H. Solak, Y. Ekinci, E. Müller, H. Sigg, and D. Grützmacher, Surf. Sci. **601**, 2787 (2007).

[20] M. Grydlik, G. Langer, T. Fromherz, F. Schäffler, and M. Brehm, Nanotechnology **24**, 105601 (2013).

[21] A. Alkhatib and A. Nayfeh, Sci. Rep. **3**, 2099 (2013).

[22] M. Kammler, R. Hull, M. C. Reuter, and F. M. Ross, Appl. Phys. Lett. **82**, 1093 (2003).

[23] R. Hull, J. L. Gray, M. Kammler, T. Vandervelde, T. Kobayashi, P. Kumar, T. Pernell, J. C. Bean, J. A. Floro, and F. M. Ross, Mater. Sci. Eng. B **101**, 1 (2003).

[24] F. M. Ross, M. Kammler, M. C. Reuter, and R. Hull, Philos. Mag. **84**, 2687 (2004).

[25] A. Portavoce, M. Kammler, R. Hull, M. C. Reuter, and F. M. Ross, Nanotechnology **17**, 4451 (2006).

[26] T. I. Kamins and R. S. Williams, Appl. Phys. Lett. **71**, 1201 (1997).

[27] G. Jin, J. L. Liu, S. G. Thomas, Y. H. Luo, K. L. Wang, and B.-Y. Nguyen, Appl. Phys. A Mater. Sci. Process. **70**, 551 (2000).

[28] Z. Zhong, a. Halilovic, M. Mühlberger, F. Schäffler, and G. Bauer, Appl. Phys. Lett. **82**, 445 (2003).

[29] T. Kitajima, B. Liu, and S. R. Leone, Appl. Phys. Lett. **80**, 497 (2002).

[30] L. Vescan, M. Goryll, T. Stoica, P. Gartner, K. Grimm, O. Chretien, E. Mateeva, C. Dieker, and B. Holländer, **432**, 423 (2000).

[31] T.-S. Yoon, H.-M. Kim, K.-B. Kim, D. Y. Ryu, T. P. Russell, Z. Zhao, J. Liu, and Y.-H. Xie, Phys. Status Solidi **246**, 721 (2009).

[32] M. Lapedus, Semicond. Eng. (2014).

[33] J. A. Floro, E. Chason, S. R. Lee, and G. A. Petersen, Appl. Phys. Lett. **71**, 1694 (1997).

[34] J. P. Dismukes, L. Ekstrom, and R. J. Paff, **437**, (1964).

[35] E. Kasper, A. Schuh, G. Bauer, B. Holländer, and H. Kibbel, J. Cryst. Growth **157**, 68 (1995).

[36] J. Tersoff, Phys. Rev. B **43**, 9377 (1991).

[37] G. Medeiros-Ribeiro and A. Bratkovski, Science **279**, 353 (1998).

[38] A. Rastelli, M. Stoffel, J. Tersoff, G. Kar, and O. Schmidt, Phys. Rev. Lett. **95**, 026103 (2005).

[39] E. Sutter, P. Sutter, and J. E. Bernard, Appl. Phys. Lett. **84**, 2262 (2004).

[40] J. Floro, M. Sinclair, E. Chason, L. Freund, R. Twesten, R. Hwang, and G. Lucadamo, Phys. Rev. Lett. **84**, 701 (2000).

[41] A. Rastelli, M. Stoffel, G. Katsaros, J. Tersoff, U. Denker, T. Merdzhanova, G. S. Kar, G. Costantini, K. Kern, H. von Känel, and O. G. Schmidt, Microelectronics J. **37**, 1471 (2006).

[42] J. Tersoff and R. M. Tromp, Phys. Rev. Lett. **70**, 2782 (1993).

[43] J. Tersoff and F. LeGoues, Phys. Rev. Lett. **72**, 3570 (1994).

[44] K. Brunner, Reports Prog. Phys. **65**, 27 (2002).

[45] J. Floro, E. Chason, L. Freund, R. Twesten, R. Hwang, and G. Lucadamo, Phys. Rev. B **59**, 1990 (1999).

[46] F. M. Ross, R.M. Tromp, and M. C. Reuter, Science **286**, 1931 (1999).

[47] T. I. Kamins, G. Medeiros-Ribeiro, D. a. a. Ohlberg, and R. Stanley Williams, J. Appl. Phys. **85**, 1159 (1999).

[48] M. Brehm, F. Montalenti, M. Grydlik, G. Vastola, H. Lichtenberger, N. Hrauda,

M. J. Beck, T. Fromherz, F. Schäffler, L. Miglio, and G. Bauer, Phys. Rev. B **80**, 205321 (2009).

[49] R. Bergamaschini, M. Brehm, M. Grydlik, T. Fromherz, and G. Bauer, Nanotechnology **285704**, (2011).

[50] M. Kästner and B. Voigtländer, Phys. Rev. Lett. **82**, 2745 (1999).

[51] F. Ross, J. Tersoff, and R. Tromp, Microsc. Microanal. **4**, 254 (1998).

[52] R. Asaro and W. Tiller, Metall. Trans. **3**, 1789 (1972).

[53] M. Grinfeld, Dokl. Akad. Nauk SSSR **290**, 1358 (1986).

[54] D. Srolovitz, Acta Metall. **37**, 621 (1989).

[55] J. Tersoff, B. Spencer, a. Rastelli, and H. von Känel, Phys. Rev. Lett. **89**, 196104 (2002).

[56] G. Springholz, V. Holy, M. Pinczolits, and G. Bauer, Science (80-. ). **282**, 734 (1998).

[57] E. Mateeva and P. Sutter, **71**, 3233 (1997).

[58] Z. Zhong, H. Lichtenberger, G. Chen, M. Mühlberger, C. Schelling, J. Myslivecek, A. Halilovic, J. Stangl, G. Bauer, W. Jantsch, and F. Schäffler, Microelectron. Eng. **83**, 1730 (2006).

[59] R. Leon, T. Senden, Y. Kim, C. Jagadish, and a. Clark, Phys. Rev. Lett. **78**, 4942 (1997).

[60] I. Berbezier, A. Ronda, A. Portavoce, and N. Motta, Appl. Phys. Lett. **83**, 4833 (2003).

[61] J. H. Zhu, K. Brunner, G. Abstreiter, O. Kienzle, and F. Ernst, Thin Solid Films **336**, 252 (1998).

[62] L. Persichetti, A. Sgarlata, M. Fanfoni, and A. Balzarotti, Phys. Rev. Lett. **104**, 036104 (2010).

[63] F. M. Ross, IBM J. Res. Dev. **44**, 489 (2000).

[64] S. Y. Shiryaev, F. Jensen, J. L. Hansen, J. W. Petersen, and A. N. Larsen, Phys. Rev. Lett. **78**, 503 (1997).

[65] S. W. Kim, Phys. Rev. B 6 (2002).

[66] Y. Nitta, M. Shibata, K. Fujita, and M. Ichikawa, **462**, (2000).

[67] J. Brunner, P. Schittenhelm, J. Gondermann, B. Spangenberg, B. Hadam, T. Köster, H. G. Roskos, H. Kurz, H. Gossner, I. Eisele, and G. Abstreiter, J. Cryst. Growth **150**, 1060 (1995).

[68] Z. Zhong, H. Lichtenberger, G. Chen, M. Mu, C. Schelling, J. Myslivecek, A. Halilovic, J. Stangl, G. Bauer, W. Jantsch, and F. Scha, Microelectron. Eng. **83**, 1730 (2006).

[69] T. I. Kamins and R. S. Williams, Appl. Phys. Lett. **71**, 1201 (1997).

[70] B. Yang, F. Liu, and M. Lagally, Phys. Rev. Lett. **92**, 025502 (2004).

[71] G. Jin, J. L. Liu, and K. L. Wang, Appl. Phys. Lett. **76**, 3591 (2000).

[72] C. Dais, G. Mussler, H. Sigg, E. Müller, H. H. Solak, and D. Grützmacher, J. Appl. Phys. **105**, 0 (2009).

[73] Z. Zhong, A. Halilovic, M. Mühlberger, F. Schäffler, and G. Bauer, J. Appl. Phys. **93**, 6258 (2003).

[74] D. Grützmacher, T. Fromherz, C. Dais, J. Stangl, E. Müller, Y. Ekinci, H. H. Solak, H. Sigg, R. T. Lechner, E. Wintersberger, S. Birner, V. Holý, and G. Bauer, Nano Lett. **7**, 3150 (2007).

[75] C. J. Duska and J. Floro, J. Mater. Res. **29**, 2240 (2014).

[76] D. Grützmacher, C. Dais, L. Zhang, E. Müller, and H. H. Solak, Mater. Sci. Eng. C **27**, 947 (2007).

[77] G. Vastola, M. Grydlik, M. Brehm, T. Fromherz, G. Bauer, F. Boioli, L. Miglio,

and F. Montalenti, Phys. Rev. B **84**, 155415 (2011).

[78] A. Portavoce, M. Kammler, R. Hull, M. C. Reuter, and F. M. Ross, Nanotechnology **17**, 4451 (2006).

[79] M. Gherasimova, R. Hull, M. C. Reuter, and F. M. Ross, Appl. Phys. Lett. **93**, 023106 (2008).

[80] A. Karmous, A. Cuenat, A. Ronda, I. Berbezier, S. Atha, and R. Hull, Appl. Phys. Lett. **85**, 6401 (2004).

[81] A. Karmous, I. Berbezier, and A. Ronda, Phys. Rev. B **73**, 075323 (2006).

[82] I. Berbezier and a. Ronda, Surf. Sci. Rep. **64**, 47 (2009).

[83] A. Pascale, I. Berbezier, A. Ronda, and P. Kelires, Phys. Rev. B **77**, 075311 (2008).

[84] G. E. Becker and J. C. Bean, J. Appl. Phys. **48**, 3395 (1977).

[85] A. Ishizaka, J. Electrochem. Soc. **133**, 666 (1986).

[86] P. E. Thompson, J. Vac. Sci. Technol. B Microelectron. Nanom. Struct. **11**, 1077 (1993).

[87] W. Kern, J. Electrochem. Soc. **137**, 1887 (1990).

[88] J. F. Graham, C. D. Kell, J. A. Floro, and R. Hull, Nanotechnology **22**, 075301 (2011).

[89] D. J. Eaglesham and M. Cerullo, Appl. Phys. Lett. **58**, 2276 (1991).

[90] Y. Kudriavtsev, a. Villegas, a. Godines, and R. Asomoza, Appl. Surf. Sci. **239**, 273 (2005).

[91] M. W. Thompson, Philos. Mag. **18**, 377 (1968).

[92] G. Binnig and C. F. Quate, Phys. Rev. Lett. **56**, 930 (1986).

[93] https://upload.wikimedia.org/wikipedia/commons/5/5e/AFMsetup.jpg.

[94] http://www.ism.cnr.it/wp-content/uploads/2016/03/curva-forza.jpg.

[95] H. Lichtenberger, M. Muehlberger, and F. Schaffler, **3650**, 12 (2003).

[96] D. J. Eaglesham, G. S. Higashi, and M. Cerullo, Appl. Phys. Lett. **59**, 685 (1991).

[97] T. Kawase, A. Mura, K. Dei, K. Nishitani, K. Kawai, J. Uchikoshi, M. Morita, and K. Arima, Nanoscale Res. Lett. **8**, 151 (2013).

[98] http://nanolab.berkeley.edu/labmanual/chap1/1.10miscetch.pdf.

[99] R. Leancu, N. Moldovan, L. Csepregi, and W. Lang, Sensors Actuators A Phys. **46**, 35 (1995).

[100] O. G. Schmidt, U. Denker, S. Christiansen, and F. Ernst, Appl. Phys. Lett. **81**, 2614 (2002).

[101] J. N. Aqua and T. Frisch, Comptes Rendus Phys. **16**, 741 (2015).

[102] O. Shklyaev, M. Beck, M. Asta, M. Miksis, and P. Voorhees, Phys. Rev. Lett. **94**, 176102 (2005).

[103] J. N. Aqua and X. Xu, Phys. Rev. E - Stat. Nonlinear, Soft Matter Phys. **90**, 1 (2014).

[104] Y. J. Ma, Z. Zhong, X. J. Yang, Y. L. Fan, and Z. M. Jiang, Nanotechnology **24**, 015304 (2013).

[105] H. Wang and J. L. Gray, J. Vac. Sci. Technol. B Microelectron. Nanom. Struct. **29**, 04D106 (2011).

[106] J. Ziegler, M. Ziegler, and J. Biersack, Nucl. Inst. Methods Phys. Res. B **268**, 1818 (2010).

[107] C. A. Volkert and A. M. Minor, MRS Bull. **32**, 389 (2007).

[108] M. Posselt, F. Gao, and H. Bracht, Phys. Rev. B - Condens. Matter Mater. Phys. **78**, 1 (2008).

[109] M. K. Weldon, Y. J. Chabal, S. B. Christman, E. E. Chaban, L. C. Feldman, C. A. Goodwin, and C.-M. Hseih, in *Proc. Seventh Int. Symp. Silicon-on-Insulator*

*Technol. Devices*, edited by P. L. F. Hemment (1996), pp. 121–132.

[110] J. Dabrowski and H.-J. Mussig, *Silicon Surfaces and Formation of Interfaces: Basic Science in the Industrial World* (World Scientific Publishing Co. Pte. Ltd., 2000).

[111] M. Borselli, T. J. Johnson, and O. Painter, Appl. Phys. Lett. **88**, (2006).

# 8 Appendix A

## Floro Group Silicon Wafer Clean

Basic components: PTFE Beakers and Dippers, Teflon-coated tweezers, 18 MΩ DI water, Heated bath

Solutions: (solution stoichiometry is not critical)

IMEC: 4:1 Sulfuric:Peroxide ($H_2SO_4$:$H_2O_2$); self-heated Beaker should be 80% full

RCA 2: 4:1:1 Water:Hydrochloric:Peroxide ($H_2O$:HCl:$H_2O_2$); $80^{O}$C Beaker should be 75% full.

OXIDATION: 2:4:1 Water:Hydrochloric:Peroxide ($H_2O$:HCl:$H_2O_2$); $80^{O}$C Beaker should be 20-25% full.

Notes:

• Safety and Environment: Wear proper personal protection equipment (PPE). Keep the sash closed as much as possible. Know the location of eyewashes and showers. Only add acid to water, never the other way around. **HF IS INSIDIOUS – USE WITH EXTREME CAUTION.** Chemicals are NEVER poured down the drain – always store waste in properly labeled containers, expeditiously have waste picked up when full.

• Process Cleanliness: White hood is for wafer cleaning ONLY. Dippers and tweezers are CLEAN – *use only clean gloves to touch*, rest only on clean lint- free cloths. Beakers are dedicated to one specific solution and should never be used for anything else. Avoid passing over any open beaker. Do not let water run onto gloves and then into beakers. Rinse beakers thoroughly **before and after** clean (at least 5x). Maintain clean pads in the hood. Wipe down chemical bottles as needed to remove dust (before) or any acid drips (after). Thoroughly clean up when finished.

1. Pre-heat water bath to $80^{O}$C, at least one hour prior to starting clean.

2. When bath has stabilized, mix RCA 2 and OXIDATION solutions (but DON’T add peroxide yet) and place in bath to heat.

3. Pre-rinse wafer in its dipper in beaker DI-1.

4. Mix IMEC. Place wafer/dipper into Imec immediately. Etch for 5 min. (Rinse DI-1 and BOE-1)

5. Place wafer/dipper into full DI-1 and rinse for 3 min. (Dip tweezers in IMEC for 10 sec, and rinse briefly in DI-1)

6. Fill BOE-1. Dip wafer into BOE for 20 sec. The wafer should pull out dry.

7. Rinse in DI-1 for 2 min.

8. Add peroxide to RCA-2. When bubbling starts, place wafer/dipper in. Etch for 2 min. (Rinse DI-2, BOE-1, BOE-2) Fill BOE-2.

9. Dip rinse in DI-2, then etch in BOE-2 for 20 sec. Dip rinse in DI-2 again.

10. Put wafer/dipper back into RCA-2 for 2 more min. (Rinse DI-2)

11. Dip rinse in DI-2, then etch in BOE-2 for 20 sec. Dip rinse in DI-2 again.

12. Put wafer/dipper back into RCA-2 for 2 more min. (Rinse DI-2 and BOE-3) Fill BOE-3.

13. Dip rinse in DI-2, then etch in BOE-3 for 20 sec.

14. Rinse in DI-2 for 5 min.

15. Remove wafer from dipper, place in OXIDATION.

16. Add peroxide to OXIDATION. Warning – this is a violent solution!

17. After 5-6 min, add another shot of peroxide. (Rinse BOE-2, BOE-3, DI-2)

18. When OXIDATION solution has quenched, use tweezers to remove wafer, dip rinse,

place back in dipper, rinse for 10 min in DI-2. Turn off water bath, remove RCA-2 and OX beakers.

19. Wafer can remain in running DI until ready to dry and load in laminar flow hood.

20. Dry wafer with blowing $N_2$, inspect, mount, load into UHV load-lock, and pump down.

21. After wafer has been loaded, allow solutions to cool for 30 min before pouring into waste.

20. Dry wafer with blowing $N_2$, inspect, mount, load, and pump down.

21. After wafer has been loaded, allow solutions to cool for 30 min before pouring into waste.